Diode Laser Spectroscopy for Measurements of Gas Parameters in Harsh Environments

Amiya Behera

Dissertation submitted to the faculty of the

Virginia Polytechnic Institute and State University

in partial fulfillment of the requirements for the degree of

Doctor of Philosophy

In

Electrical Engineering

Anbo Wang, Chair

Luke Lester

Yong Xu

Mantu Hudait

Gary Pickrell

February 14, 2017

Blacksburg, VA

Keywords: Diode Laser Spectroscopy, Wavelength Modulation, Frequency Chirp, Distributed Sensing

Diode Laser Spectroscopy for Measurements of Gas Parameters in Harsh Environments

Amiya Behera

ABSTRACT

The detection and measurement of gas properties has become essential to meet rigorous criteria of environmental unfriendly emissions and to increase the energy production efficiency. Although low cost devices such as pellistors, semiconductor gas sensors or electrochemical gas sensors can be used for these applications, they offer a very limited lifetime and suffer from cross-response and drift. On the contrary, gas sensors based on optical absorption offer fast response, zero drift, and high sensitivity with zero cross response to other gases. Hence, over the last forty years, diode laser spectroscopy (DLS) has become an established method for non-intrusive measurement of gas properties in scientific as well as industrial applications. Wavelength modulation spectroscopy (WMS) is derivative form of DLS that has been increasingly applied for making self-calibrated measurements in harsh environments due to its improved sensitivity and noise rejection capability compared to direct absorption detection. But, the complexity in signal processing and higher scope of error (when certain restrictions on operating conditions are not met), have inhibited the widespread use of the technique.

This dissertation presents a simple and novel strategy for practical implementation of WMS with commercial diode lasers. It eliminates the need for pre-characterization of laser intensity parameters or making any design changes to the conventional WMS system. Consequently, sensitivity and signal strength remain the same as that obtained from traditional WMS setup at low modulation amplitude. Like previously proposed calibration-free approaches, this new method also yields absolute gas absorption line shape or absorbance function. Residual Amplitude Modulation (RAM) contributions present in the first and second harmonic signals of WMS are recovered by exploiting their even or odd symmetric nature. These isolated RAM signals are then used to estimate

the absolute line shape function and thus removing the impact of optical intensity fluctuations on measurement. Uncertainties and noises associated with the estimated absolute line shape function, and the applicability of this new method for detecting several important gases in the near infrared region are also discussed. Absorbance measurements from 1% and 8% methane-air mixtures in 60 to 100 kPa pressure range are used to demonstrate simultaneous recovery of gas concentration and pressure. The system is also proved to be self-calibrated by measuring the gas absorbance for 1% methane-air mixture while optical transmission loss changes by 12 dB.

In addition to this, a novel method for diode laser absorption spectroscopy has been proposed to accomplish spatially distributed monitoring of gases. Emission frequency chirp exhibited by semiconductor diode lasers operating in pulsed current mode, is exploited to capture full absorption response spectrum from a target gas. This new technique is referred to as *frequency chirped diode laser spectroscopy* (FC-DLS). By applying an injection current pulse of nanosecond duration to the diode laser, both spectroscopic properties of the gas and spatial location of sensing probe can be recovered following traditional Optical Time Domain Reflectometry (OTDR) approach. Based on FC-DLS principle, calibration-free measurement of gas absorbance is experimentally demonstrated for two separate sets of gas mixtures of approximately 5% to 20% methane-air and 0.5% to 20% acetylene-air. Finally, distributed gas monitoring is shown by measuring acetylene absorbance from two sensor probes connected in series along a single mode fiber. Optical pulse width being 10 nanosecond or smaller in the sensing optical fiber, a spatial resolution better than 1 meter has been realized by this technique.

These demonstrations prove that accurate, non-intrusive, single point, and spatially distributed measurements can be made in harsh environments using the diode laser spectroscopy technology. Consequently, it opens the door to practical implementation of optical gas sensors in a variety of new environments that were previously too difficult.

Diode Laser Spectroscopy for Measurements of Gas Parameters in Harsh Environments

Amiya Behera

GENERAL AUDIENCE ABSTRACT

The detection and measurement of gas properties has become essential to meet rigorous criteria of environmental unfriendly emissions and to increase the energy production efficiency. Although a lot of electrical gas sensors has been explored to meet these demands, they offer a very limited lifetime and suffer from cross-response and drift. On the contrary, gas sensors based on molecular spectroscopy offer fast response, zero drift, and high sensitivity with zero cross response to other gases. With the recent boom in telecomm sector, low cost diode lasers are now readily available for numerous applications. This makes them an excellent optical source for spectroscopy based gas monitoring. Hence, measurement of gas parameters using diode lasers (also known as *diode laser spectroscopy*) has become very popular over the last few decades. However, the harsh and rapidly changing conditions encountered in most industrial environments have inhibited its widespread use.

This dissertation presents novel strategies for practical implementations of diode laser spectroscopy systems. The proposed gas sensing system can simultaneously recover the concentration of a target gas and the ambient pressure at ultrahigh speed. It does not require any future calibration at installation site, which makes it quite ideal for applications like underground mine safety, monitoring combustion cycles in power plants, or monitoring leakage in natural gas pipelines. Furthermore, optical pulse generated by these diode lasers can be used to collect additional information regarding the location of gas leakage. This is demonstrated for measuring methane and acetylene gas in 60 to 100 kilopascal pressure range. Also, gas leakage location monitoring is proved by acetylene measurement from two sensor probes connected in succession along an optical fiber.

These demonstrations prove that accurate and non-intrusive measurements can be made using the diode laser spectroscopy technology even in harsh conditions. Consequently, it opens the door to practical implementation of optical gas sensors in a variety of new environments that were previously too difficult.

Acknowledgements

I sincerely thank my advisor, Professor Anbo Wang, who offered me the opportunity to study in such an excellent research group and university. Without his support, this arduous journey of Ph.D. would have never been a possibility for me. It is hard to quantify the intellectual and physical resources that Professor Wang made available to me, through him and through his group that made my graduate study such an enriching experience. I truly thank him for being a wonderful mentor and role model.

I would like to express my gratitude to the other committee members, Dr. Luke Lester, Dr. Yong Xu, Dr. Mantu Hudait, and Dr. Gary Pickrell for their support throughout this project. I am also grateful to Dr. Kray Luxbacher and Ms. Heather Dougherty for their help in installing my sensor system in underground coal mine.

My friends and colleagues at Center for Photonics Technology (CPT) made my time at Virginia Tech some of the most interesting days of my life. It's hard to envision more unique and widely-varying conversations than those shared over lunch and during brief visits to each other's desks. I would like to thank every student and staff member have worked with in CPT for their help in my research projects: Dr. Bo Dong, Dr. Dorothy Wang, Dr. Haifeng Xuan, Dr. Zhihao Yu, Dr. Chenyuan Hu, Dr. Lingmei Ma, Dr. Bo Liu, Dr. Michael Fraser, Dr. Aram Lee, Dr. Dong Wang, Zhipeng Tian, Chennan Hu, Yunbin Song, Scott Zhang, Mohammad Al-mamun, Li Yu, and Di Hu.

I would like to extend my acknowledgements to all my friends in Blacksburg, many of whom are also my colleagues at CPT. I am especially thankful to Yun and Di for the biking adventures in nearby mountain trails. I also want to thank Prasad Vaidya, Prashant Kumar, Sriram Malladi, Vireshwar Kumar, and Ravi Anant for making my stay in Blacksburg wonderful.

Finally, I would also like to express my deepest gratitude to my parents and family in India for their endless love, support, and encouragement.

Table of Contents

List of Figures

List of Tables

Acronyms and Abbreviations

A/D	Analog-to-Digital
AM	Amplitude Modulation
DFB	Distributed Feed Back
DLS	Diode Laser Spectroscopy
FBG	Fiber Bragg Grating
FC-DLS	Frequency Chirped Diode Laser Spectroscopy
FM	Frequency Modulation
FM/AM	Frequency Modulation generate Amplitude Modulation
FSR	Free Spectral Range
FWHM	Full-width-half-maximum
LIA	Lock-in amplifier
L-M	Levenberg-Marquardt
LPG	Long Period Grating
OPD	Optical Path Difference
RAM	Residual Amplitude Modulation
RF	Radio Frequency
TDLS	Tunable Diode Laser Spectroscopy
TEC	Thermo-electric cooler
TIA	Trans-impedance amplifier
TTL	Transistor Transistor Logic
WDM	Wavelength Division Multiplexing
WMS	Wavelength Modulation Spectroscopy

Chapter 1 Introduction

1.1 Background and Motivation

With the rapid rise in population, energy demands have increased exponentially in the last few decades. Currently coal, natural gas, and petroleum are the primary sources for energy production. But the usage of these fossil fuels adversely affects the environment because of carbon dioxide (CO_2) and other greenhouse gas (such as methane (CH_4), nitrous oxide (NOx)) emissions. Hence CO_2 capture for geological storage and real time in situ measurement of synthesis gas (syngas) composition in coal gasification to improve the fuel-to-energy efficiencies are getting a lot of attention. Additionally, natural gas consumption in the United States is expected to increase by 50% within the next 20 years [1]. At the same time, the largest component of the natural gas infrastructure which constitutes approximately 400 thousand miles of delivery pipelines are rapidly aging. Pipeline failure due to geohazards or third party interference can often lead to business loss and large scale environmental damage. Therefore, a reliable and timely detection of failure such as hydrocarbon leakage and emission along the pipeline is quite critical.

Many electrical gas sensing systems have been explored in the past to satisfy the requirements of energy industry. However, these electrical sensors are basically on-site point sensors with power supplies, offer limited sensitivity or measurement range, and cannot survive the hazardous conditions of measurement location. On the other hand, spectroscopy based optical fiber gas sensors are highly accurate, offer zero cross-sensitivity with other gases, and do not require calibration or a power supply at the measurement location. Thus Tunable Diode Laser Spectroscopy (TDLS) has gradually become an established method for non-intrusive measurements of gas properties for industrial and environmental monitoring applications. First applications of this technology were seen in mid-infrared (IR) taking advantage of the strong rotational/vibrational absorption transition lines present in that range [2–6]. However, this method did not become a popular industry tool until high performance distributed feedback (DFB) laser and InGaAs photodiodes became available in near IR range.

Working in near IR region allowed researchers to capitalize the low cost and robust optical components from the telecomm market, including optical fiber networks for remote access to harsh environments [7,8].

Two most common laser spectroscopy methods for single point gas detection are: TDLS with direct detection and TDLS with wavelength modulation. In TDLS with direct detection, laser frequency is scanned across one absorption line transition by thermal or current control. Then, using the non-absorbing sections of the transmitted light intensity as baseline, the absolute absorption line shape function is recovered. From this absolute line shape function, both concentrations and pressure variations can be compensated during measurement [9–11]. However, this technique is useful only when the selected absorption line is sufficiently strong and the resulting absorption attenuation in the transmitted intensity has high signal-to-noise (SNR) ratio. For detecting gases with weak absorption lines or in high pressure conditions, wavelength modulation is a more suitable method.

In typical TDLS with wavelength modulation (also known as Wavelength Modulation Spectroscopy or WMS), the laser frequency is simultaneously modulated by a ramp wave of sub-Hz or Hz frequency to the temperature or current control and a sine wave of kHz frequency to the current control. This produces multiple harmonics in the transmitted intensity which can be detected by a lock-in amplifier (LIA). In other words, WMS scheme enables AC detection of absorption profile at selected frequencies, thereby eliminating laser and 1/f noise [12–18]. Due to its inherent noise rejection capability, WMS is finding many applications in industrial process control such as high pressure coal gasifiers [19,20], ground test scramjet engines [21], internal combustion engines [22]. But the higher sensitivity of WMS technique also comes with a penalty of increase in complexity of signal analysis and higher scope of error [16–18].

Besides frequency modulation (FM), the sine wave fed to laser current control also modulates the laser output power; thus generating a sinusoidal amplitude modulation (AM) signal at the receiver. This signal is widely referred to as residual amplitude modulation (RAM). On the other hand, laser FM also produces another set of AM terms

at multiples of modulation frequency (f_m) due to the nonlinear response of absorption line shape in optical frequency domain. These terms are referred to as FM-generated AM (FM/AM). Without the presence of RAM, measured n^{th} harmonic signal would be purely from FM/AM and proportional to n^{th} derivative of absorption line shape function at small frequency modulation amplitudes [23,24]. However, in practical systems, RAM contributions to measured harmonic is often significant and produces distortions in all harmonic frequencies. Furthermore, measurements at first harmonic frequency is affected by an additional background RAM which is independent of gas concentration [24]. Therefore, signal processing for a WMS system is often complex.

One primary requirement of gas measurement in harsh environment is that the installed system should be stand-alone and require zero maintenance or calibration. For a WMS system, this is very difficult to realize because of the aforementioned distortion issue. In recent past, several researchers have proposed techniques to enable calibration free measurements using WMS. By definition, a *calibration free* measurement system can perform absolute measurements of gas concentration and other parameters (e.g. pressure or temperature) without any on-site calibration or comparison with a known gas mixture or condition. Two distinct methods have been reported in the past to address calibration issue, namely: 1) absorption line shape recovery from residual amplitude modulation (RAM) and its background value in first harmonic signal [24–28], 2) measurement of second harmonic signal normalized by first harmonic [22,29–31]. However, both methods impose a few limitations on system operating conditions and can often lead to erroneous results if these conditions are not met. Although some researchers have tried to mitigate those limitations by pre-characterizing all the system parameters with an empty gas cell measurement and later iteratively matching the simulated harmonics (from HITRAN database [32]) with measured signals [33,34], future measurements may show errors due to drift from pre-characterization test conditions, temperature variations, and aging of laser diode. In this dissertation, an alternative strategy to implement a calibration-free system is reported and it does not require any modification to traditional WMS design. Moreover, unlike the existing methods, the new approach does not require laser diode parameters such as average intensity, intensity modulation amplitude or

modulation rate to be known in advance. Thus it is more suitable for practical environments where most of the environmental conditions are unknown, the incident laser intensity is rapidly varying due to vibration, optical cavity window-fouling, beam-steering, etc.

Another focus of this dissertation is to explore the possibility of spatially distributed detection of gas properties using diode laser spectroscopy (DLS). The basic principle behind distributed fiber optic sensing can be illustrated by an Optical Time Domain Reflectometry (OTDR) system. Figure 1.1 shows the schematics of an OTDR system that consists of a pulsed laser, a detector, a coupler, and signal processing unit. In this system, an optical pulse launched into the fiber and the light is reflected back from a sensing location with information about measurand. Assuming the time at which reflected light is received is τ , the distance to sensing location can be estimated by time of flight (TOF) calculation. Thus sensor location s is given by:

$$s = \frac{v\tau}{2} \tag{1.1}$$

where v is the velocity of light in optical fiber. In this case, spatial resolution of the system is determined by the temporal bandwidth of the light pulse.

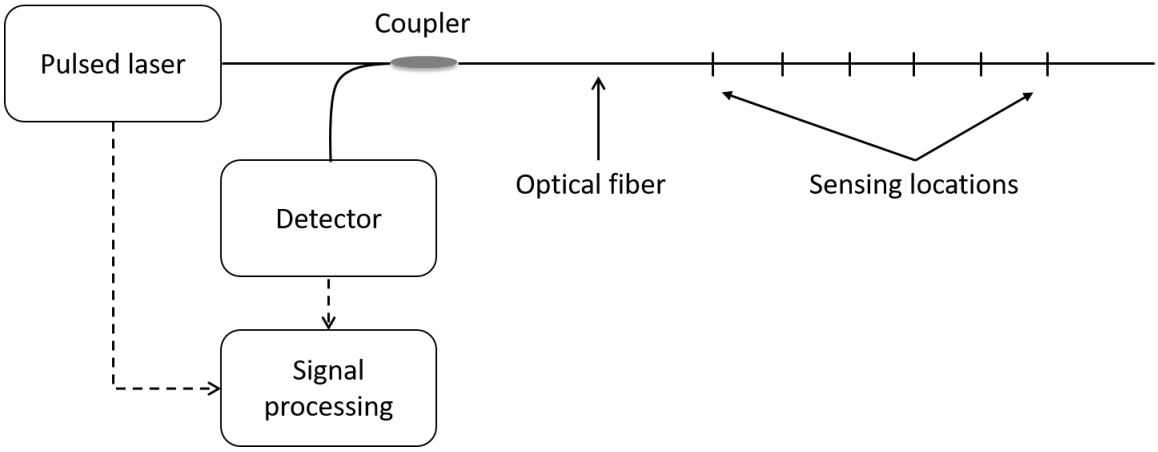

Figure 1.1. Distributed fiber optic sensing by OTDR method.

These kinds of distributed fiber optic sensing systems can be divided into two types by the spatial continuity of the measurand: (a) fully-distributed sensor, (b) quasi-distributed

sensor. A quasi distributed optical sensing system is one in which sensing elements are connected in succession at prescribed locations along the fiber. On the other hand, a fully-distributed sensor utilizes the entire fiber as the sensing element. Current distributed optical sensing technology is only capable of detecting gas with widely tunable external cavity lasers and Fabry-Perot interferometers as sensing elements with restricted lengths [35–39]. Furthermore, aforementioned techniques can only work at a fixed temperature and pressure conditions as they only measure the peak optical attenuation value resulting from gas absorption, not the complete gas absorption response. Thus such systems cannot realize *calibration-free* measurement. Although some researchers have used fiber long period grating (LPG) to detect hydrogen in a distributed manner, the fiber cladding requires a specialized coating for such sensing to work [40,41]. So this approach is gas specific and is difficult to implement for a long distance applications.

Clearly, for practical applications like hydrocarbon leakage monitoring for natural gas pipelines over several kilometers, the existing methodology is inadequate. Therefore, it would be highly desirable to develop a new technology that can permit long-span distributed measurement of gas properties using a single optical fiber.

1.2 Scope of the Dissertation

The primary objective of this research is to develop novel gas detection techniques using diode laser spectroscopy for both single point and spatially distributed monitoring. The contents of this dissertation are organized into six chapters.

Chapter 2: This chapter reviews fundamentals of molecular spectroscopy and dependence of absorption response on environmental conditions. This is followed by existing optical techniques used for single point gas monitoring and spatially distributed gas monitoring.

Chapter 3: A strategy to extract multiple gas parameters (concentration, pressure, and temperature) from their absorption response is described and then validated by simulations.

Chapter 4: This chapter discusses the current calibration-free WMS system techniques and their underlying limitations, describes an alternate strategy to measure absolute line

shape function, and demonstrates the efficacy of this alternate approach for calibration-free measurements by recovering RAM contributions from first and second harmonic signals. The simultaneous estimation of concentration and pressure from gas absorption response is also demonstrated.

Chapter 5: A novel approach to realize calibration-free spatially distributed measurement of gas parameters by standard telecomm diode lasers is discussed. The method is experimentally validated by estimating gas concentration and pressure from measured absorbance. Spatially distributed gas monitoring is also demonstrated using multiple sensor probes connected along a single mode fiber.

Chapter 6: This chapter summarizes the entire dissertation and also suggests directions for future research.

Chapter 2 Optical Gas Monitoring

2.1 Fundamentals of Molecular Absorption Spectroscopy

All molecules have quantized rotational and vibrational energy states in gas phase. When electromagnetic radiation or a photon interacts with one gas molecules, it can change its internal energy. Because these energy states are discrete, only photons that have energy equal to the difference in energy levels can be absorbed. Therefore, for an energy transition to be triggered, photon wavelength should be:

$$\lambda = \frac{hc}{\Delta E} \tag{2.1}$$

where ΔE is the separation between two molecular energy states in consideration, h is Planck's constant (6.63×10^{-34} J-s), c is the speed of light in vacuum, and λ is the wavelength of photon or incident light. As every chemical compound has its own specific molecular structure, the combination of vibration and rotational energy transitions are unique to its molecules. Thus these wavelengths of absorption can be used like human finger prints for their identification. This scientific measurement technique of studying, identifying, and quantifying different materials by light is known as *Molecular Spectroscopy*.

In general, vibrational energy transitions require high energy photons and occur in the visible or ultra-violet region of the electromagnetic spectrum. On the other hand, rotational energy transitions occur mostly in the far infrared or microwave region. However, photons in the near infrared and infrared range can often trigger an energy transition which involves changes in both vibrational state and rotation states. This is referred to as rotational-vibrational or ro-vibrational spectroscopy. The wavelengths at which energy level transitions occur are called *spectral lines* or *absorption lines*. In Figure 2.1, the absorption lines for carbon monoxide (CO) and carbon dioxide (CO_2) are shown overlapped for a wavelength range of 1560 nm to 1580 nm. The distinction between their absorption lines is quite clear.

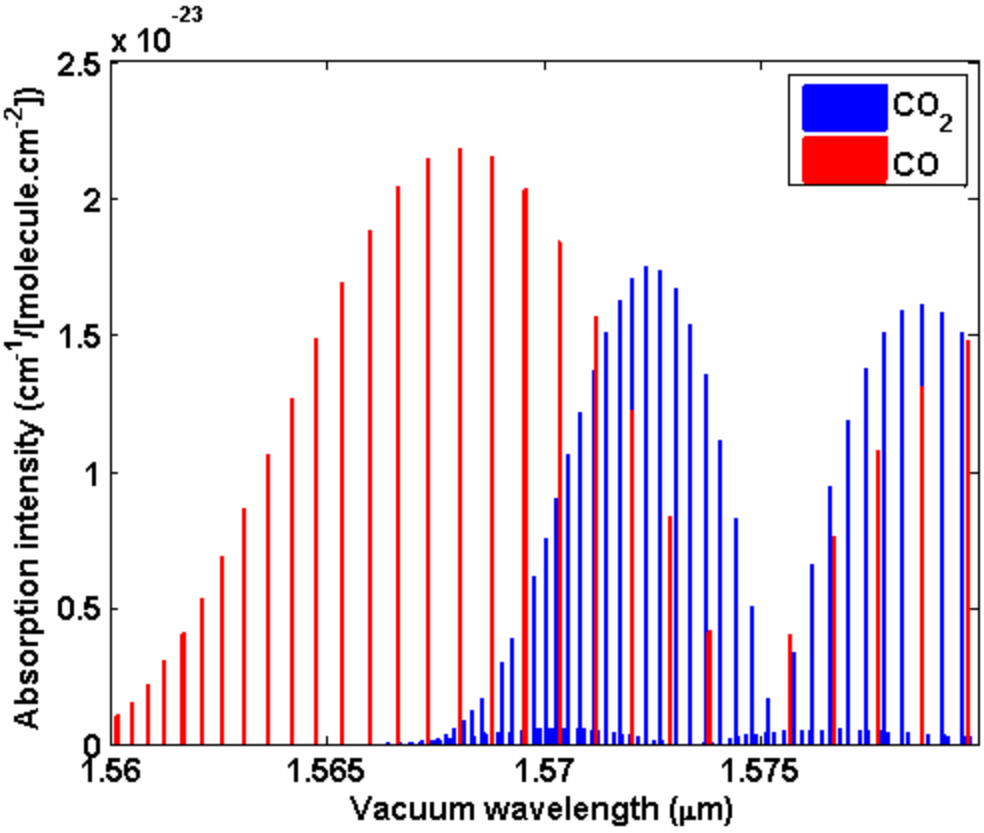

Figure 2.1. Absorption line intensity for carbon monoxide (CO) and carbon dioxide (CO_2) in the near infrared range (1560 nm ~ 1580 nm).

Although the spectra measured for each absorption line is expected to be infinitely narrow, measured results are always broad due to several physical processes. Theoretically, absorption response $\alpha(\nu)$ of a single line can be broken into two parts – line shape function ϕ_j and line strength or intensity S_j [42,43].

$$\alpha(\nu) = \sum_j S_j \bullet \phi_j(\nu - \nu_{0,j}) \tag{2.2}$$

where $\nu = \frac{1}{\lambda}$ is the wavenumber and $\nu_{0,j}$ is the absorption line center wavenumber of j^{th} transition for the gas molecule in consideration. The following sections take an in-depth look at the above two parameters and how they affect the intensity and width of gas absorption response.

2.1.1 Intensity of Line Spectra

The intensity of absorption line determines the amplitude or peak value of absorption response. There are two main contributors to line intensity and these are: transition probability and population of energy states. Transition probability is simply the likelihood of a molecule making transition from one energy level to another. This varies from molecule to molecule based on its three-dimensional shape or spatial orientation of chemical bonds between atoms. Additionally, absorption lines or spectra get considerably weaker with increasing energy levels. This is attributed to rapidly decreasing population density which is often modeled by the Boltzmann distribution. The ratio of population between upper energy state and lower energy state is given as:

$$\frac{N_{Upper}}{N_{Lower}} = e^{\left(\frac{-\Delta E}{kT}\right)} \tag{2.3}$$

where ΔE is the difference between energy states as before, k is the Boltzmann constant ($1.38 \times 10^{\wedge -23}$ JK^{-1}) and T is the temperature in Kelvin.

2.1.2 Width of Line Spectra

The width of absorption response is governed by the line shape function ϕ and its exact shape is determined from three primary broadening mechanisms: (a) Natural broadening, (b) Doppler broadening, and (c) Pressure (collisional) broadening.

2.1.2.1 Natural broadening

Natural broadening is a consequence of the finite lifetime of the excited state due to spontaneous emission. By quantum-mechanical theory, finite life time is equated with the precision of the energy (the longer a molecule remains in a particular energy level, the more precisely the energy will be defined) [43]. Heisenberg's uncertainty principle describes this mathematically as:

$$\Delta E' = h\Delta f \approx \frac{h}{2\pi\Delta t} \tag{2.4}$$

where $\Delta E'$ is the uncertainty of the energy level, h is Planck's constant as before and Δt is the natural lifetime of the molecule staying in the particular energy level. The spread of frequency Δf is known as the full-width-half-maximum (FWHM) linewidth from natural broadening and the spread in frequency is usually modeled by a Lorentz profile. However, natural line width is quite small compared to the other two and is often neglected in most practical applications.

2.1.2.2 Doppler broadening

Doppler broadening is the result of Doppler Effect, which is the apparent shift in the frequency of a signal emitted or absorbed by a body in motion. During spectroscopic measurement, the frequency of electromagnetic energy absorbed by a gas molecule changes according to the direction and velocity of its motion relative to the radiation source. If the molecule moves with a constant velocity towards the electromagnetic radiation, the frequency appears higher (blue shift) and hence the frequency at which absorption occurs is lower. On the other hand, if the molecule moves away from the electromagnetic radiation, the frequency appears lower (red shift) and hence absorption happens at a higher frequency. As molecular motion is random, both positive and negative frequency shift are possible. The result is a broad line shape function. Mathematically, this line shape is described by a Gaussian profile give as:

$$\phi_D(\nu-\nu_0)=\frac{2}{\Delta\nu_D}\bullet\sqrt{\frac{ln2}{\pi}}\exp\left[-4\ln 2\left(\frac{\nu-\nu_0}{\Delta\nu_D}\right)^2\right] \tag{2.5}$$

where $\Delta\nu_D$ is the FWHM for the Doppler broadened line shape and can be estimated by Eq. (2.6).

$$\Delta\nu_D(\mathrm{cm}^{-1})=7.1623\times10^{-7}\nu_0\sqrt{\frac{T}{M}} \tag{2.6}$$

Here T is gas temperature in Kelvin, M is its molecular mass in grams per mole [33]. Since velocity of gas molecules depends on their kinetic energy, a temperature

dependence was expected. However, there is no dependence on gas molecule other than its mass.

2.1.2.3 Pressure or collision broadening

Collision broadening or pressure broadening dominates at atmospheric pressure (~ 101 kPa) or higher. Due to the increased pressure, there is an increased likelihood of molecules colliding with each other. When another molecules comes closer to the target molecule, it perturbs the energy levels of the target molecule, and the absorbed photon frequency changes. Therefore, large number of collisions give rise to an increased blurring of the energy levels, and the result is a larger spread in frequencies. Since this is an extension of the natural broadening phenomena, the line shape function used to model the gas absorption is, again, Lorentzian distribution. This profile is given by:

$$\phi_C(\nu-\nu_0)=\frac{2}{\pi\Delta\nu_C}\frac{1}{1+\left[\frac{2(\nu-\nu_0)}{\Delta\nu_C}\right]^2} \tag{2.7}$$

where $\Delta\nu_C$ is the FWHM for collision broadened line shape and can be estimated from the gas parameters by Eq. (2.8).

$$\Delta\nu_C(\mathrm{cm}^{-1})=2\bullet P\bullet\sum_j \chi_j\bullet\gamma_j{}^{296K}\bullet\left(\frac{296}{T}\right)^{n_j} \tag{2.8}$$

Here P is gas pressure, χ_j is the mole fraction of collision partner j, γ_j is the collisional broadening coefficient (cm^{-1} atm^{-1}), and n_j is the temperature exponent of the collision width [33].

2.1.2.4 Voigt profile

Doppler broadening is the primary broadening mechanism up to 20 kPa gas pressure. But beyond 20 kPa, collision broadening begins to dominate. Thus a Lorentzian profile becomes increasingly more accurate with increasing pressure. In general, line shape function of a single absorption transition is described by a Voigt profile which is a

convolution of the two broadening curves [44–51]. Once, $\Delta\nu_C$ and $\Delta\nu_D$ have been estimated from gas pressure and temperature conditions, the Voigt shape can be computed using Eq. (2.9).

$$\phi_V(\nu) = \int_{-\infty}^{\infty} \phi_D(\nu')\phi_C(\nu - \nu')d\nu' \tag{2.9}$$

Figure 2.2 depicts normalized (unit area under the curve) Gaussian or Doppler profile, Lorentz profile, and Voigt profile responses for comparison. When Doppler and Collision broadening are both contributing, the wings of the absorption response show a Lorentz shape and the core or line center exhibits Doppler behavior.

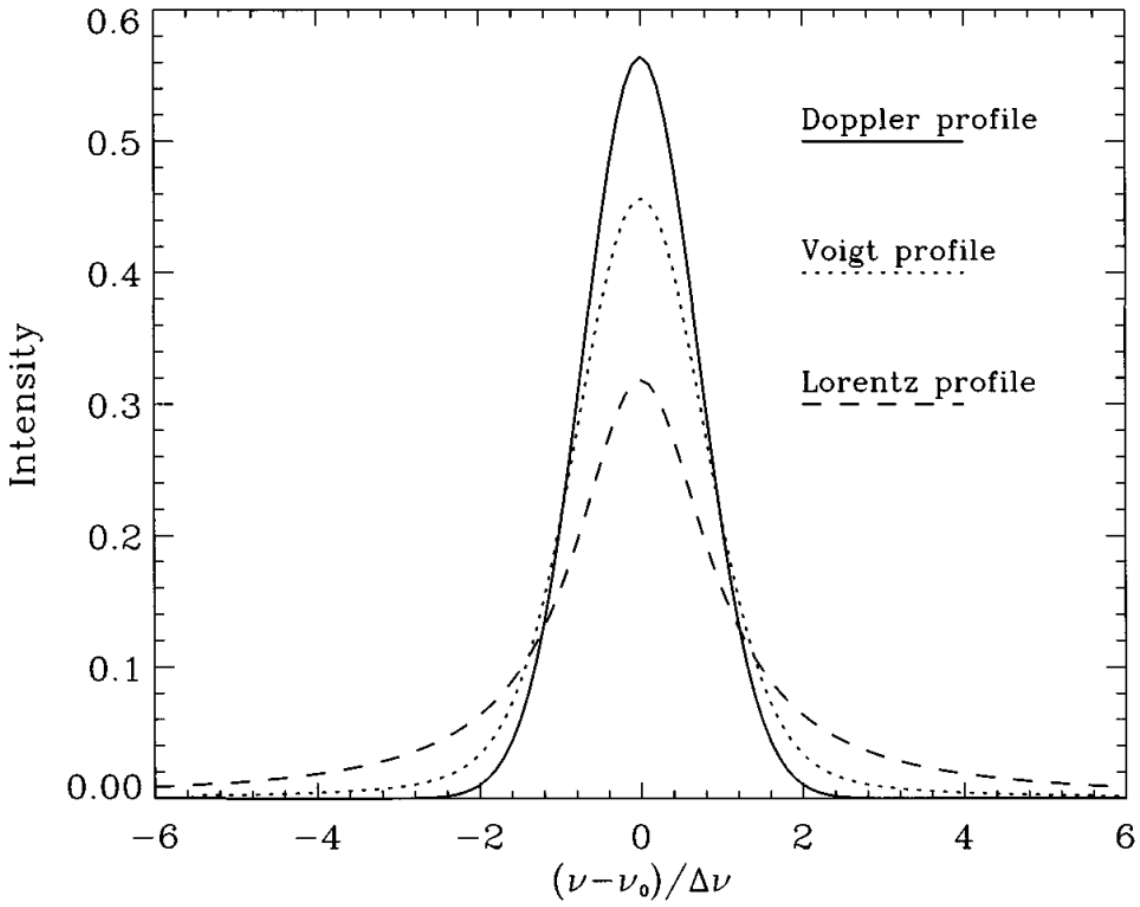

Figure 2.2. Comparison of normalized Lorentz, Doppler and Voigt line shapes functions [43] ($\Delta\nu$ is the FWHM for the corresponding line shape function and $\Delta\nu_D = \Delta\nu_C$ for the Voigt profile).

It should be noted that there is no closed form mathematical expression for the Voigt shape and it is often computed numerically. Otherwise, analytical approximation proposed by McLean et al can be used to evaluate Voigt profile pretty accurately [45]. Furthermore, for one atmospheric pressure and higher, $\phi_C >> \phi_D$ and Lorentz distribution alone is sufficient to describe the absorption response for most practical applications.

2.2 Single Point Gas Monitoring

2.2.1 Tunable Diode Laser Spectroscopy (TDLS) with Direct Detection

In Tunable Diode Laser Spectroscopy (TLDS), the laser frequency is temperature tuned by a ramp wave of sub-Hz frequency such that it scans the known single absorption line of target gas. This frequency or wavelength scanning can also be realized by current tuning in which case the scanning speed can be several hundred Hz. But this often requires a very precise control of laser temperature so that laser center frequency is always in close proximity of the absorption line. In either case, laser intensity I and wavenumber ν become functions of time. A simple setup for TDLS is depicted in Figure 2.3.

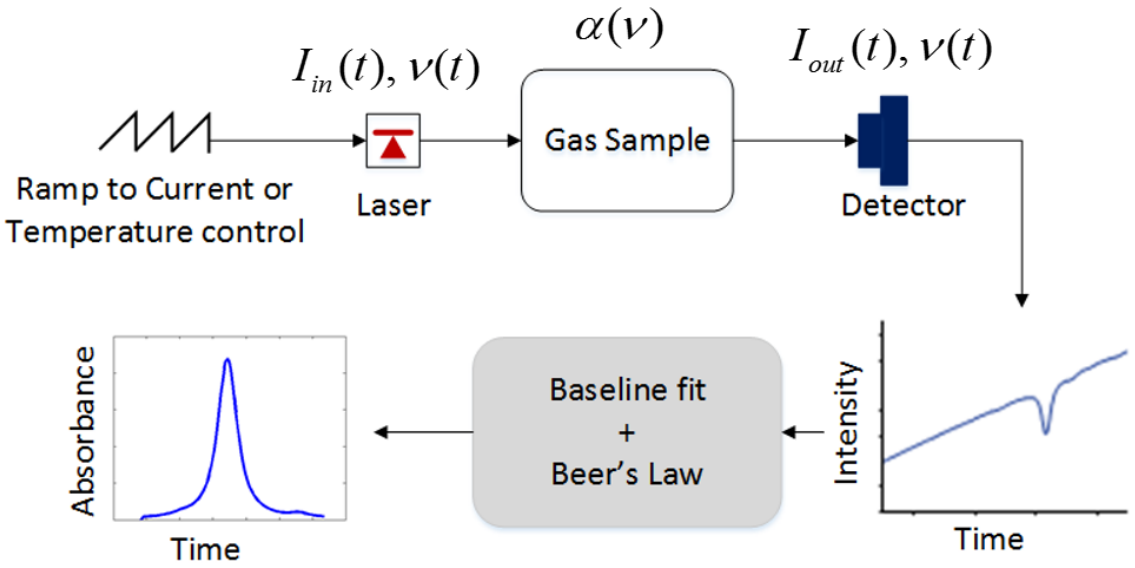

Figure 2.3. Typical setup for tunable diode laser spectroscopy.

The optical beam goes through an open gas cell where it interacts with the target gas. Since gas absorption response $\alpha(\nu)$ is frequency dependent, detected optical signal shows an amplitude change in time. The relationship between the input intensity I_{in} and output intensity I_{out} at a particular wavenumber ν is described by the Beer-Lambert law:

$$I_{out} = I_{in} e^{-\alpha(\nu)Cl} \approx I_{in}\left[1-\alpha(\nu)Cl\right] \tag{2.10}$$

where $\alpha(\nu)$ is the gas absorption response, C is the molar concentration of target gas, and l is the path length over which light and gas interact. $\alpha(\nu)Cl$ is referred to as *absorbance* and its maximum value is known as *optical depth* for the absorbing medium.

As the laser output is swept across the target gas absorption line, output intensity is monitored at the photodetector as a function of time. For a narrow scanning range (< 0.5 nm), $\nu(t)$ is quite linear when the scanning signal (temperature or current) for diode lasers is also linear function of time. Hence, absorption response measured in time domain $\alpha(\nu(t))$ is equivalent to true absorption response $\alpha(\nu)$. By using the non-absorbing sections of I_{out} (or the output intensity expected in the absence of gas absorption) to normalize total $I_{out}(t)$, absorbance $\alpha(\nu(t))Cl$ can be calculated. A detailed discussion on this normalization process is provided in Section 4.3.1. If l is known, gas concentration and other parameters can easily be estimated from absorbance.

2.2.2 Tunable Diode Laser Spectroscopy (TDLS) with Wavelength Modulation

TDLS with wavelength modulation or also known as Wavelength Modulation Spectroscopy (WMS) is a variation to direct detection with TDLS. Instead of using one ramp wave for laser frequency scan, additional sine wave of kHz frequency is fed to the laser current control. The block diagram for WMS measurements is shown in Figure 2.4.

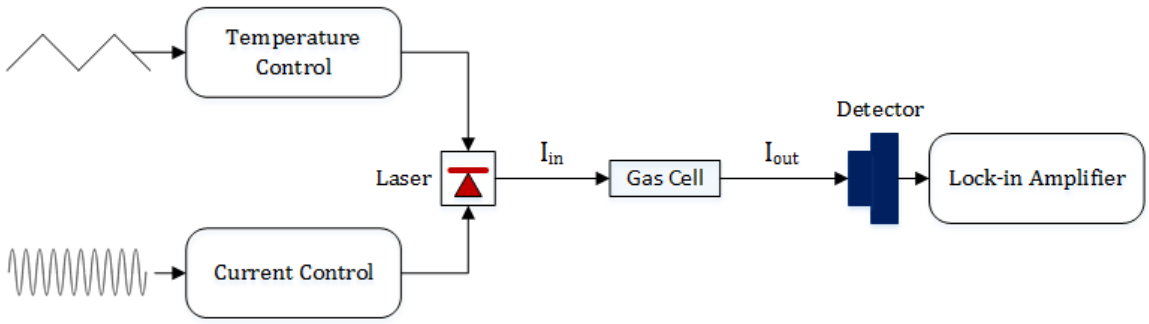

Figure 2.4. Typical setup for wavelength modulation spectroscopy (WMS).

The sine wave modulation produces both amplitude modulation (AM) and frequency modulation (FM) in the laser output. Taking into account these modulation effects, the input intensity at a particular wavenumber $\bar{\nu}$ can be written as follows: $I_{in} = I(\bar{\nu}) + \Delta I(\bar{\nu}) \bullet \cos(\omega t)$ and the output intensity, using Eq. (2.11), is as follows:

$$I_{out} = [I(\bar{\nu}) + \Delta I(\bar{\nu}) \bullet \cos(\omega t)] \bullet [1 - \alpha(\bar{\nu}) Cl] \tag{2.11}$$

$$\text{where } \nu = \bar{\nu} + \delta\nu \bullet \cos(\omega t - \psi) \tag{2.12}$$

Here, $\omega = 2\pi f_{\mathrm{m}}$ (f_{m} being the sine wave current modulation frequency), $\delta\nu$ and ΔI are the resulting FM and AM amplitudes, $\bar{\nu}$ is the laser center emission wavenumber, I is the average intensity, and ψ is the phase shift between AM and FM [24,29]. Since absorption response is nonlinear function of ν, multiple harmonics are present in the intensity I_{out} measured at the detector.

It should be noted that quality of WMS harmonic signals are highly dependent on the parameter called *modulation index*, m (where $m = \dfrac{2\delta\nu}{FWHM\ of\ \alpha(\nu)}$) and it can be adjusted by controlling the amplitude of sine wave fed to the laser current control. For $m \le 0.2$, the Taylor series expansion model proposed by Duffin et al. can be used to express the first harmonic (or 1f) and second harmonic (or 2f) terms present in I_{out} [24].

$$\begin{aligned} I_{1\mathrm{f}} &= \Delta I \bullet \cos(\omega t) - \Delta I \bullet \alpha(\bar{\nu}) \bullet Cl \bullet \cos(\omega t) \\ &\quad -\delta\nu \bullet I(\bar{\nu}) \bullet \alpha'(\bar{\nu}) \bullet Cl \bullet \cos(\omega t - \psi) \end{aligned} \tag{2.13}$$

$$I_{2f} = -\frac{\delta\nu}{2} \bullet \Delta I \bullet \alpha'(\bar{\nu}) \bullet Cl \bullet \cos(2\omega t - \psi) - \frac{\delta\nu^2}{4} \bullet I(\bar{\nu}) \bullet \alpha''(\bar{\nu}) \bullet Cl \bullet \cos(2\omega t - 2\psi) \quad (2.14)$$

As expected the sinusoidal amplitude modulation (AM) of the laser intensity generates an amplitude modulation in the measured harmonic. This signal is widely referred to as *residual amplitude modulation* (RAM). On the other hand, laser FM also produces another set of AM terms at multiples of modulation frequency (f_m) due to the nonlinear response of absorption line shape in optical frequency domain. These terms are referred to as *FM-generated AM* (FM/AM). Henceforth, terms proportional to ΔI and I in harmonic signal expressions would be referred to as RAM and FM/AM respectively. For instance, the first term in Eq. (2.13) is the background RAM which has no dependency on gas concentration; second term is an absorption dependent RAM variation; and the third term is traditional first derivative signal arising from FM/AM. Similarly, second harmonic signal expression in Eq. (2.14) has the first term from absorption dependent RAM and second term from traditional second derivative arising from FM/AM. Notice that there is no background RAM present in second harmonic signal which makes it ideal for zero reference measurements. However, both harmonics are not true derivatives of line shape function, $\alpha(\bar{\nu})$.

Compared to TDLS with direct detection scheme, WMS offers superior sensitivity due to better noise rejection by harmonic detection. The lock-in amplifier (LIA) is used to select and measure one these harmonics in output intensity. In most application, detection at the second harmonic is preferred as the derivative-like waveform has much of the baseline slope (background RAM interference) and noise associated with the first harmonic removed.

2.2.3 Multiple Gas Monitoring by Tunable Diode Laser Spectroscopy (TDLS) with Wavelength Modulation

In order to perform simultaneous sensing of multiple gases, harmonic detection by WMS scheme can be exploited. A simplified block diagram is shown in Figure 2.5 to explain

this principle. In this scheme, both carbon monoxide (CO) and carbon dioxide (CO_2) gas inside the gas chamber can be detected at the same time. DFB Laser 1 is centered at a wavelength of 1566 nm. It is temperature modulated by a ramp of frequency f and being current modulated by a sine wave of frequency f_1. Similarly, DFB Laser 2 is centered at a wavelength of 1572 nm. It is also temperature modulated by a ramp of f, but the current modulation is done by a sine wave at frequency f_2. f_2 is selected such that it is not a multiple of f_1 and the ramp frequency $f << f_1, f_2$. The optical signals from the two lasers are combined by a coupler and then sent to the gas chamber. The transmitted optical signal is collected by a single photo-receiver module and sent to the LIA for harmonic detection. This LIA is implemented in LabVIEW software from National Instruments.

It should be noted that this scheme does not require much hardware modification to the existing single gas sensing system and minimizes the cost by reducing the use of multiple fiber cable and optical receiver modules when several gases need to be monitored.

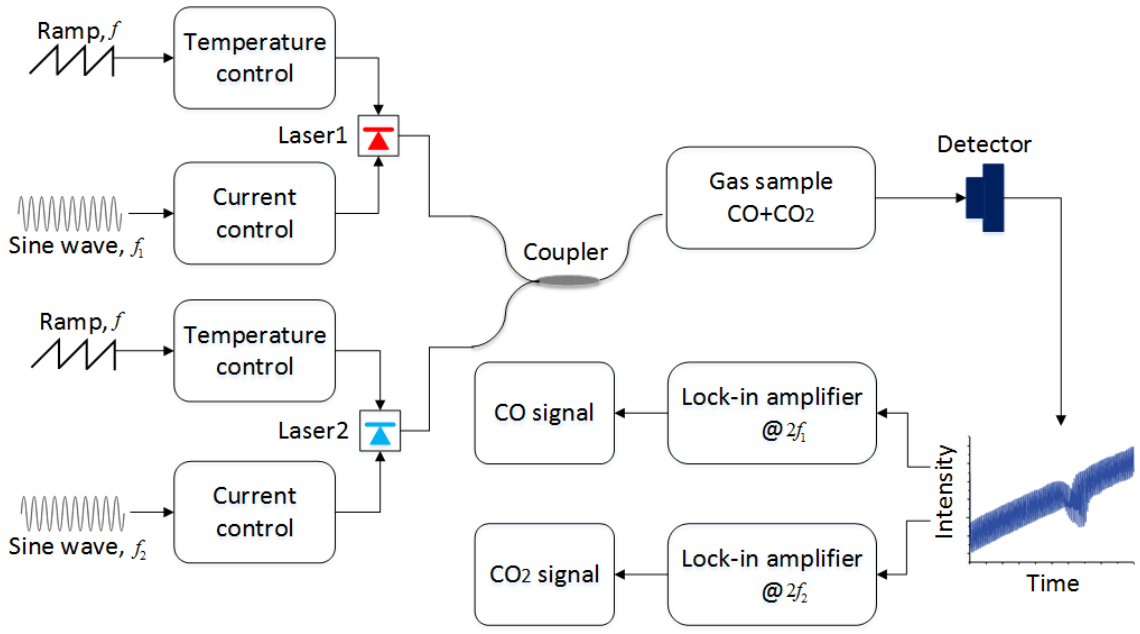

Figure 2.5. Experiment setup for simultaneous detection of two gases (CO and CO_2).

Figure 2.6 shows an exemplary system configured to simultaneously detect methane (CH_4), carbon dioxide (CO_2), and carbon monoxide (CO) in underground coal

mines [52]. Additional or alternative gases could also be selected for detection and measuring. One or more gas sensor probes may be used in such a multiple gas monitoring system. In this example, two sensor probes are deployed at remote locations for mine safety.

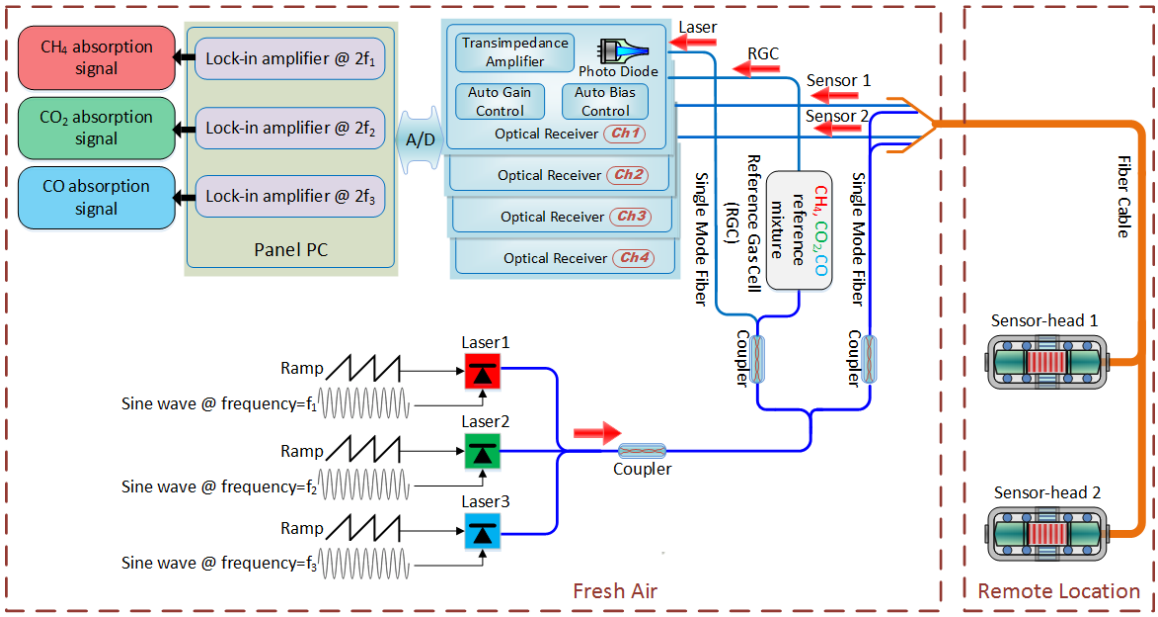

Figure 2.6. Designed system for remote monitoring of multiple gases in underground coal mines [52].

A multiple gas monitoring system is an extension of a single gas sensing system. It is likewise based on absorption spectroscopy and relies on absorption lines at different wavelength bands to detect different gases separately. The system is configured to detect and measure absorption lines for each of a plurality of detectable gases, where the absorption lines relied upon are selected so as to have no overlap from one gas to another. As shown in Figure 2.6, each gas of the plurality of detectable gases is allotted a separate laser module. For this exemplary system, the particular wavelengths at which absorptions (or conversely, transmittances) may be detected and measured are listed in Table 2.1.

Table 2.1. Center wavelength for different gases

Gas	Laser peak wavelength (nm)
Methane	1651
Carbon dioxide	1577
Carbon monoxide	1566

The laser signals for each of the gas monitoring modules is combined by optical couplers and this combined laser signal is then divided by one or more couplers to supply optical signal to (a) an input channel of an optical receiver module, (b) a reference gas cell (RGC), and (c) each of one or more sensor probes arranged to allow detection and monitoring of the gases. In Figure 2.6, both of the two sensor probes are arranged to detect all three gases (i.e. CH_4, CO, and CO_2).

The combined laser optical signals for a given sensor probe is launched into a single mode fiber which runs to that sensor probe. After the optical signal has passed through the gas chamber of the gas sensor probe, the optical signals transmitted back from the gas sensor probe are routed to an input channel of the optical receiver module where it is processed to generate a concentration measurement. It is important to note that besides the two sensor channels from remotely located sensor probes, there are two additional channels being detected at the optical receiver module in Figure 2.6. These two channels, namely *Laser* and *RGC*, are used for better gas absorbance recovery[1]. The Laser channel carries the direct optical signal from DFB lasers without interacting with any surrounding gases, and RGC channels carries optical signal from gas absorptions in a Reference Gas Cell containing fixed mixture (i.e. 4.76% CH_4, 47.62% CO, and 47.62% CO_2) of gases.

Figure 2.7 (a) and (b) depict the second harmonic signals simultaneously measured from absorptions by carbon monoxide (CO) and carbon dioxide (CO_2) respectively using experiment setup in Figure 2.5.

[1] A discussion on how *Laser* and *RGC* signals are used for improved absorbance recovery can be found in Appendix A.

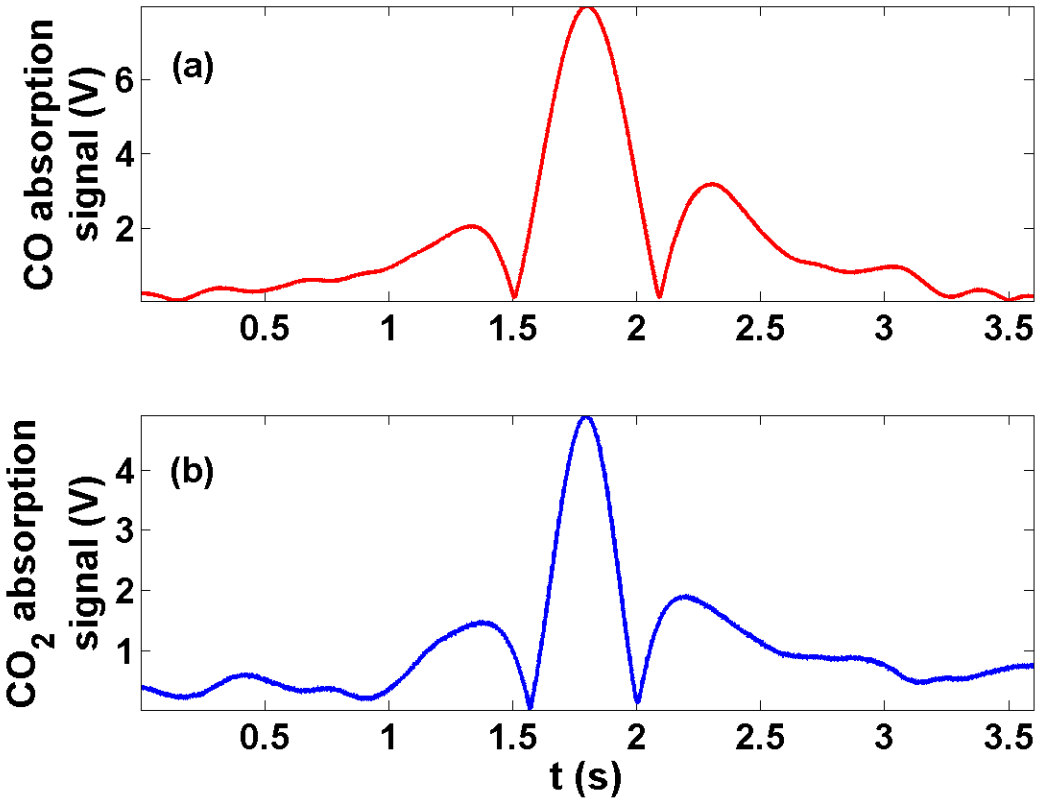

Figure 2.7. Simultaneously measured second harmonic signal from (a) CO absorption, (b) CO_2 absorption.

First and second harmonic signal from methane (CH_4) absorption at three different concentrations are shown in Figure 2.8 and Figure 2.9 respectively.

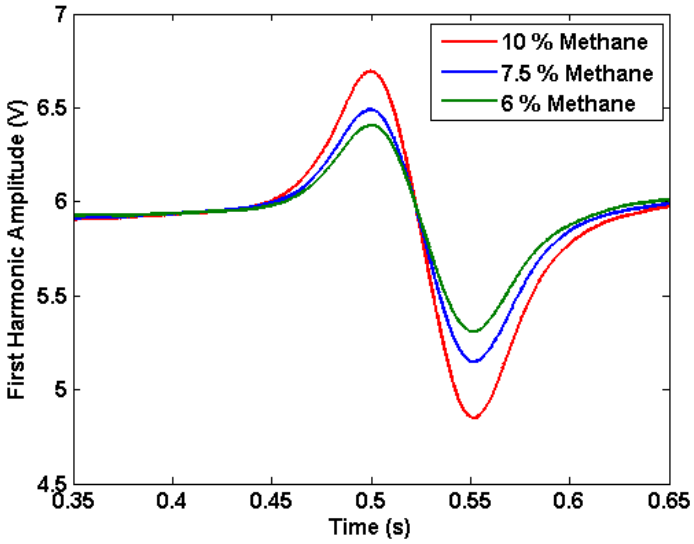

Figure 2.8. First harmonic signal from CH_4 absorption at different concentrations.

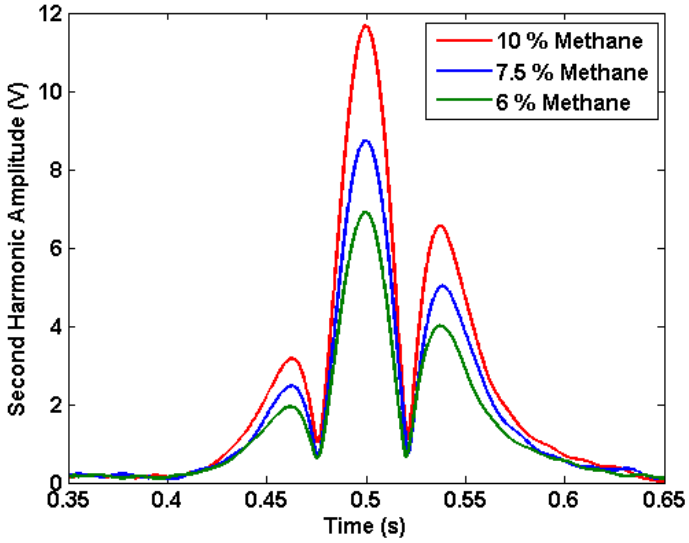

Figure 2.9. Second harmonic signals from CH_4 absorption at different concentrations.

2.3 Spatially Distributed Gas Monitoring

In the following section, a brief overview of recent developments in spatially distributed gas monitoring systems is presented.

2.3.1 Spectroscopy Based Distributed Optical Gas Sensing

Quasi-distributed gas sensing using spectroscopy was first proposed by Zavrsnik et al [35–37]. They used a combination of interferometric mixing and frequency modulated continuous wave (FMCW) method to distinguish between different open path micro-optic gas sensing units arranged in series. Each sensing unit or cell was constructed using two capillaries, two collimating GRIN lenses and a supporting V-groove alignment block. With two glass-air interfaces for each cell, it worked like a Fabry-Perot interferometer. The time delay between the two reflections, along with the linear frequency ramp of the laser source, gave rise to beat frequencies in the mixed output. By using different cavity lengths for the interferometers, each individual sensing cell could be identified by its power spectrum in the frequency domain. When target gas was present in the cavity, it attenuated the amplitude of signal passing through the sensing cell, resulting in a decrease in the power spectrum amplitude for a given measurement point. Although this technique is not gas specific, it has several other limitations. Firstly, the cell length has to be kept unique and smaller than the coherence length of light source for interferometric mixing to work. Secondly, frequency output of the diode laser needs to be varied in a linear fashion by a linear current ramp. Thirdly, connecting fibers are necessary between two successive sensing cells such that their separation is greater than the coherence length of the source and two different cells do not interfere. Fourthly, different cell lengths does not completely ensure their separation from cross-terms which are the result of undesired interference between any two optical paths associated with more than one sensor in a system. And finally, unlike single point monitoring with TDLS systems, the recovery of full absorption response spectrum, $\alpha(\nu)Cl$, is not possible by this approach. Later Guan et al modified this design to include a scanning Michelson interferometer to realize quasi-distributed gas sensing by coherence multiplexing only [38]. This avoids the frequency (wavelength) modulation of the diode laser and allows a narrowband absorption sensing. But all other limitations from interferometric mixing still remain.

Lu et al have proposed another concept of quasi-distributed region selectable gas sensing [39]. Their design uses long propagation fiber, two collimator based gas cell as sensing probe, and fiber Bragg grating (FBG) reflector as region selector. The peak

reflection wavelength of the FBG is synchronized with the target gas absorption line center and it is laid behind the sensing probe to reflect. From this FBG reflection signal, the location and species of the leakage can be analyzed. However, this sensor design also has several limitations. Firstly, a different absorption line needs to be selected for each sensing probe. This can be very difficult to realize by a diode laser which has limited wavelength scanning range and broadband source is the only option. Secondly, FBG reflection peaks need to wavelength synchronized with target gas absorption lines. So multiple gases cannot be monitored with the same sensing fiber. Also, switching to a different target gas requires changing all the FBG reflectors. Thirdly, the total number of locations at which gas sensing can be done is limited by the wavelength span of the source and number of gas absorption lines available in that span. Fourthly, peak reflection wavelength of typical FBG at 1550 nm band has approximately 10 pm shift over 1 degree C temperature change. This drift can easily desynchronize the FBG reflector and absorption line. Therefore, an athermal packaged FBG with passive or active temperature compensation is required. And finally, the recovery of full absorption response spectrum is not possible by this approach as well.

2.3.2 Non-spectroscopy Based Distributed Optical Gas Sensing

Distributed gas sensing by non-spectroscopic technique have been limited to a specific gas. Sumida et al. were first to report a distributed hydrogen measurement with fiber-optics [53]. They used 100 um silica core and coated with platinum-supported tungsten oxide (Pt/WO_3) thin film to make the cladding hydrogen sensitive. In the presence of hydrogen, WO_3 is reduced to tungsten bronze (H_xWO_3). So the refractive index of the thin film cladding also changes since dielectric constant of WO_3 and H_xWO_3 have different values. Therefore, optical power propagating through the fiber core gets strongly influenced by the change in evanescent field absorption coefficient and refractive index of cladding. Then, hydrogen concentration is determined from the transmission loss of the fiber-optic sensor. Commercial OTDR instrument is used to monitor this fiber transmission loss and location of hydrogen leakage. However, this technique is limited by cladding material and cannot be used for monitoring gases other

than hydrogen. Also, it cannot measure the full absorption response spectrum for target gas.

Wu et al have reported a three fiber grating based sensing module to U.S. Department of Energy which can be used for constructing distributed gas sensing instrumentation [40]. The design of the three fiber-grating is explained in Figure 2.10. The sensing module is based on a fiber long period grating (LPG) with coated sensing material around the grating cladding. The sensing material is specific to the gas (e.g. Pd/SiO_2 nanocomposite for hydrogen detection and $SiO_2/SnO_2/Pd$ for carbon monoxide detection) and is deposited on fiber gratings by sol-gel process or sputtering. Since the forward propagating cladding modes induced evanescent field for the LPG is located at its cladding/air interface, changes in the refractive index of above mentioned sensing materials influences the LPG's LP_{01} mode. In their sensing module, first FBG provides initial signal power reference, and second FBG provides a broadband reflection for reflectance based sensing. Also, the central wavelength of the FBG_1 should be far away from the transmission LP_{01} mode wavelength, while that of FBG_2 could be at the same wavelength as LPG's LP_{01} mode for maximum sensitivity or response amplitude. For distributed measurement, several sensing modules can be cascaded along an optical fiber and wavelength division multiplexing (WDM) can be used to separate their response at the detector. But this approach also has some disadvantages. Firstly, when designed for multiple fiber gas sensors in one fiber cable, all LPGs should be separated by at least 10 nm to avoid any interference and to achieve better transmission peaks tracking. Hence, the laser source must have a large wavelength span. Secondly, deposited sensing material on LPG needs to be changed when target gas is changed. Thirdly, it cannot measure the full absorption response spectrum for target gas.

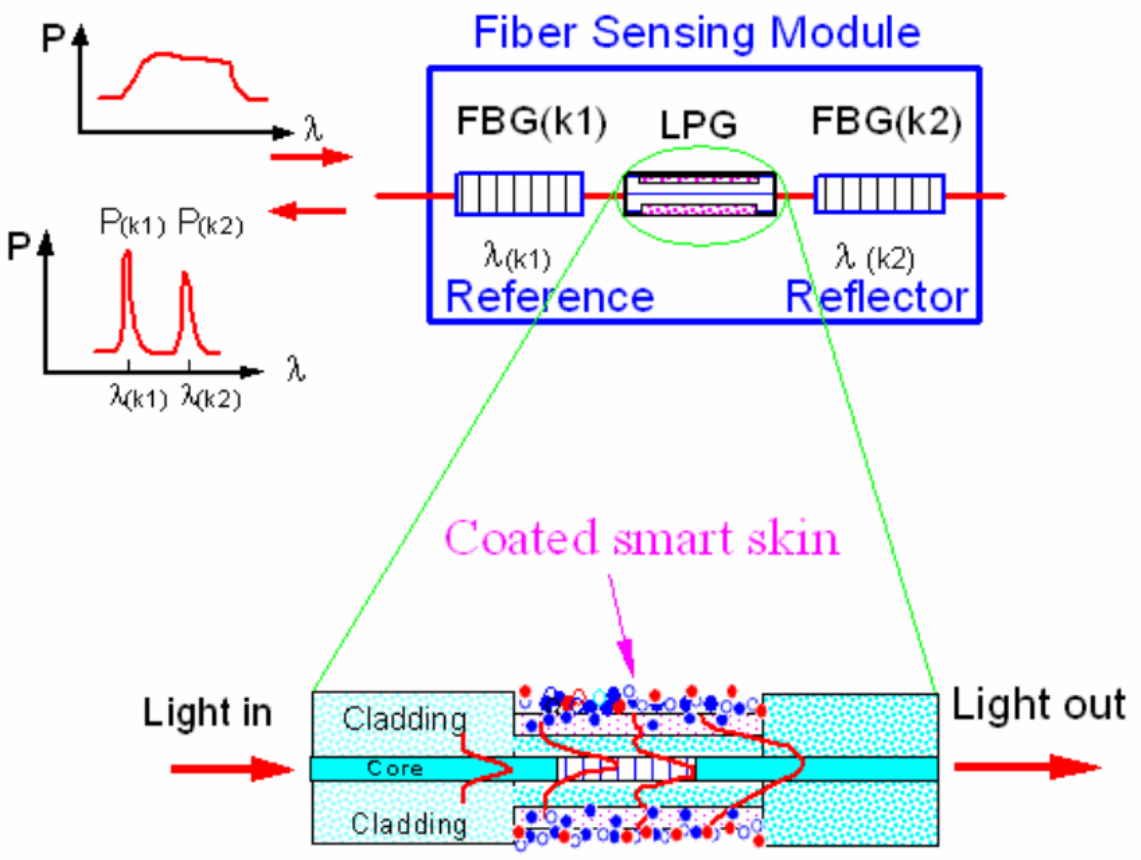

Figure 2.10. Three fiber-gratings based sensing modulus for fossil fuel gas sensing [40].

A distributed hydrogen monitoring based on travelling LPG in single mode fiber has also been proposed by Wang et al [41]. The fiber is coated with a platinum (Pt) catalyst layer and travelling LPG is generated by an acoustic pulse propagating along the fiber. The Pt-coated fiber section is heated by the thermal energy released form Pt-assisted combustion of hydrogen (H_2) and oxygen (O_2). The temperature change from the combustion results in a measurable wavelength shift in the transmission spectrum of the travelling LPG. An advantage of this system is that it allows the reconstruction of LPG spectrum at any location of the fiber. Thus it realizes fully distributed sensing of gas. But this approach requires a different coating materials for different gases which increases its complexity. Furthermore, a widely tunable laser source is needed to scan and track LPG transmission peak.

In summary, current distributed gas sensing techniques are often complex or gas specific. This increases the total cost of the gas monitoring system significantly. Additionally, a

recovery of full absorption response spectrum is not possible by any of the above methods. As discussed in Section 2.1, gas absorption response $\alpha(\nu)$ changes significantly with pressure and temperature change. Without capturing, the complete absorption response, it is very difficult to estimate true concentration for most practical application.

Chapter 3 Strategy for Estimation of Gas Parameters from Absorption Response

As described earlier in Section 2.1, measured absorption response $\alpha(\nu)$ from a gas is affected by parameters like pressure and temperature of the environment. Therefore, using a Voigt curve fit for absorption response, it is possible to extract these parameters besides concentration.

For TDLS with direct detection, absorption response is obtained from $I_{out}(t)$ after normalizing it by the non-absorbing sections of I_{out} (or baseline intensity). On the other hand, absorption response for WMS systems can be calculated from $\Delta I \bullet \cos(\omega t) - \Delta I \bullet \alpha(\bar{\nu}) \bullet Cl \bullet \cos(\omega t)$ term in first harmonic after the RAM and FM/AM terms have been separated. The techniques to separate these two terms present in WMS harmonics is discussed in Chapter 4.

3.1 Voigt Profile Fitting

As there is no closed form expression for Voigt profile given in Eq. (2.9), an analytical approximation given by McLean et al is used for this research [45]. Assuming that laser emission wavenumber changes linearly with time, i.e. $\nu(t) = const \times t + \nu_{start}$, due to thermal scan, Eq. (2.9) can be rewritten in time domain after some rearrangement of the terms.

$$\phi_V(t) = a_L \frac{2}{\Delta\nu_D}\sqrt{\frac{ln2}{\pi}}V(X,Y) \tag{3.1}$$

where a_L is signal amplitude scaling factor during detection, $X = \frac{2\sqrt{\ln 2}}{\Delta\nu_D}(t - t_0)$, $Y = \frac{\Delta\nu_C}{\Delta\nu_D}\sqrt{\ln 2}$, $\nu(t_0) = \nu_0$, and V(X,Y) is given by the analytical expression in Eq. (3.2).

$$V(X,Y)=\sum_{i=1}^{4}\frac{C_i(Y-A_i)+D_i(X-B_i)}{(Y-A_i)^2+(X-B_i)^2} \tag{3.2}$$

Coefficients $A_i \to D_i$ are obtained from the table provided by McLean et al [45]. Following Eq. (3.1) and (3.2), the measured absorption response is least-square fitted to a Voigt shape by Levenberg-Marquardt (L-M) algorithm. The four parameters are used for the fitting process are $a_L, \Delta\nu_C, \Delta\nu_D$, and t_0. While collisional broadening width ($\Delta\nu_C$) and Doppler broadening width ($\Delta\nu_D$) are given a wider range of initial guesses, the other two parameters are selected around the peak value and location of measured absorption response. After the fitting algorithm converges, gas concentration, pressure and temperature are extracted from the final values of $a_L, \Delta\nu_C$, and $\Delta\nu_D$.

3.2 Estimation of Different Gas Parameters

3.2.1 Concentration

Gas concentration is proportional to the amplitude of the Voigt function, i.e. a_L. With the value of a_L known from least square fitting, the gas concentration can be easily determined.

3.2.2 Temperature

Gas temperature can be estimated from fitted value of $\Delta\nu_D$ using Eq. (2.6). But this method may not yield accurate result if Gaussian broadening is not very prominent. In such cases, two absorption lines technique proposed by Goldenstein et al can be used to measure gas temperature [54].

3.2.3 Pressure

Gas pressure can be easily estimated from Eq. (2.8), if temperature has already be determined or is nearly constant. Parameters like broadening coefficient γ_j and temperature exponent n_j can be obtained from HITRAN database [55]. Note that under

fixed temperature condition, gas pressure is directly proportional to FWHM of measured absorbance. However, if information on temperature change is not available, a reference gas cell with fixed concentration and pressure of target gas is required for absorbance comparison.

3.3 Simulation Results

To check the efficacy of parameter extraction by L-M algorithm and analytical approximation of Voigt profile in Eq. (3.2), several absorption responses are simulated in MATLAB. Gaussian noise is also added to these spectra such that signal-to-noise ratio is 20 dB to mimic real measurement data. All four parameters ($a_L, \Delta\nu_C, \Delta\nu_D$, and t_0) are extracted by least square fitting. Then true parameter values are compared against those obtained from curve fitting. The simulation results for three possible measurement scenarios are described below.

3.3.1 Case 1: Doppler width < collision/pressure width

This situation occurs when gas absorption measurements are done near or above atmospheric pressure ($P \geq 101\,\text{kPa}$ or 14.7 psi). In such environment, pressure broadening or collisional broadening is dominant and temperature induced narrowing is not significant.

Parameters used for simulating absorbance: $a_L = 0.5, \Delta\nu_D = 0.1, \Delta\nu_C = 0.2, t_0 = 1$

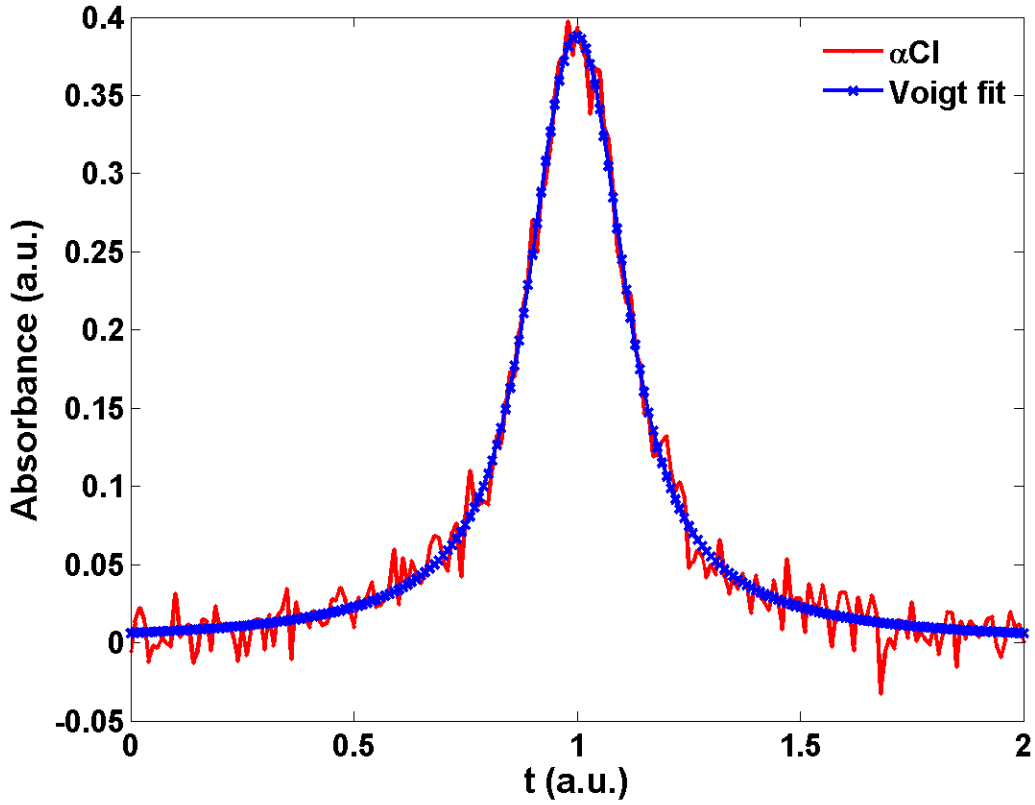

Figure 3.1. Absorption signal with collision broadening dominance.

The initial guess value of the parameter provided to L-M algorithm, the true value for the parameter, the fitted value of the parameter after convergence, asymptotic standard error of the parameters (σ_p), and percentage error in the parameter $=100\times\frac{\sigma_p}{fit\ value}$ are listed in Table 3.1.

Table 3.1. Fitting parameters

Parameter	Initial guess	True value	Fit value	σ_p	% error
a_L	0.397	0.5	0.536	0.0267	4.9
$\Delta\nu_D$	0.050	0.1	0.118	0.0155	13.1
$\Delta\nu_C$	0.050	0.2	0.183	0.0103	5.7
t_0	0.980	1.0	0.999	0.0012	0.1

3.3.2 Case 2: Doppler width > collision/pressure width

This situation is true for gas absorption measurements at low pressure ($P \leq 30$ kPa or 4.3 psi). In such conditions, Doppler broadening is dominant due to weak contribution from collisional broadening. The final absorption profile is kind of a hybrid response with a Doppler center and Lorentz wings.

Parameters used for simulating absorbance: $a_L = 0.5, \Delta\nu_D = 0.15, \Delta\nu_C = 0.1, t_0 = 1$

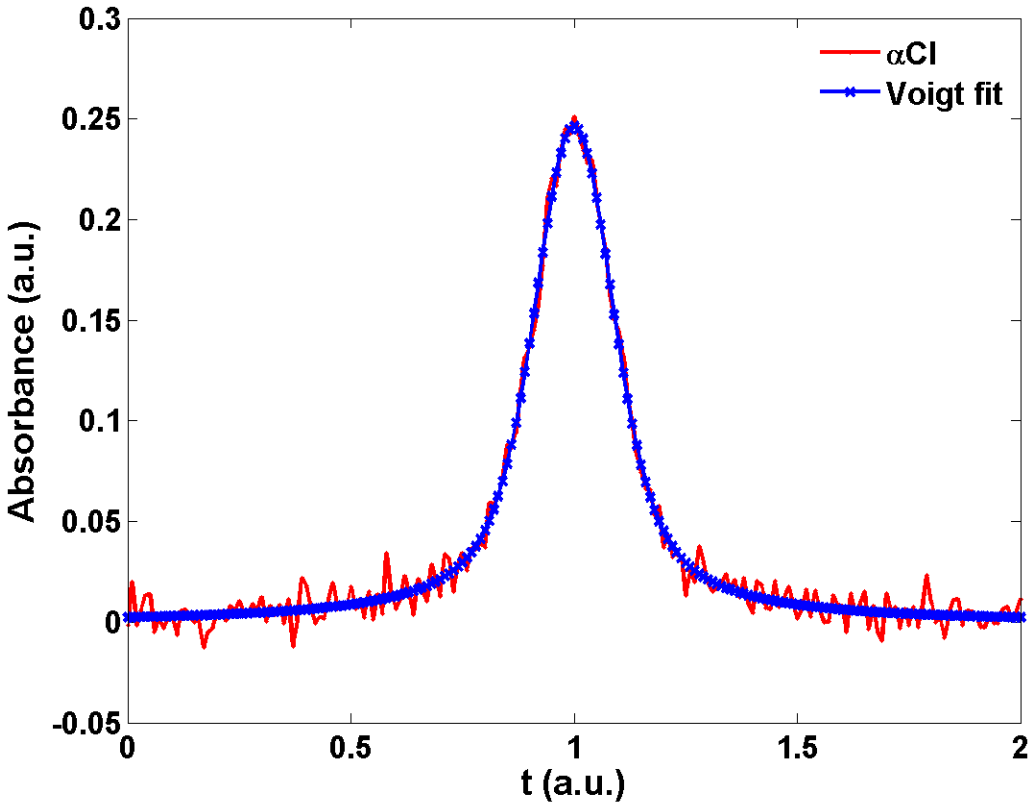

Figure 3.2. Absorption signal with Doppler broadening dominance.

The initial guess value of the parameter provided to L-M algorithm, the true value for the parameter, the fitted value of the parameter after convergence, asymptotic standard error of the parameters (σ_p), and percentage error in the parameter $= 100 \times \frac{\sigma_p}{fit\ value}$ are listed in Table 3.2.

Table 3.2. Fitting parameters

Parameter	Initial guess	True value	Fit value	σ_p	% error
a_L	0.502	0.5	0.4721	0.0297	6.3
$\Delta\nu_D$	0.075	0.15	0.1463	0.0075	5.1
$\Delta\nu_C$	0.025	0.1	0.1061	0.0074	7.0
t_0	1.000	1.0	0.9998	0.00098	0.1

3.3.3 Case 3: Doppler width ≈ collision/pressure width

This case is true for gas absorption peaks near but lower than atmospheric pressure (between 30 kPa to 60 kPa). In such environment, Doppler broadening may be comparable to Lorentz broadening.

Parameters used for simulating absorbance: $a_L = 0.5, \Delta\nu_D = 0.1, \Delta\nu_C = 0.1, t_0 = 1$

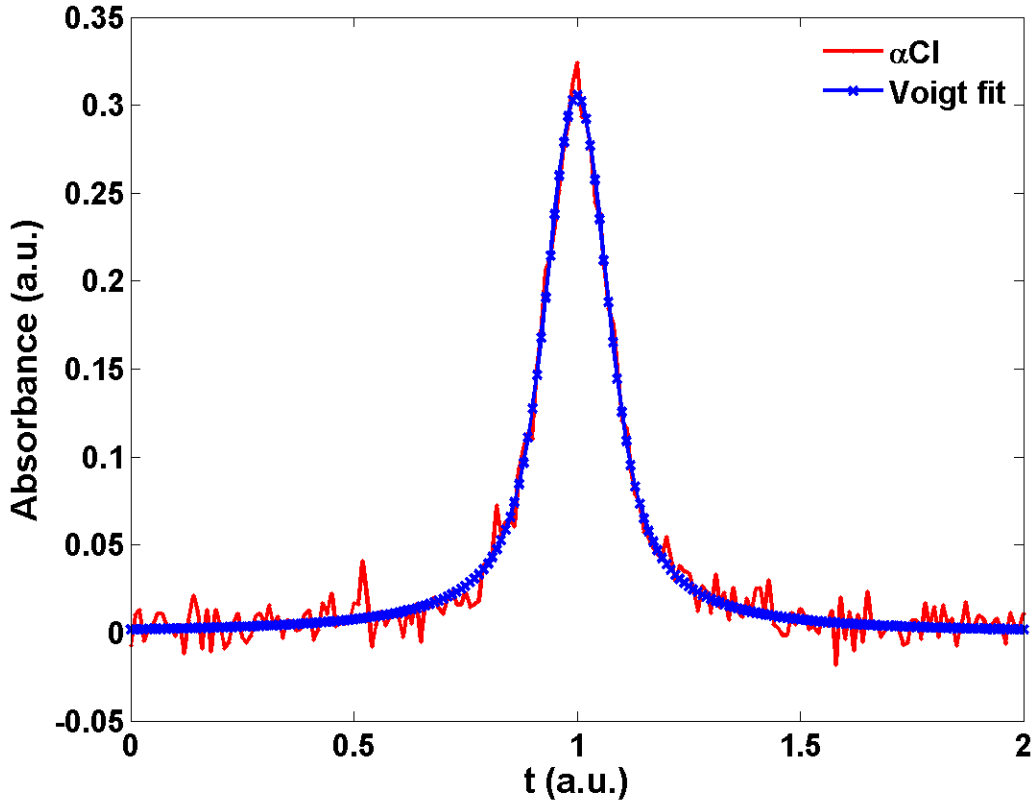

Figure 3.3. Absorption signal with equal effect from collisional and Doppler broadening.

The initial guess value of the parameter provided to L-M algorithm, the true value for the parameter, the fitted value of the parameter after convergence, asymptotic standard error of the parameters (σ_p), and percentage error in the parameter $=100\times\frac{\sigma_p}{fit\ value}$ are listed in Table 3.3.

Table 3.3. Fitting parameters

Parameter	Initial guess	True value	Fit value	σ_p	% error
a_L	0.648	0.5	0.4984	0.0304	6.1
$\Delta\nu_D$	0.050	0.1	0.1002	0.0075	7.5
$\Delta\nu_C$	0.025	0.1	0.1005	0.0070	6.9
t_0	1.000	1.0	0.9994	0.0009	0.1

It is evident that Voigt profile fitting parameters can be successfully extracted even from a noisy absorption signal with high accuracy under varying pressure and temperature conditions. Consequently, target gas concentration, pressure and temperature can also be extracted with similar accuracy. In the following chapter, an experimental demonstration of gas pressure and concentration estimation from the RAM contributions in WMS harmonics is presented.

Chapter 4 Strategy for Calibration-free Single Point Gas Detection using Diode Lasers

4.1 Motivation

Most industrial gas monitoring systems require a setup that can run for extended period of time (typically years) without any need for calibration. However, in a traditional WMS scheme, calibration becomes necessary as the measured harmonics have contributions from frequency as well as amplitude modulation. As explained in Section 2.2.2, without the presence of RAM, measured n^{th} harmonic signal would be purely from FM/AM and proportional to n^{th} derivative of absorption line shape function at small frequency modulation amplitudes [23,24]. However, in practical systems, RAM contributions to measured harmonic is often significant and produces distortions at all harmonic frequencies. Furthermore, measurements at first harmonic frequency is affected by an additional background RAM which is independent of gas concentration [24]. Hence, signal processing for a WMS system is often complex.

In this chapter, a simple yet novel strategy is presented to separate RAM and FM/AM contributions in measured harmonics. After their separation, a normalization technique is discussed to eliminate the dependency of absorption signal on laser parameters like I and ΔI. Variations in these intensity parameters may occur over time for reasons like laser output intensity change due to aging, collimator misalignment in gas measurement cell, optical fiber loss due to bending, optical or electronic gain change in photo-receiver circuit etc. Therefore, key to a calibration-free WMS system is to remove influence of laser parameters and use the absolute absorption line shape function, $\alpha(\nu)Cl$, for all gas parameters estimation.

4.2 Model for Signal from Wavelength Modulation Spectroscopy (WMS)

In conventional WMS, LIA phase (x-axis) is aligned with the RAM term for harmonic detection. But due to the phase lag ψ of FM/AM term from RAM term, LIA measures a summation of the RAM term and the projection of FM/AM term on x-axis. Here, we

must stress that ψ is not a constant parameter and is a function of modulation frequency f_m. For a diode laser, thermally induced FM is intrinsically π out of phase with the intensity modulation and further lags it by an additional frequency dependent component that can be as large as 0.35π for a modulation rate of 250 kHz [29,56]. Consequently, the contribution of FM/AM term can vary from one modulation rate to another, even though all other laser parameters, i.e. $I, \Delta I, \delta\nu$, remain the same.

For further discussion, we examine the two harmonic signal components measured by the LIA: In-phase or X-component and Quadrature phase or Y-component. If the reference frequency for the LIA is phase aligned with the RAM signal, the X, Y components, and amplitude R for first harmonic can be expressed by Eq. (4.1).

$$\begin{aligned} X_{1f} &= \frac{1}{2}\left[\begin{array}{l} \Delta I - \Delta I \bullet Cl \bullet \alpha(\bar{\nu}) \\ -I(\bar{\nu}) \bullet Cl \bullet \alpha'(\bar{\nu}) \bullet \delta\nu \bullet \cos(\psi) \end{array}\right] \\ Y_{1f} &= \frac{1}{2}\left[I(\bar{\nu}) \bullet Cl \bullet \alpha'(\bar{\nu}) \bullet \delta\nu \bullet \sin(\psi)\right] \\ R_{1f}(\bar{\nu}) &= \sqrt{X_{1f}{}^2(\bar{\nu}) + Y_{1f}{}^2(\bar{\nu})} \end{aligned} \tag{4.1}$$

Similarly, X, Y components and amplitude R for second harmonic are expressed by Eq. (4.2).

$$\begin{aligned} X_{2f} &= -\frac{1}{4}\left[\begin{array}{l} \Delta I \bullet Cl \bullet \alpha'(\bar{\nu}) \bullet \delta\nu \bullet \cos(\psi) \\ +I(\bar{\nu}) \bullet Cl \bullet \dfrac{\alpha''(\bar{\nu})}{2} \bullet \delta\nu^2 \bullet \cos(2\psi) \end{array}\right] \\ Y_{2f} &= \frac{1}{4}\left[I(\bar{\nu}) \bullet Cl \bullet \frac{\alpha''(\bar{\nu})}{2} \bullet \delta\nu^2 \bullet \sin(2\psi)\right] \\ R_{2f}(\bar{\nu}) &= \sqrt{X_{2f}{}^2(\bar{\nu}) + Y_{2f}{}^2(\bar{\nu})} \end{aligned} \tag{4.2}$$

Note that, in the absence of gas absorption, first harmonic signal amplitude is $0.5\Delta I$ and it is the background RAM, R^0_{1f}. Also, X and Y components for second harmonic signal are not affected by this background signal.

4.3 Existing Methods for Realizing Calibration-free Measurement with WMS

In the following subsections, two most popular calibration-free methods for WMS systems are discussed along with their limitations.

4.3.1 Background RAM estimation from isolated RAM

As shown in Eq. (4.1), RAM and FM/AM components in first harmonic signal have a phase separation ψ . If the RAM component can be isolated from first harmonic signal, its non-absorbing spectral wings can be used to estimate R^0_{1f} in the complete laser scanning range [23–26]. This can be done by using some polynomial curve fitting on those wings. Then estimated R^0_{1f} can be used to normalize measured RAM signal for finding an intensity independent absorption profile, i.e. $R_{1f}' = R_{1f} / R^0_{1f} = 1 - \alpha(\bar{\nu})Cl$.

Researchers at University of Strathclyde have proposed many techniques to recover or measure isolated RAM signal from first harmonic, namely, FM/AM nulling with appropriate lock-in amplifier phase selection [24]; phasor decomposition [25]; background RAM suppression [27]; and phase quadrature modulation frequency operation [51]. However, this *background RAM estimation* method has several limitations. Firstly, in the presence of nearby absorption peaks from the target gas or other background gases, estimated background RAM would be incorrect. Secondly, wavelength scanning range of the diode laser must be wide enough to cover the full absorption profile and some additional spectrum where gas absorption is completely absent. For such large laser wavelength tuning range, variations in parameters such as $I(\bar{\nu}(t))$, $\Delta I(\bar{\nu}(t))$ and $\bar{\nu}(t)$ is large and often nonlinear. Thus curve fitting does not always give a good estimate on their behavior. It is possible to use separate detection channels for measuring the nonlinear changes in laser intensity and frequency without any gas interaction. But, in that case, any variation in $I(\bar{\nu}(t))$ and $\Delta I(\bar{\nu}(t))$ due disturbance at the gas measurement cell channel cannot be correctly estimated. Therefore, this approach is only suitable for measuring gases with well isolated absorption lines in low atmospheric pressure conditions.

4.3.2 First harmonic normalization for WMS

Most widely used techniques to get a calibration-free WMS system is second (2f) harmonic measurement with first harmonic (1f) normalization. This technique was pioneered by Cassidy and Reid for second harmonic signal measurement in turbulent atmospheric conditions [5]. Several decades later, researchers at Stanford University used the same principle for measuring second and higher harmonic signals to achieve a calibration free measurement system in high pressure gas chambers [29–31,33,34]. This normalization approach works well even for pressure broadened absorption lines where the laser cannot be tuned to the non-absorbing spectral wings of harmonic signal. However, their method requires a pre-characterization of the laser to estimate all of its parameters, i.e. $I, \Delta I, \psi, \Delta\nu$, before any measurement. Although laser pre-characterization is not difficult, variations in these parameters due to several factors such as drift from pre-characterization test conditions, temperature variations, physical damage or bending in the optical fiber connecting the laser, detector and gas measurement cell, and aging of laser diode would cause errors in future measurements. In fact all operating conditions, including modulation frequency (f_{m}), need to remain fixed during measurement cycle. Another important limitation to this method comes from the interplay of RAM and FM/AM contributions to the measured WMS harmonics. To understand this issue, we have to examine the concept behind *first harmonic normalization*.

At low optical depth ($\alpha Cl < 0.05$) and zero FM/AM contributions, first harmonic signal amplitude is a good approximation of ΔI as $R_{1\mathrm{f}} = 0.5\Delta I\left[1-\alpha(\bar{\nu})Cl\right] \approx 0.5\Delta I$ (See Eq. (4.1) for details). Therefore, normalizing the second or higher harmonics by the first harmonic signal amplitude will remove any common perturbation in ΔI . This is very useful concept, because any optical intensity change at the gas measurement cell due to vibrations, optical misalignment, bending of connection fibers, or variations in detector gain is estimated in real time from $R_{1\mathrm{f}}$. Naturally, if higher harmonics are normalized by this approximated ΔI , some error is added in the process. This error is the highest at the absorption line center and is equal to the maximum value of αCl (also known as optical depth) [29].

But in most practical WMS systems, it is incorrect to ignore FM/AM contributions. For instance, if $\Delta I / I$ is small and $|\cos(\psi)| \approx 1$, FM/AM term could be comparable or even larger than RAM term in the first harmonic. As the values of $\Delta I / I$ and ψ can easily show large variations from one diode laser to another for the same target $\delta\nu$ value, it is impossible to avoid this problem altogether. Furthermore, ψ dependency puts a restriction on modulation frequency (f_m) as they are interdependent. Figure 4.1 shows simulated values for the ratio of first harmonic signal amplitude (R_{1f}) and background RAM (R^0_{1f}) as $\Delta I / I$ and ψ parameters are changed. For this simulation, $\alpha(\bar{\nu}(t))$ is assumed to be a Lorentz shape with FWHM=0.138 cm^{-1}, WMS system modulation index, $m = 0.11$ and absorption optical depth, $\alpha Cl_{max} = 0.05$. All the remaining parameters are experimentally obtained from a DFB laser diode (Inphenix Inc., Model IPDFD 1602-1110). For *first harmonic normalization* method to work correctly, values of R_{1f} / R^0_{1f} should be between 0.95 and 1 (optical depth being 0.05). However, it is evident from Figure 4.1 that changes in laser operating conditions can add huge errors to this *first harmonic normalization* process.

Several important observations can be made from Figure 4.1. Firstly, first harmonic signal is inherently asymmetric about absorption line center even though Lorentz shape is symmetrical in nature. Hence, higher harmonics normalized by the first harmonic will always be distorted. Secondly, amount of distortion depends on phase shift, ψ , which is a function of modulation frequency, f_m . Thirdly, this normalization error will grow rapidly as $\Delta I / I$ gets smaller than 0.1. Therefore, it is vital to separate the FM/AM contribution from first harmonic signal before using it for normalization of higher harmonics. In the following section, we investigate a simple technique to achieve this goal.

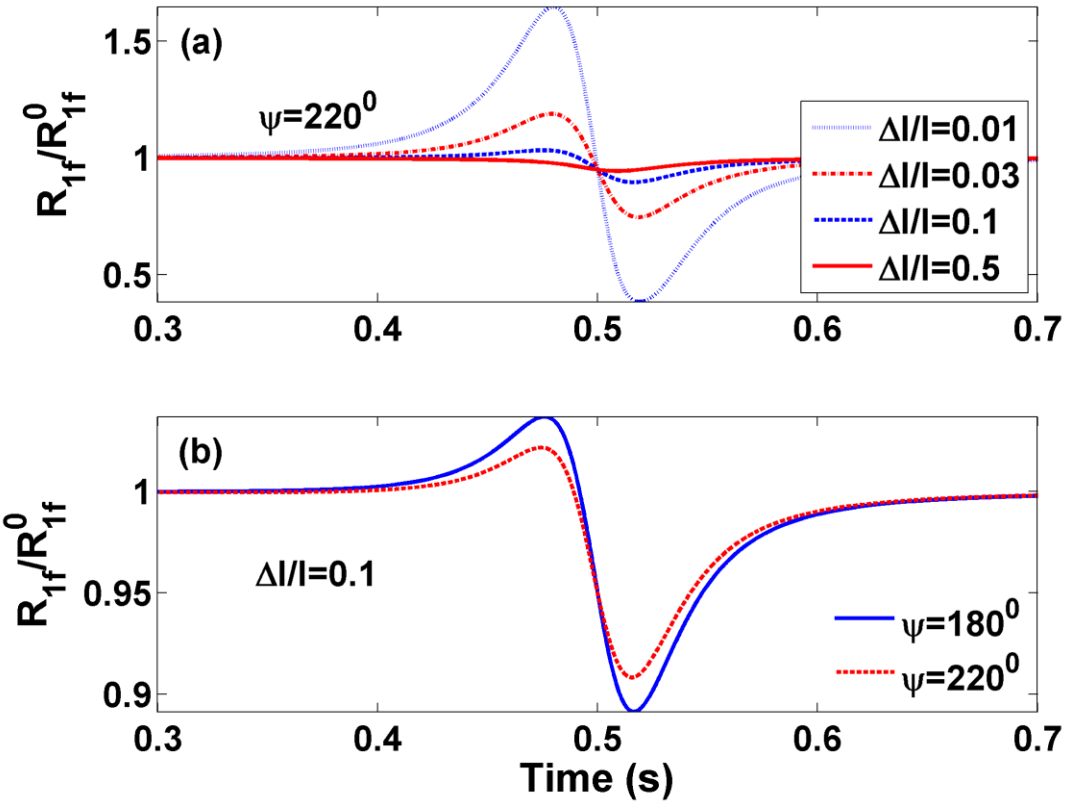

Figure 4.1. First harmonic signal to background RAM ratio (a) at different intensity parameters with $\psi = 220^0$, (b) at different AM-FM phase difference ψ with $\Delta I / I = 0.1$.

4.4 Processing Harmonic Signal from WMS for Calibration-free Measurement

It is clear that *first harmonic normalization* method has distinct advantages over *background RAM estimation* method for realizing a robust calibration free WMS system. But it is absolutely essential to isolate the RAM signal for *first harmonic normalization* to correctly work. One possibility is to apply the lock-in amplifier phase selection method proposed by Duffin et al to measure isolated RAM contributions only [24]. However, this scheme results in a reduction of detected signal amplitude and is highly dependent on the phase difference, ψ, which can easily change when modulation frequency is changed [29,56]. Similarly, background RAM suppression method proposed by Chakraborty et al, although useful, takes many additional optical components like a fiber delay line of appropriate length for the chosen modulation frequency, variable optical

attenuator, and polarization controllers to work [27]. Another possibility is to operate the laser diode at its phase quadrature modulation frequency, where $\psi = 90^0$ (making RAM and FM/AM contributions orthogonal to each other), and measure pure RAM signal. But this frequency is typically >1 MHz for diode lasers which increases the costs of photodetector and associated electronics [28]. Since we aim to apply WMS scheme for simultaneous sensing of multiple gases, which will be detected at different modulation frequencies, it is essential to find a signal recovery scheme that requires least modification to conventional design and has minimal dependence on modulation frequency.

4.4.1 RAM recovery with symmetry approach

Here, we investigate a simple algorithm to recover RAM from X-component of first harmonic. For isolated absorption lines (lines that have negligible broadening contribution from nearby absorption line transitions), absorption profile $\alpha(\nu)$ follows a Lorentzian or Voigt shape which is symmetric by nature. Furthermore, Eq. (4.1) shows that RAM and FM/AM terms nearly follow $\alpha(\nu)$ and $\alpha'(\nu)$ shapes respectively. In Figure 4.2, we have shown the response of $\alpha(\nu)$ and its derivatives calculated from Lorentz distribution provided in Eq. (2.7). A quick examination of the plot reveals that $\alpha(\nu)$ is even symmetric about $\nu - \nu_0 = 0$ axis and its derivatives also have similar properties (i.e. even or odd). This means that harmonic signals are always a sum of even and odd terms. For example, in first harmonic signal expression, RAM term is even symmetric about $\nu - \nu_0 = 0$ axis and FM/AM term is odd symmetric about the same axis. Hence, if the symmetry axis can be accurately located in the measured signal, it is possible to separate RAM and FM/AM term in data processing.

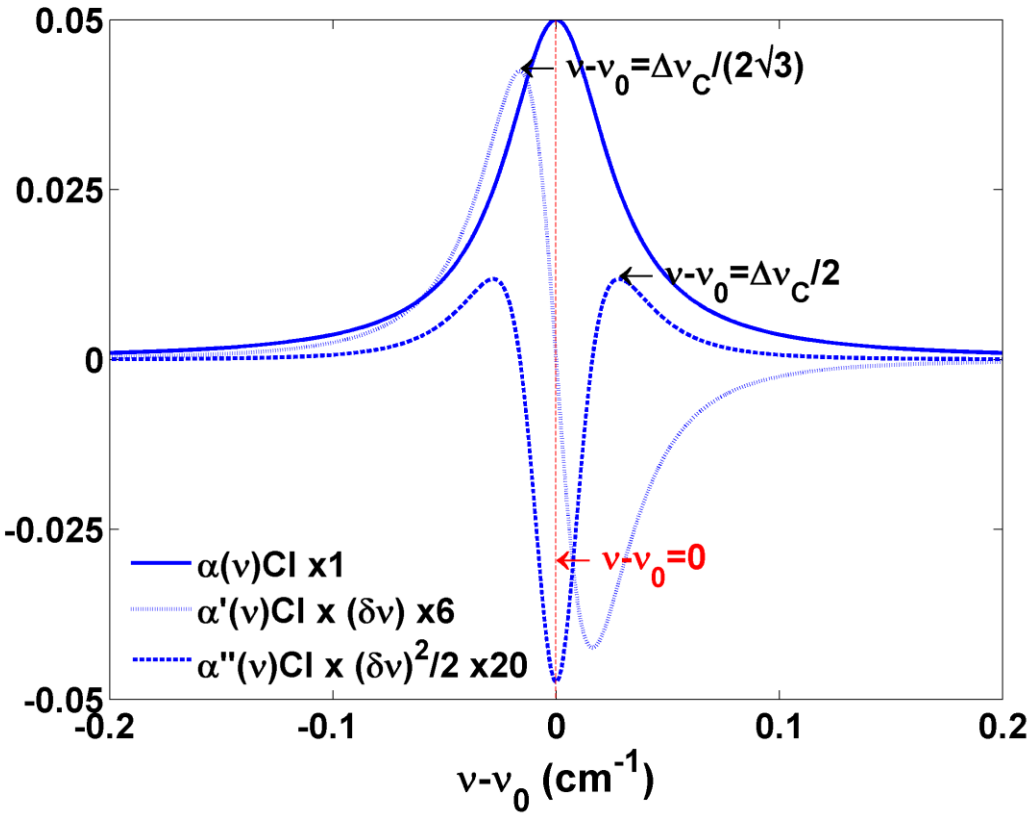

Figure 4.2. Absorption profile $\alpha(\nu)$ and its derivatives at optical depth=0.05 with $\delta\nu = 0.0074\,\mathrm{cm}^{-1}$ (Note that extrema locations of $\alpha'(\nu)$ or $\alpha''(\nu)$ can be used to estimate $\Delta\nu_C$).

One simple method to find the symmetry axis is to use direct absorption signal from the sensor before it goes to a lock-in amplifier. Theoretically, $\nu - \nu_0 = 0$ axis location is same as the position of absorption peak in time domain. If direct absorption signal and X, Y-components of harmonics are measured concurrently, symmetry axis can be located by applying a low pass filter on the former and finding absorption peak position. However, when direct absorption signal is noisy or gas absorption is weak, this technique fails. Therefore, we give a signal correlation method to locate this symmetry axis by using only lock-in amplifier signals.

From Eq. (4.1), it is clear that X-component is significantly distorted by the contributions from RAM and FM/AM. But Y-component is purely from FM/AM. Hence, after the X and Y signals at first harmonic frequency have been digitally sampled, the algorithm described in Figure 4.3 can be used to recover RAM and FM/AM at the same time.

Ideally, $\nu = \nu_0$ axis should be at the zero crossing of the Y-component if $I(\bar{\nu}(t))$ is constant. However, experimentally measured Y-signal does not show this property due to several reasons; (a) $I(\bar{\nu}(t))$ is not constant and may have a nonlinear response in time domain, (b) noise from vibration and laser intensity fluctuations, (c) contributions from higher order derivatives ignored in the simple Taylor series model at low modulation index [24]. Therefore, we select the midpoint of maximum and minimum locations for Y-component as a first guess for the symmetry axis (see Figure 4.4(b)). Using this axis, even and odd parts are separated from X-component. Then odd part of X is correlated with Y to estimate R-squared (R^2) value. To check if the match is optimum, axis location is moved by several data points to both left (negative shift) and right (positive shift) of initial guess and calculated R^2 values are plotted (see Figure 4.5). Once symmetry axis is correctly located for a maximum R^2 , RAM and FM/AM are separately computed knowing that $RAM_{1f} = X_{\text{Even}}$ and $FM/AM_{1f} = \pm\left(Y^2 + X_{\text{Odd}}^2\right)^{0.5}$ (Both positive and negative sign should be considered).

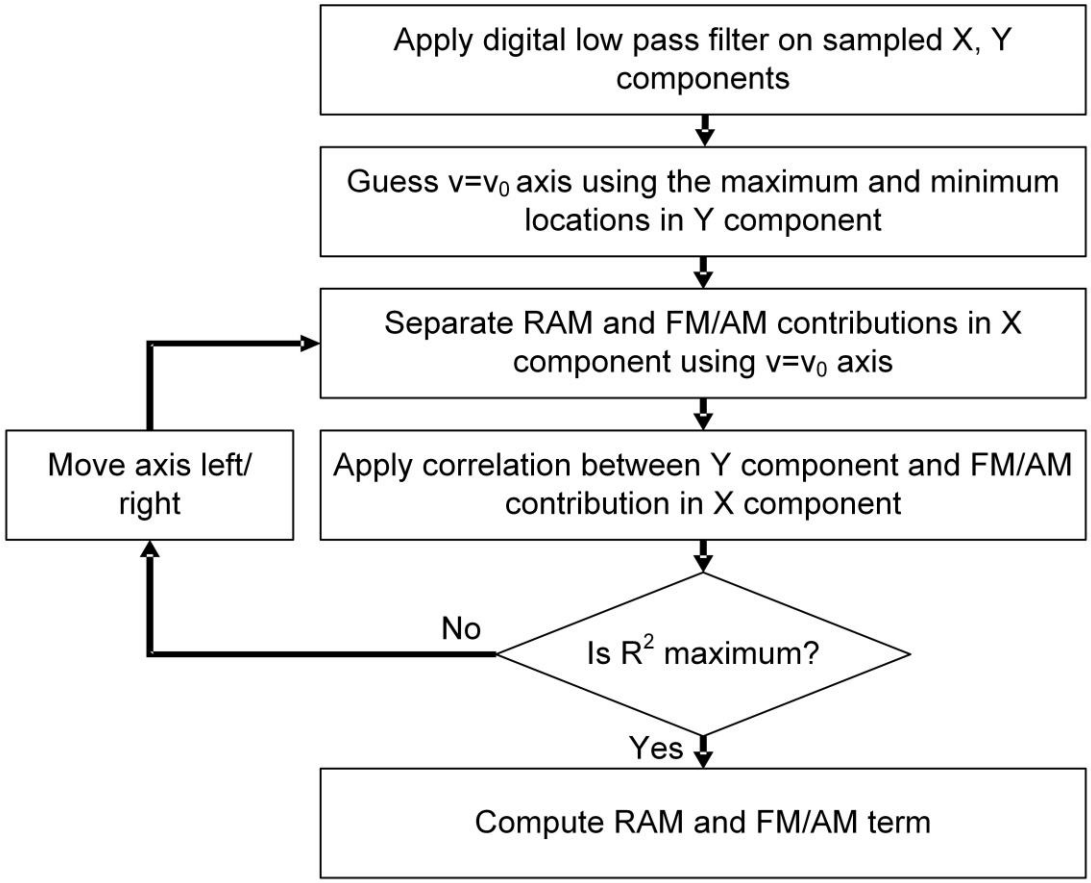

Figure 4.3. Flowchart of algorithm to recover RAM and FM/AM from first and second harmonic signals.

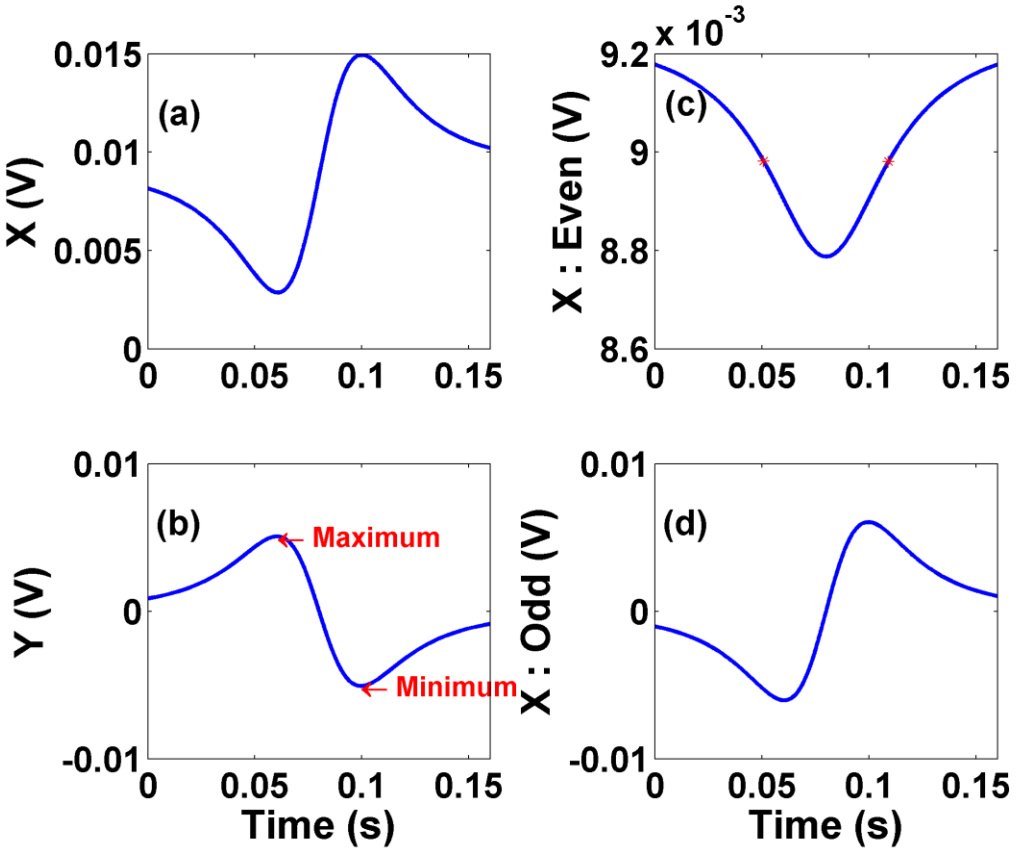

Figure 4.4. (a) X-component, (b) Y-component with maximum and minimum, (c) Computed even contribution (Half maximum points marked) in X or RAM, and (d) Computed odd contribution in X for simulated first harmonic signal.

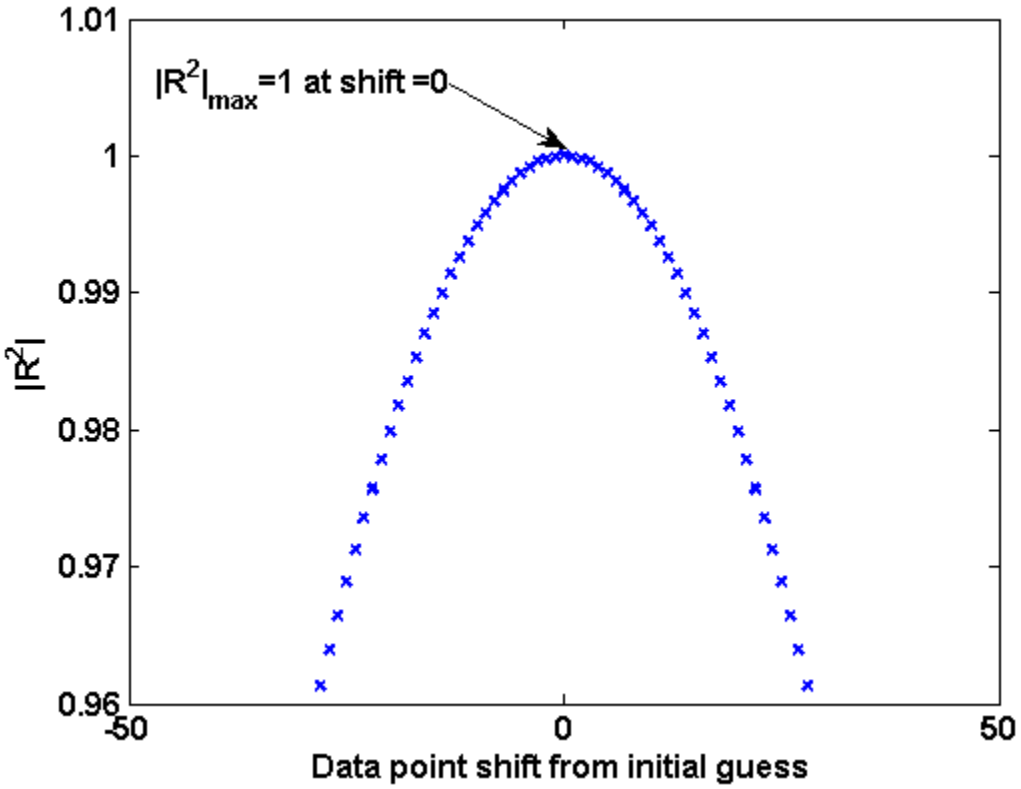

Figure 4.5. R-squared value vs. shift in data points for simulated first harmonic.

4.4.2 RAM normalization for absolute line shape function

From Eq. (4.2), X-component of second harmonic signal consists of only $\alpha'(\nu)$ and $\alpha''(\nu)$ terms which are odd and even symmetric respectively. Therefore, following the algorithm in Figure 4.3, it is easy to split RAM and FM/AM contributions. Otherwise the symmetry axis located in the recovery of first harmonic RAM can also be used to recover second harmonic RAM, if both harmonics were measured concurrently. After RAM contributions from the first and second harmonic signals are available, first derivative of absolute absorption line shape function, i.e. $\alpha'(\bar{\nu})Cl$ can be computed using Eq. (4.3).

$$\begin{aligned} RAM_{\text{2f, Normalized}} &= \frac{RAM_{\text{2f}}}{RAM_{\text{1f}}} \\ &= -\frac{\Delta I \bullet \alpha'(\bar{\nu})Cl \bullet \delta\nu \bullet \cos(\psi)}{2\Delta I\left[1-\alpha(\bar{\nu})Cl\right]} \approx -\frac{\alpha'(\bar{\nu})Cl \bullet \delta\nu \bullet \cos(\psi)}{2} \end{aligned} \tag{4.3}$$

$\delta\nu$ and ψ remain fixed after the laser diode operating conditions are decided. Consequently, the WMS system is now calibration free with no dependency on laser intensity change over time.

4.5 Experimental Validation: Simultaneous Measurement of Concentration and Pressure

4.5.1 Designed components for experiment

4.5.1.1 Gas sensing cell (sensor-probe)

The gas cell or sensor probe is an open cavity for light and gas interaction. It uses two collimators on both ends for guiding light without significant power loss. In order to minimize the interference between the two surfaces of a protection window, two wedge angle windows are also used in the design. The interference between the window and other optical components were removed by tilting the windows with 10 degree. This is shown in Figure 4.6.

Figure 4.6. Tilted window and collimators in sensor probe.

The cross-section view of the sensor probe is shown in Figure 4.7. It has two stage dust filters for protection from dust and other debris in underground mines.

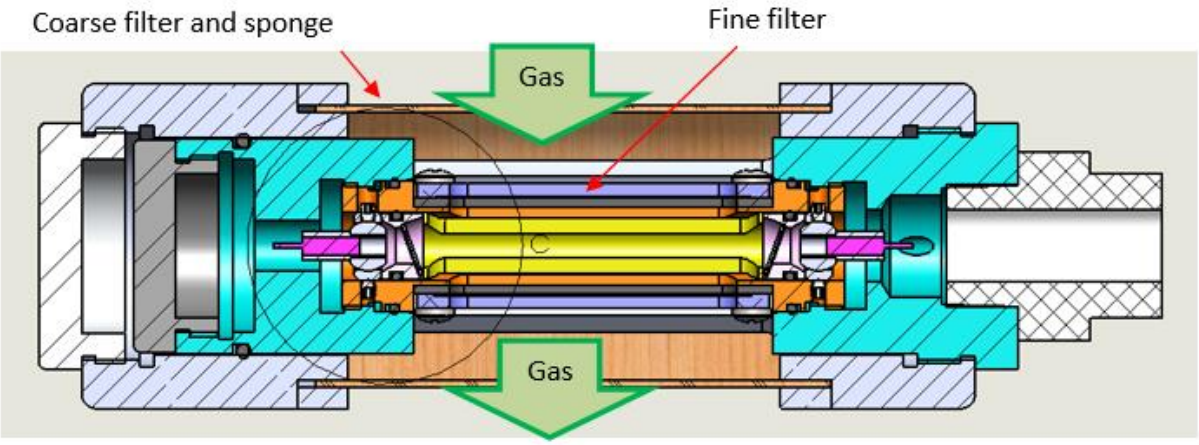

Figure 4.7. Sensor probe with dust filters in place [57].

The gas can flow from top coarse filter to the bottom coarse filter. The coarse filter can block most of the big size particles and the fine filter would block fine particles larger than 40µm. The window for the coarse filter is large to increase the response time. Figure 4.8 shows the fabricated sensor probe along with the dust filters and optical fiber connections from the collimators.

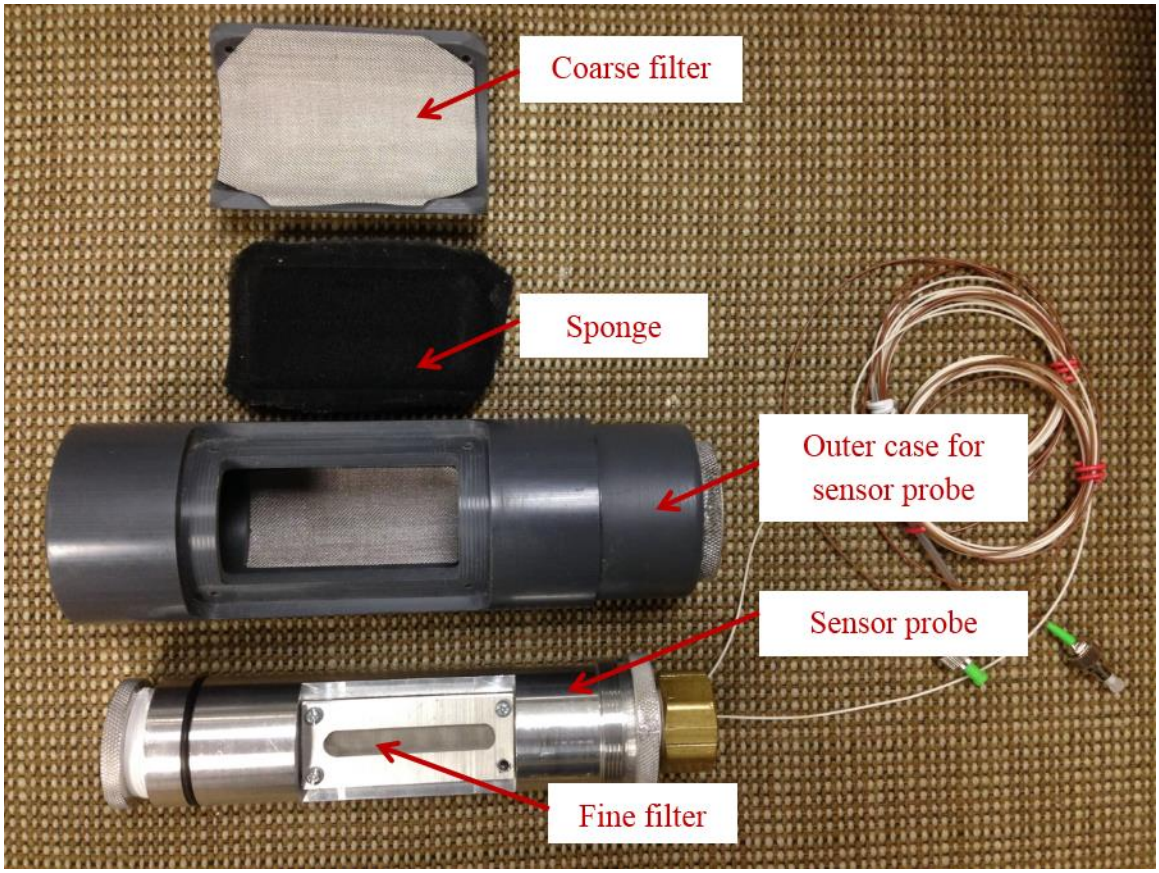

Figure 4.8. Fabricated sensor probe (disassembled).

4.5.1.2 Laser driver circuit

Laser controller circuit includes TEC driver (HTC1500, Wavelength Electronics Inc.) and current driver (PLD200, Wavelength Electronics Inc.) whose exemplary control circuits can be obtained from vendor website.

4.5.1.3 Photo-receiver circuit

Each optical receiver module contains Trans-impedance amplifier (TIA) with adjustable bias and gain, and analog filter. Figure 4.9 shows the circuit design used to achieve these steps. The photodetector is operated in photo-voltaic mode to eliminate the possibility of dark current [58]. V_{BIAS} pin is used to offset the mean of photo-diode current generated from average laser intensity. This is necessary because average laser power carries no information about gas absorption and unnecessarily limits the amplifier gain. The gain of the TIA is determined by feedback resistor R_F which can be switched by solid-state relay

switches. This helps in measuring gas absorption signals that is changing exponentially (Refer Eq. (2.10)) with concentration. The bandwidth of the TIA is controlled by both R_F and C_F. The exact values for various circuit elements in the TIA are selected by following some excellent literature available on this topic [59–62]. Finally, a 3rd order analog filter is placed between the TIA and output port to remove additional high frequency noises.

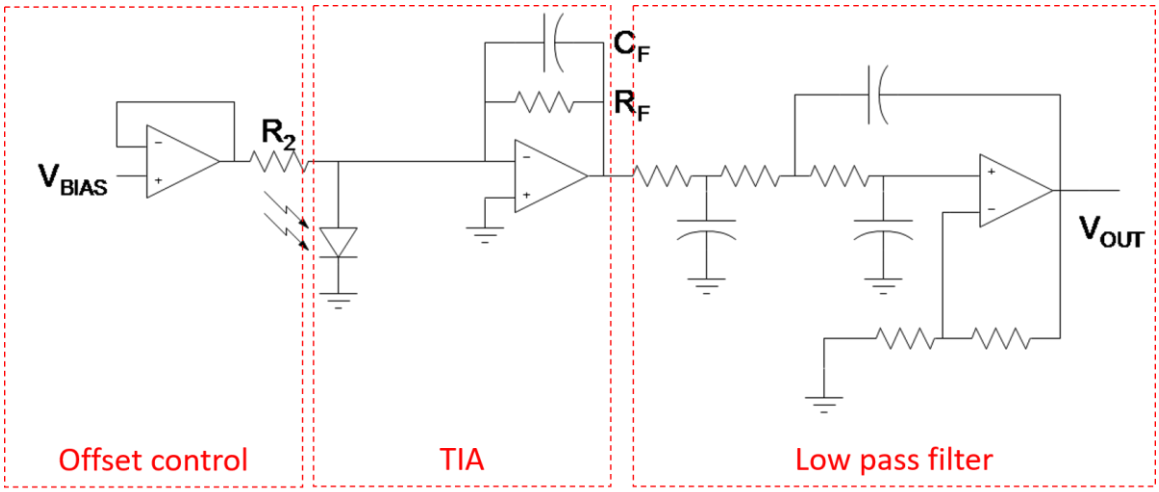

Figure 4.9. Photo-detection and trans-impedance amplifier (photodiode in photovoltaic mode).

4.5.2 RAM recovery for first harmonic using symmetry

The experiment setup for measuring gas concentration and pressure using WMS scheme is described in Figure 4.10. In order to validate the proposed RAM signal recovery method, first harmonic signals from CH_4 absorption are measured for two different methane-air mixtures at approximately 1% and 8% concentration levels with a 5.5 cm long open gas cell. At a concentration of 8%, estimated optical depth is about 0.17 and thus assumption for linear approximation in Eq. (2.10), i.e. $\alpha Cl \le 0.05$, is not valid. However, since the maximum percentage error in this exponential to linear approximation is only 1.6% and $e^{-\alpha(\nu)Cl}$ is symmetric about the same $\nu = \nu_0$ axis as $\alpha(\nu)$, the proposed approach works reasonably well. But we must emphasize that it is better to keep optical depth smaller than 0.05 and for high concentration measurements, light-gas interaction length l can be reduced to avoid exceeding this limit.

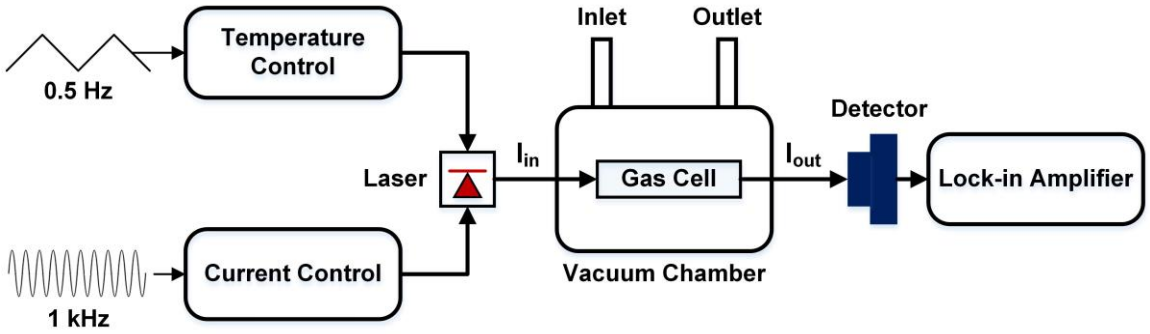

Figure 4.10. Experiment setup for harmonic signal measurement.

As show in Figure 4.10, the gas cell is kept inside an enclosed quartz vacuum chamber where pressure could be varied with a rotary vane pump and the temperature in the chamber remained constant at room temperature. After the lock-in amplifier (Stanford Research Systems, Model SR810) outputs are sampled (rate=10k) by an A/D card (NI, Model USB 6211), RAM signal is recovered using the algorithm presented in Figure 4.3. The R-squared plot for measured harmonic signal at 97 kPa from 8% methane-air mixture is shown in Figure 4.11. Due to nonlinear laser intensity response and other background signals in Y, maximum correlation was reached at data point shift=4, not zero. The measured X, Y component as well as the even and odd contributions recovered from correct axis split of X-component for 1% and 8% methane-air mixtures have been depicted in Figure 4.12 (a) and (b) respectively. It is clear that symmetry approach works well in recovering RAM and FM/AM components at both concentrations.

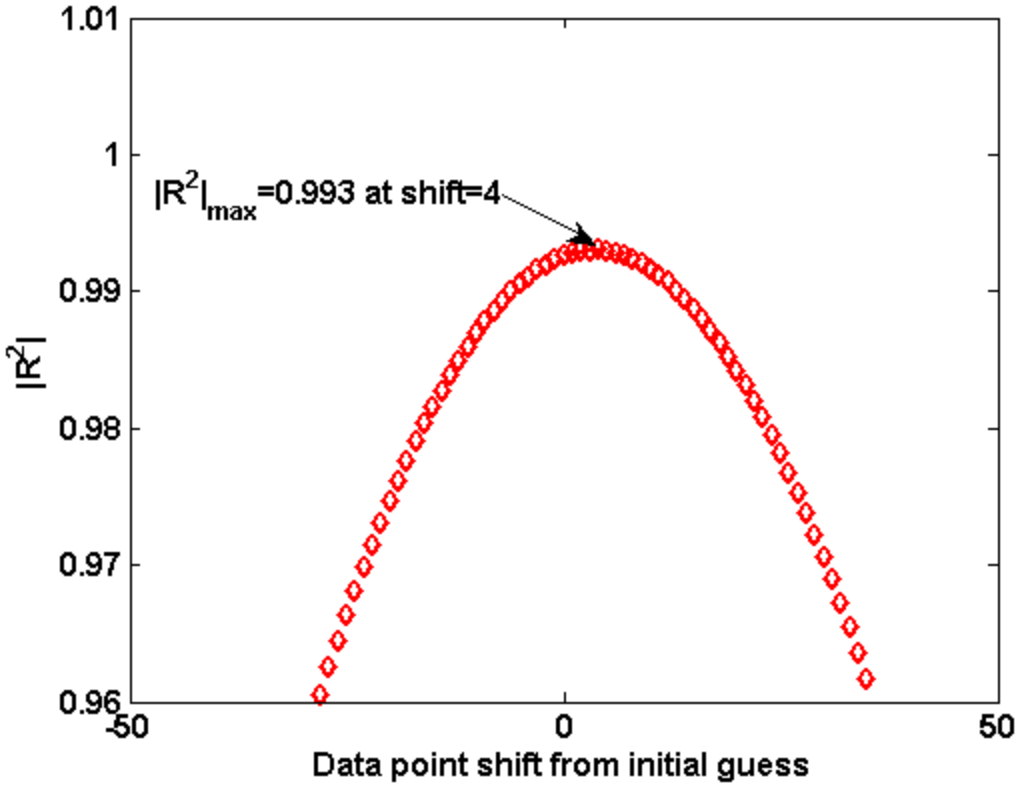

Figure 4.11. R-squared value vs. shift in data points for experimentally measured first harmonic.

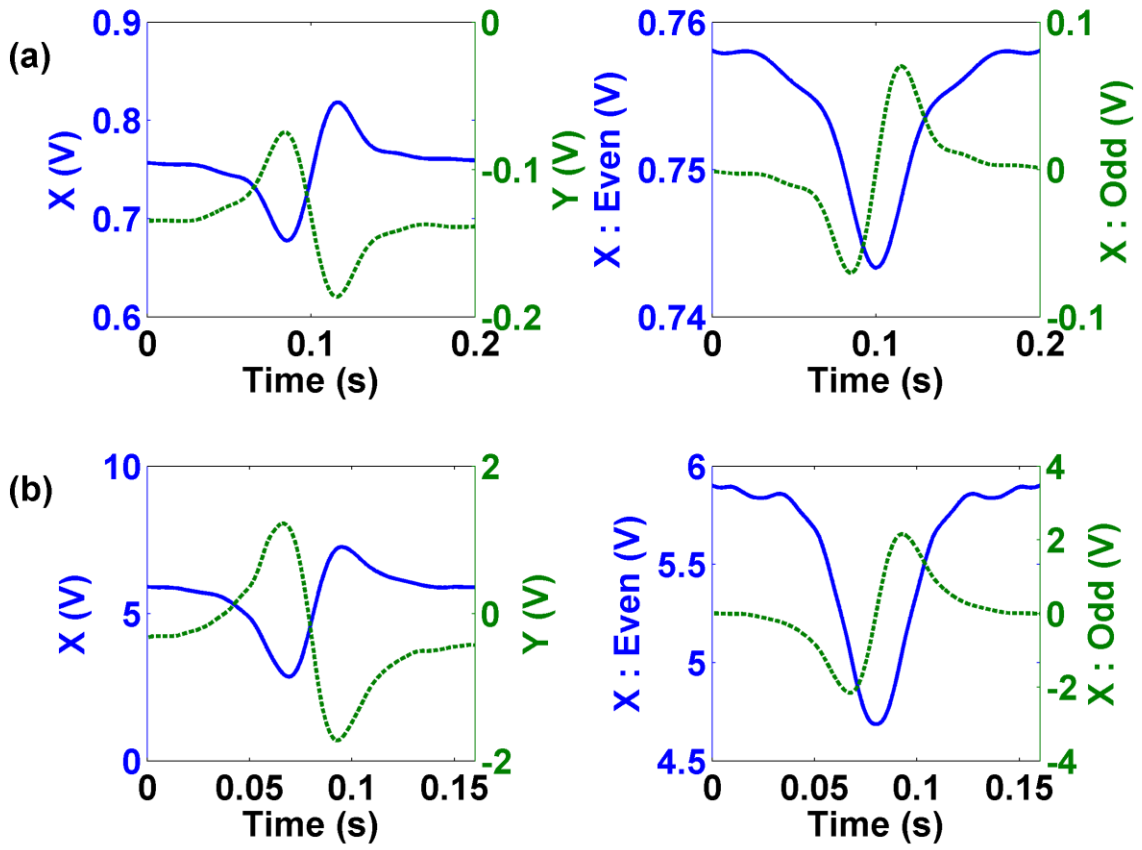

Figure 4.12. (a) X and Y-component (left), extracted even and odd contributions in X (right) for measured first harmonic signal at 1% methane concentration, (b) X and Y-component (left), extracted even and odd contributions in X (right) for measured first harmonic signal at 8% methane concentration.

The above harmonic measurement process is repeated at different chamber pressures for 8% methane-air mixture and the estimated FWHM value from RAM is plotted against the reading from a digital pressure gauge (MTI Corp., Model EQ-DVPG-LD). As FWHM value for a collision broadening dominated absorption profile is directly proportional to gas pressure (see Eq. (2.8) for explanation), a linear relation between the two measured parameters is expected. However, the chamber we used for the experiment allowed only negative atmospheric pressure (less than 100 kPa), where contributions from Doppler broadening could not be ignored. Therefore, expected values of absorption FWHMs are first calculated using Eq. (2.6), (2.8), and HITRAN data for pressures 0 - 100 kPa. Figure 4.13 shows expected FWHM obtained from a Voigt profile approximation of absorption profile $\alpha(\nu)$ [45]. It is evident that overall FWHM has a strict linear relation with pressure in the range 60 to 100 kPa. Note that the FM amplitude $\delta\nu$ is set to be 0.0074

cm^{-1} in the experiment such that modulation index *m* remained less than 0.2 over this pressure range.

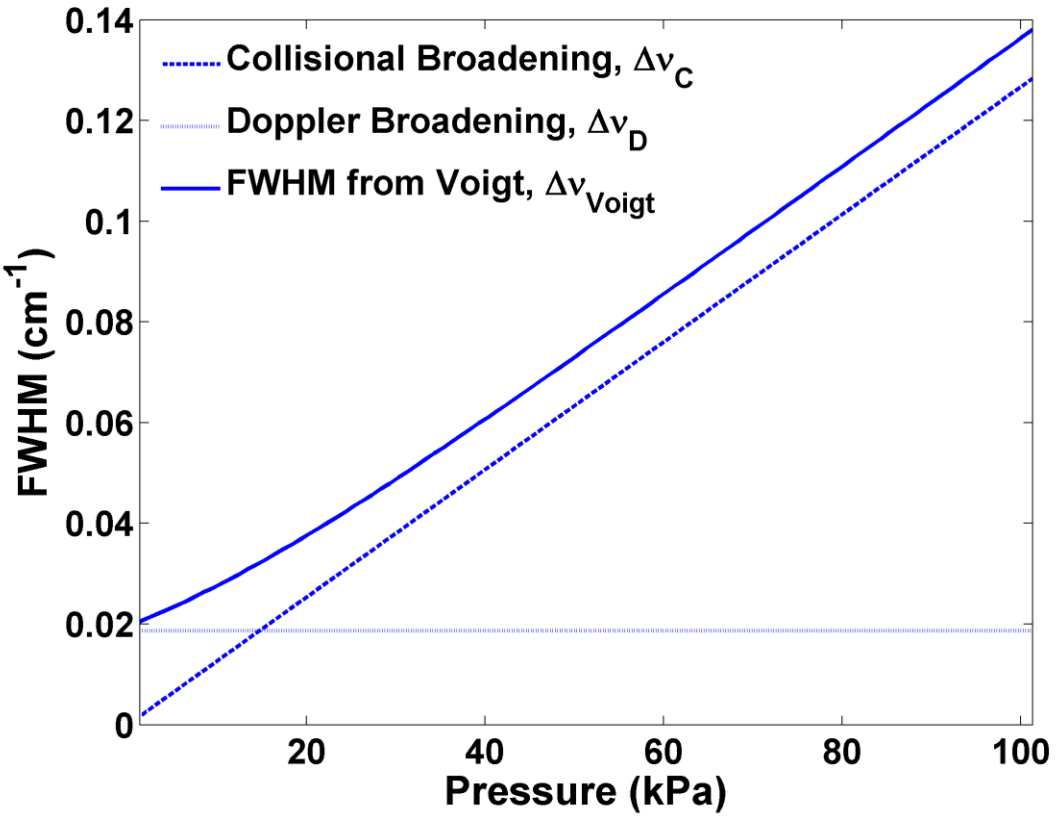

Figure 4.13. Calculated FWHM vs. pressure at 296 K using HITRAN data.

The FWHM and optical depth estimated from recovered first harmonic RAM signals are plotted against measured pressure in Figure 4.14 (a) and (b) respectively. Each measurement point for these plots is obtained from an average of ten consecutive absorption scans. From the linear relation between experimentally measured FWHM and pressure, it is evident that recovered RAM_{1f} is pretty accurate. Error bars have also been indicated in the same plots. The accuracy of gas pressure estimation by this approach estimated to be ±0.73 kPa in the range 60 to 100 kPa. It should be noted that FWHM values have been indicated in seconds as they are calculated from harmonic signals measured in time domain. Figure 4.14 (b) indicates the optical depth (αCl_{max}) estimated from these recovered first harmonic RAM signals. Expected optical depth from HITRAN

data simulation is also depicted in the same plot for comparison. It is apparent that optical depth estimated from RAM_{1f} deviates from HITRAN simulation in low pressure range. We believe that methane, being a lighter gas compared to air, escapes faster during vacuuming process and thus reducing αCl value. To verify this phenomenon, optical depth measured from direct absorption signal at the photo-detector has been shown in the same plot. As directly measured optical depth closely follows that obtained from RAM_{1f}, the accuracy of symmetry approach is proved.

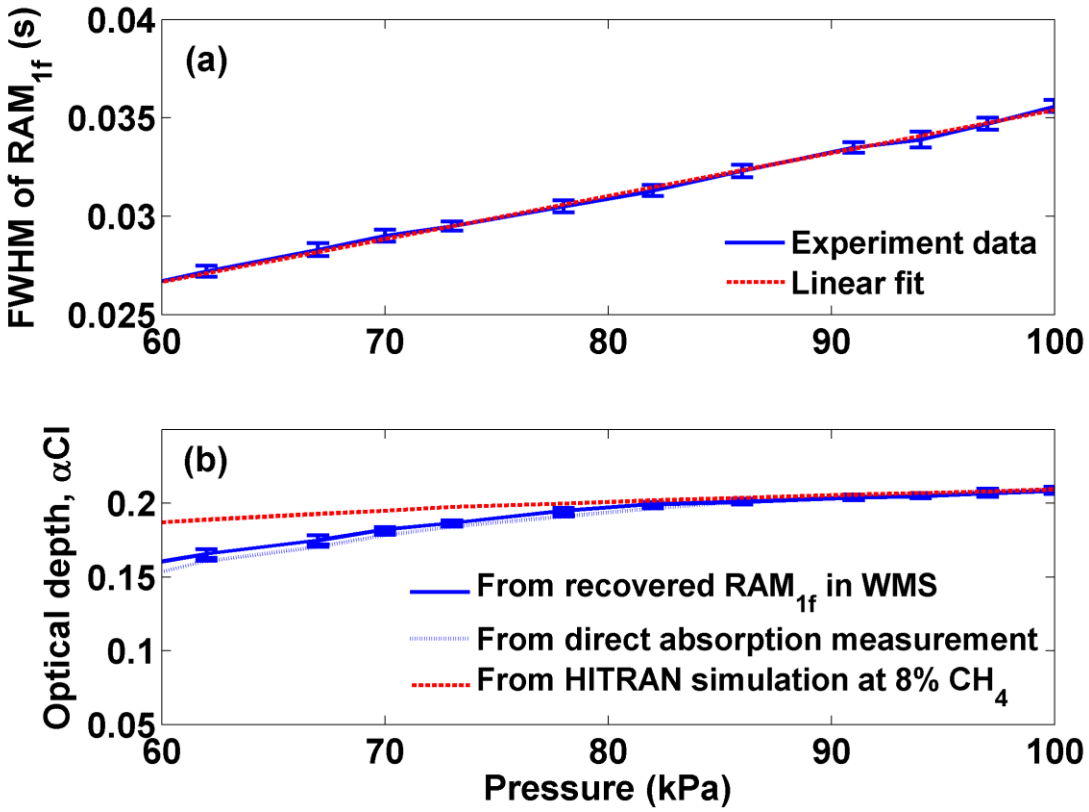

Figure 4.14. (a) FWHM of gas absorption profile, and (b) Estimated optical depth from RAM component in measured first harmonic signals vs. gas pressure at 8% methane concentration (error bars are evaluated from ten consecutive scans).

4.5.3 Calibration free measurement by RAM normalization

In order to validate the *RAM normalization* method proposed in Section 4.4.2, harmonic signals from CH_4 absorption are measured for a 1% methane-air mixture at different

optical transmission loss values in the sensor probe. X, Y-components of first and second harmonics signals are calculated by a software lock-in amplifier (LabVIEW program) after sensor signal is digitized by the A/D card. Using the symmetry method of Figure 4.3, RAM_{1f} and RAM_{2f} have been recovered. Finally, $RAM_{2f,Normalized}$ is calculated according to Eq. (4.3).

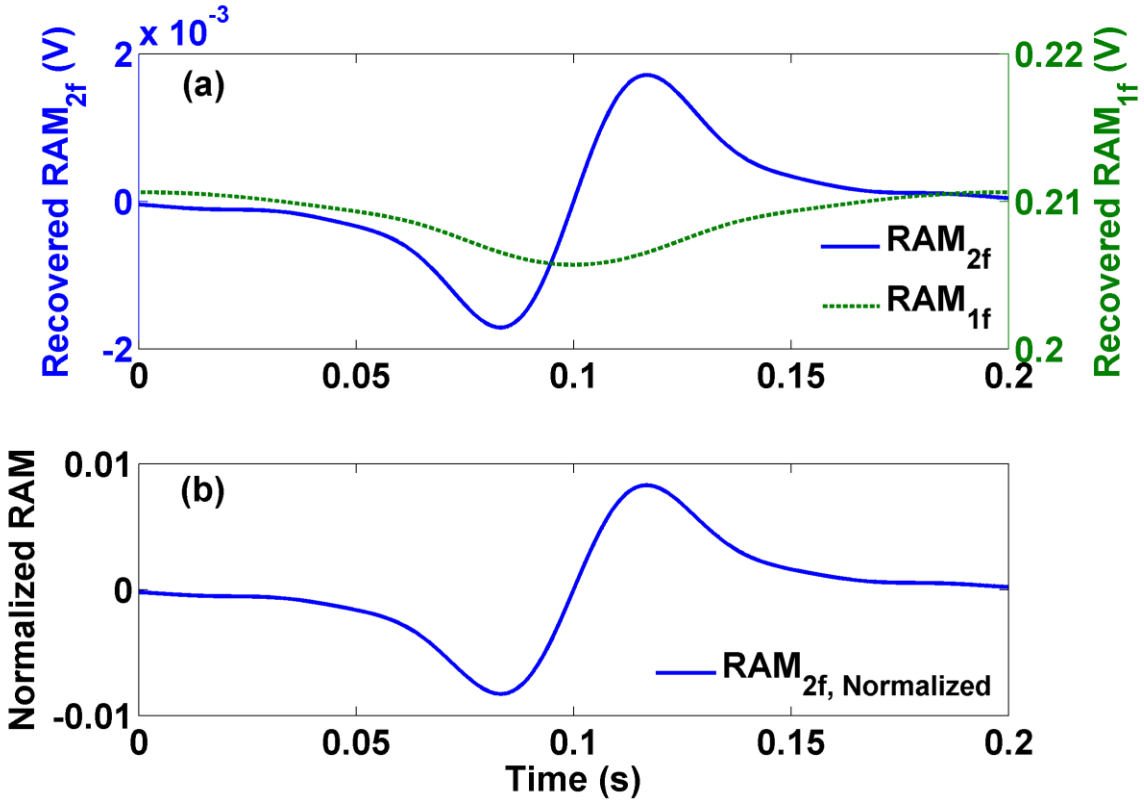

Figure 4.15. (a) Recovered RAM components from measured first and second harmonic signals, (b) Normalized second harmonic RAM.

Figure 4.15 (a) depicts the results from RAM recovery when optical transmission loss was approximately 16 dB. Also, it is obvious that $RAM_{2f,\ Normalized}$ signal in Figure 4.15 (b) has almost no distortion and is very close to ideal $\alpha'(\bar{\nu})$ shape. Therefore, its extrema locations can be used to calculate absorption FWHM, $\Delta\nu_C$ (See Figure 4.2), without any difficulty. The amplitude of $RAM_{2f,\ Normalized}$ and the optical depth estimated from it are

shown in Figure 4.16 (a) and (b) respectively when optical transmission loss changes by 12 dB. The amplitudes of corresponding first and second harmonic RAMs are also shown for comparison. Note that Figure 4.16 (a) only shows the AC amplitude for RAM_{1f} signal, i.e. DC or baseline has been subtracted for the plot. Although RAM_{1f} and RAM_{2f} are both changing with transmission loss, $RAM_{2f,\,Normalized}$ and its corresponding optical depth remain unchanged. This indicates that this new technique is independent of laser intensity parameters and thus suitable for realizing a calibration-free WMS system.

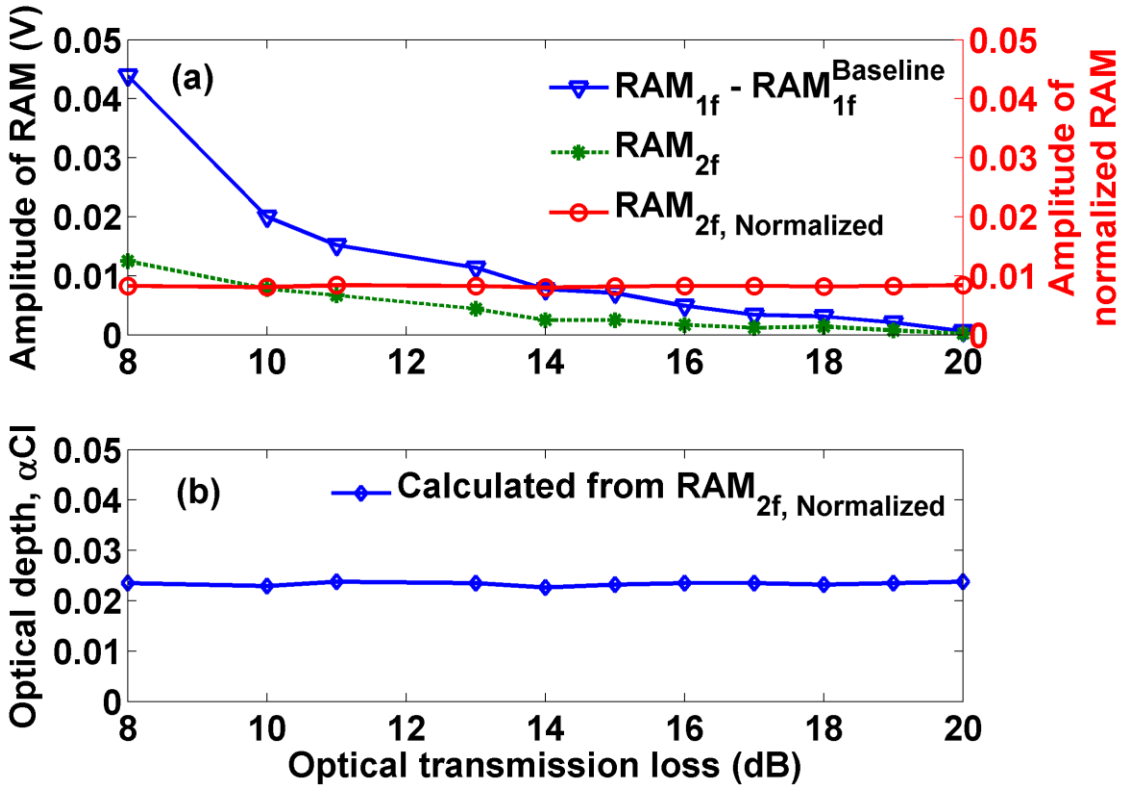

Figure 4.16. (a) Amplitudes of recovered first harmonic RAM, second harmonic RAM, and normalized second harmonic RAM, (b) Estimated optical depth from normalized second harmonic RAM with varying optical loss in the sensor probe.

4.5.4 System sensitivity and measurement range

The accuracy and sensitivity of gas sensor system is tested for methane (CH_4) monitoring by comparing its measured concentration value with a gas chromatograph (Shimadzu,

Model GC-2014) reading. A *partial pressure based mixing* and *dilution* technique was used for preparing different concentration mixtures[2]. Figure 4.17 depicts the true methane concentration plotted against the measured concentration by the sensor with error bars from ten measurements. It is evident that the sensor system tracks the true concentration accurately and has a linear relation with it. It can measure CH_4 concentration from 0.01% (i.e. 100 ppm) to 50% in real time and satisfies the lower explosive limit (LEL) criteria (5% concentration) on commercial methane sensors. The sensor accuracy estimated to be ±60 ppm or 1.6% of mean reading (whichever is greater).

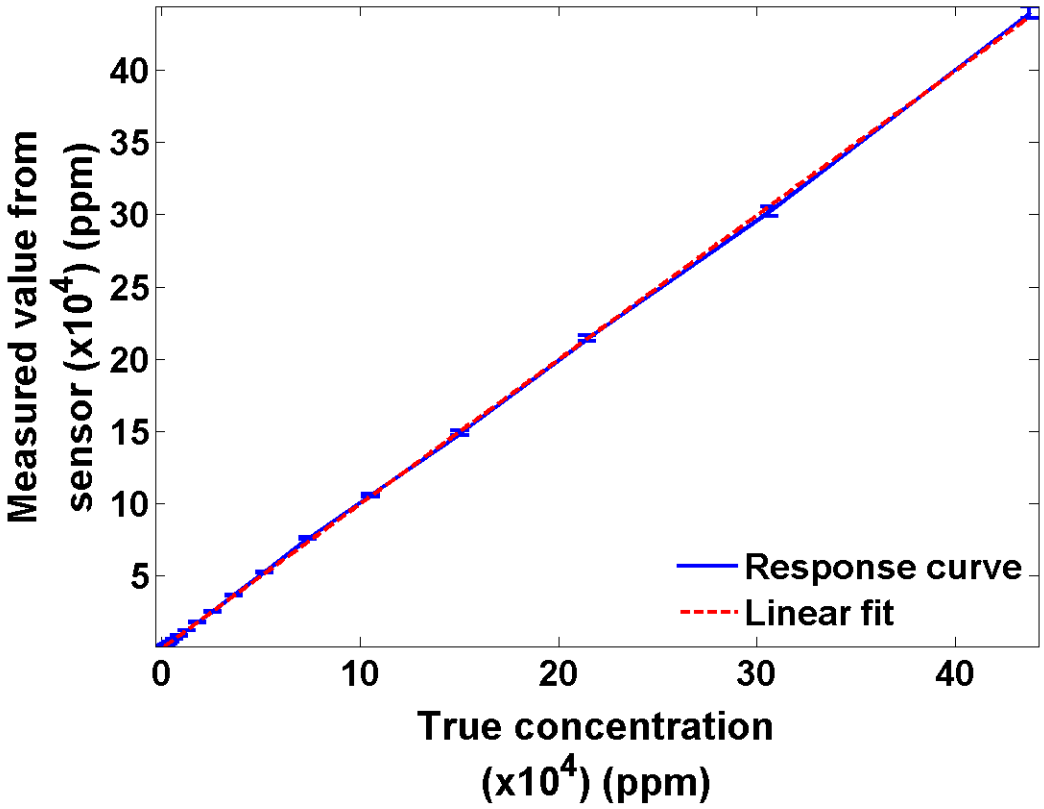

Figure 4.17. Performance of methane (CH_4) concentration measurement system for 100 ppm to 500,000 ppm (error bars are evaluated from ten consecutive sensor readings).

4.6 Advantages and Limitations

[2] A discussion on preparing different gas concentration mixtures using their partial pressure and dilution technique can be found in Appendix B.

4.6.1 Advantages

An alternative strategy to implement a calibration-free system without any modification to traditional WMS system design is presented. This new method exploits the symmetry present in harmonic signals to recover RAM contributions and estimate absolute line shape function. After absolute line shape has been determined, gas concentration or pressure can be calculated without any reference mixture. Furthermore, unlike the existing WMS techniques, the new approach does not require laser diode parameters such as average intensity, intensity modulation amplitude or modulation rate to be known in advance. It also avoids performing any extensive simulation of line shape function (using HITRAN database) to match the measurement. In addition to these benefits, RAM recovery based on symmetry and normalization technique also suppresses intensity fluctuations during measurement. Passing the digitized harmonic signals through low pass filter (cut off frequency must be higher than frequency bandwidth of absorption profile) removes any high frequency noise which can make symmetry axis determination erroneous. Although very low frequency perturbations can still pass through, mathematical correlation ensures an accurate estimation of symmetry axis (Note that accuracy of axis location is determined by the step size in which guessed locations are moved left/ right and hence sampling frequency used during digitization is kept sufficiently high). The impact of remaining low frequency perturbations in optical intensity and its influence on $RAM_{\text{2f, Normalized}}$ can be modeled as follows.

Since laser frequency $\bar{\nu}$ is linearly scanned by thermal or current tuning, $I(t)$ primarily shows a linear response in time with some mean value I_0. Therefore, $I(t)$ can be expressed as $I(t) = I_0 + \Delta I_{\text{Scan}}(t)$, where $\Delta I_{\text{Scan}}(t)$ is an odd function about symmetry axis. Also, for small modulation index, $\Delta I(t)$ remains nearly constant, i.e. $\Delta I(t) = \Delta I_0$. For a typical WMS system, the above equations are approximate representations of laser intensity change with time. Let us treat any deviation from these equations (such as any nonlinear response of laser for $I(t)$ or $\Delta I(t)$, or intensity variations in the gas measurement cell due to mechanical disturbance) as noise. Now, the laser intensity response can be expressed by Eq. (4.4).

$$\begin{aligned} I(t) &= I_0 + \Delta I_{\text{Scan}}(t) + N_1(t) \\ \Delta I(t) &= \Delta I_0 + N_2(t) \end{aligned} \tag{4.4}$$

where $N_1(t)$ and $N_2(t)$ are time varying low frequency noises.

Since noise response is random in time, it should be treated as a sum of even and odd functions with respect to symmetry axis, i.e. $N_{1,2}(t) = N_{1,2}{}^{\text{Even}}(t) + N_{1,2}{}^{\text{Odd}}(t)$. From Eq. (4.1), (4.2) and with some algebra, it is easy to show that recovered RAM contributions from the X-components of first and second harmonic will be expressed by Eq. (4.5) and (4.6) respectively.

$$RAM_{1\text{f}} = -\frac{1}{2}\begin{Bmatrix} \Delta I_0\left[\alpha(t)Cl - 1\right] \\ +N_2{}^{\text{Even}}(t)\left[\alpha(t)Cl - 1\right] \\ +\Delta I_{\text{Scan}}(t) \bullet \alpha'(t)Cl \bullet \delta\nu \bullet \cos(\psi) \\ +N_1{}^{\text{Odd}}(t) \bullet \alpha'(t)Cl \bullet \delta\nu \bullet \cos(\psi) \end{Bmatrix} \tag{4.5}$$

$$RAM_{2\text{f}} = -\frac{1}{4}\begin{Bmatrix} \Delta I_0 \bullet \alpha'(t)Cl \bullet \delta\nu \bullet \cos(\psi) \\ +N_2{}^{\text{Even}}(t) \bullet \alpha'(t)Cl \bullet \delta\nu \bullet \cos(\psi) \\ +\Delta I_{\text{Scan}}(t) \bullet \alpha''(t)Cl \bullet \dfrac{\delta\nu^2}{2} \bullet \cos(2\psi) \\ +N_1{}^{\text{Odd}}(t) \bullet \alpha''(t)Cl \bullet \dfrac{\delta\nu^2}{2} \bullet \cos(2\psi) \end{Bmatrix} \tag{4.6}$$

It is apparent that recovered RAM signals from first and second harmonics are affected by the same sets of odd or even noise signals ($N_1{}^{\text{Odd}}$ and $N_2{}^{\text{Even}}$). Therefore, normalization of second harmonic RAM by first harmonic RAM helps in reducing the influence of laser intensity fluctuations. Furthermore, $|\alpha(\bar{\nu})Cl - 1| >> \alpha'(\bar{\nu})Cl\delta\nu >> \alpha''(\bar{\nu})Cl\dfrac{\delta\nu^2}{2}$ (see Figure 4.2). So if we neglect the last two terms in Eq. (4.5) and (4.6), and estimate $RAM_{2\text{f, Normalized}}$, it is identical to that derived in Eq. (4.3).

4.6.2 Limitations

For RAM recovery from even-odd splitting of harmonic signal to correctly work, absorption profile, $\alpha(\nu)$ needs to be symmetric in shape. As discussed earlier, gas pressure (P), temperature (T), and strength (S) of the absorption line transition being interrogated determine the shape of $\alpha(\nu)$. If the target line transition is completely isolated from the influence of nearby line transitions or the neighboring transition lines are spectrally equidistant from target line transition, $\alpha(\nu)$ will be symmetric in shape. In the near infrared region, i.e. 1560 - 1580 nm, carbon dioxide (CO_2) and carbon monoxide (CO) have over twenty such line transitions available [32]. Also for methane (CH_4), three well isolated lines are available in 1647 – 1655 nm range. But unlike CO and CO_2 absorption lines, CH_4 lines are blended by closely packed secondary peaks. For example, the primary transition line at 1650.961 nm has three secondary peaks at 1650.958 nm, 1650.955 nm, and 1650.948 nm respectively [32]. This is graphically shown in Figure 4.18 (a). Nevertheless, the absorption profile simulated at 100 kPa pressure and 296 K temperature using Eq. (2.2) and (2.7) shows excellent symmetry. This symmetric shape is also verified by a Lorentz curve fit of overall absorption profile in Figure 4.18 (b) and (c). Note that, broadened profiles from all four line transitions contributing to this overall absorption profile are also indicated by blue dashed lines in the same figure.

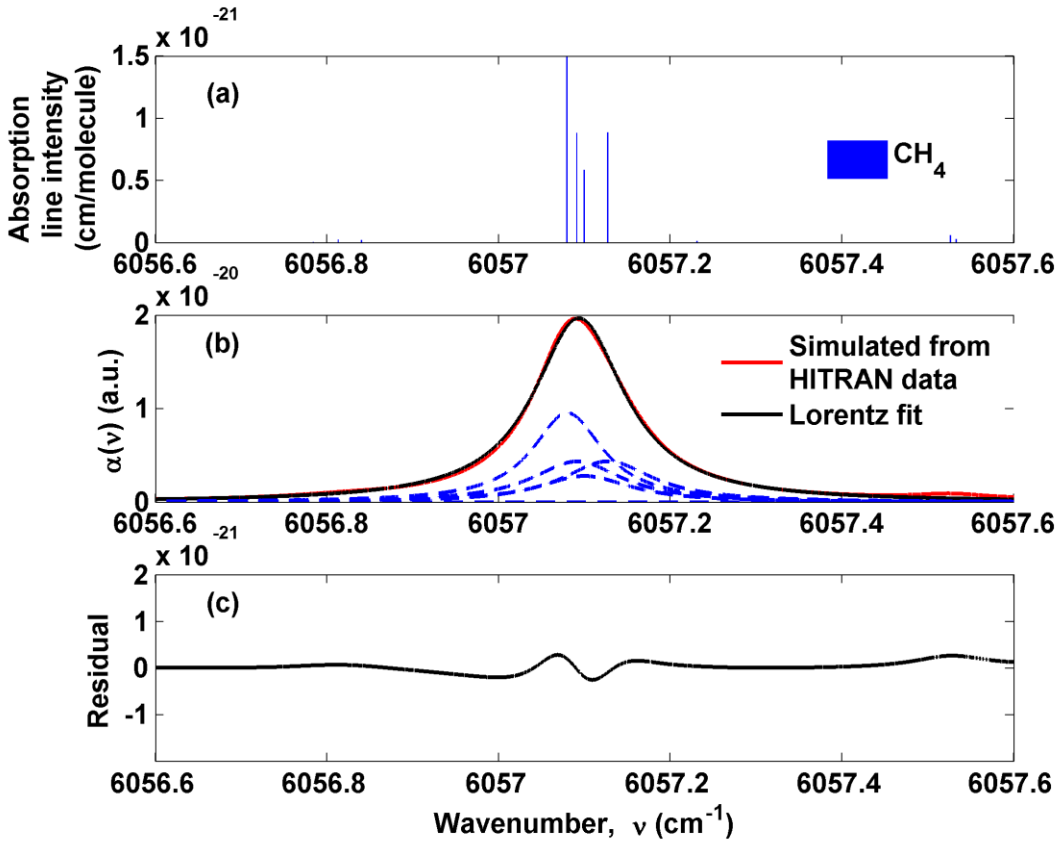

Figure 4.18. (a) Methane absorption line transitions near 1651 nm, (b) Methane absorption profile simulated at 100 kPa and 296 K using HITRAN data with Lorentz fit to verify its symmetry, (c) Residuals for the fit (difference between corresponding data points).

It is also important to remember that shape of $\alpha(\nu)$ is decided by gas pressure and temperature. For closely packed line transitions of CO and CO_2, pressure broadened neighboring transition lines will distort the target transition line. Therefore, symmetry of $\alpha(\nu)$ should be verified for pressures exceeding 200 kPa. But for blended transition lines of CH_4, the line shape functions of the four transitions are fairly narrow at pressures below 60 kPa. Thus their individual contributions make the overall absorption profile asymmetric at pressures below this value. However, CH_4 absorption profile remains fairly symmetric in low to moderate pressure range, i.e. 60 kPa to 1000 kPa, as confirmed by Figure 4.18 (b). However, if symmetry approach is applied to an absorption profile near or slightly above the recommended pressure and temperature range, the recovered RAM components from both first and second harmonic will be partially incorrect. Also, RAM recovered from first harmonic will be less affected by the asymmetry as compared to that

recovered from second harmonic since the former has a large background RAM associated with it.

Another limitation on the proposed method for calibration-free WMS system is the restriction on modulation index ($m \leq 0.2$). But this can be overcome if higher order derivatives are to be considered to generate correction factors for recovered RAM [24]. Alternatively, Fourier series expansion model for WMS system can be used to devise a strategy similar to the proposed one for separating RAM component from first and higher harmonic signals by exploiting the symmetry in absorption profile [14,16,63].

Chapter 5 Strategy for Calibration-free Spatially Distributed Gas Detection using Diode Lasers

5.1 Motivation

An increasing number of gas pipelines are being constructed in remote regions affected by harsh environmental conditions. In the absence of regular monitoring, geohazards or third party interference often result in pipeline failures leading to large leaks or even explosions. Consequently, there is a growing demand for a system that is capable of detecting and monitoring such hydrocarbon leakage along the pipeline. In Section 2.3, we discussed about the limitations of current technology and how they are difficult to implement in practical applications. Moreover, unlike single point gas monitoring system, existing distributed gas sensing methods cannot measure the full absorption response spectrum $\alpha(\nu)$. As explained in earlier chapters, full absorption response can be used to make the gas sensing system calibration-free and estimate gas parameters like pressure and temperature in addition to concentration. In this chapter, a new method for spectroscopic measurements is discussed which can address the aforementioned issues and can also be applied for distributed sensing.

5.2 Frequency Chirped Diode Laser for Spectroscopic Measurement

A diode laser's peak emission frequency is determined primarily by the energy band gap of the semiconductor material and then by the junction's temperature and current density [64]. The laser emission frequency tunes with temperature because both the optical path length of the cavity and the wavelength dependence of the gain curve change with temperature. In general, an increase in temperature also increases the laser cavity length which results in a decrease in emission frequency. But the exact temperature dependence of the laser characteristics varies substantially for different models and types of lasers. In addition to dependence on temperature, the laser emission frequency also depends on the injection current. Changes in the injection current can affect the diode in two ways: (1) change the junction temperature for the diode because of Joule heating, (2)

change the carrier density which also changes the index of refraction of lasing medium. Both these effects will result in a transient variation in laser emission frequency which is referred to as *frequency chirp* [65–69].

For time scales longer than about 1 μs the current tuning can simply be thought of as a way to change the temperature rapidly, because the carrier density contribution to the index of refraction tuning is relatively small [64,68]. So when a step-function pulse is applied as injection current, Joule heating will decrease the laser emission frequency with time. The opposite behavior will be observed when laser driving current is reduced rapidly. So the output electric field from a modulated semiconductor diode laser can be expressed as Eq. (5.1).

$$E_1(t) = E_0(t)\exp[j\omega_0 t + j\phi(t)] \tag{5.1}$$

Here $E_0(t)$ is the modulated amplitude, ω_0 is the initial laser emission frequency, and $\phi(t)$ is the modulated optical phase. The modulated laser emission frequency can be written as

$$\omega(t) = \omega_0 + \frac{d\phi(t)}{dt} \tag{5.2}$$

For a step-function pulse modulation as the injection current, the amplitude or intensity modulation of the diode laser field is also approximately a step-function if the transition time of the modulation pulse is smaller than the relaxation time of the diode laser. But the emission frequency $\omega(t)$ responds in two steps: (1) frequency switching (ω jumps from continuous mode frequency ω_0 to ω_1 at the time t_0 when the pulse is applied); (2) dynamic frequency shift or chirp (ω rapidly change from ω_1 to ω_2 which is a new steady state value [70]. This behavior is depicted in Figure 5.1.

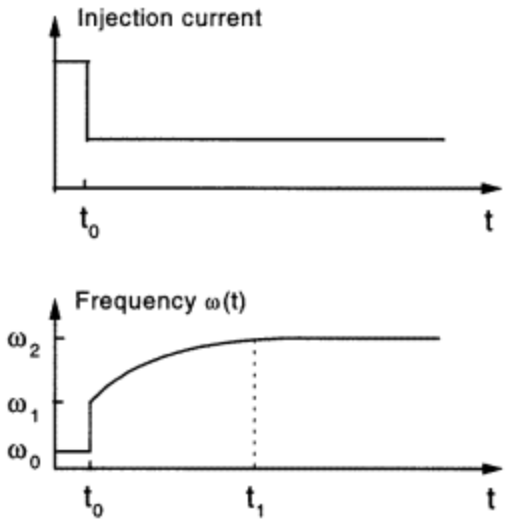

Figure 5.1. When the injection current is modulated by a step-function pulse from high to low, the diode laser emission frequency is first switched from its initial value ω_0 to ω_1 and then quickly shifted to ω_2 within the time duration of $t_1 - t_0$ [70].

However, for modulation time scales shorter than 100 ns, the temperature rise from Joule heating is small enough such that the carrier density effect is the dominant contributor to frequency chirp [64,68]. It is well know that in diode lasers, the refractive index changes with the carrier density [71–73]. When the carrier density varies, due to pump current variation or due to the stimulated emission depleting the carrier density, the refractive index change will affect the effective guide mode index and cause a spectral shift. For small-signal sinusoidal modulation (with a DC bias above threshold), the electron or carrier density both increases and decreases with the modulation. Hence the observed frequency chirping is bidirectional. However, if a short (several nanosecond or smaller duration) square pulse is applied as injection current, the optical pulse is generated only during the time in which the electron density is decreased by the process of stimulated emission. This is because of the nature of relaxation oscillation in optical pulse generation under fast and deep modulation. In this case, the reduced carrier density results in an increased refractive index in the active region. The result is an increase in optical path length for the laser cavity and emission frequency shifts to a smaller value. Consequently, under pulse modulation, there is no oscillation of frequency chirping as in the case of sinusoidal modulation; instead, the frequency chirping is unidirectional and monotonically decreases as a function of time during the optical pulse [65]. Regardless

of the frequency chirp mechanism, there are two classifications for this transient behavior exhibited by semiconductor diode lasers: (1) Frequency up-chirp or blue shift, (2) Frequency down-chirp or red shift.

Since laser frequency or wavelength chirp is a transient response, it can be used to rapidly scan an optical resonance in wavelength domain. Absorption response $\alpha(\nu)$ of gases like methane (CH_4), carbon dioxide (CO_2), carbon monoxide (CO), acetylene (C_2H_2) typically follow a Lorentzian or Voigt profile in optical frequency domain ν. At atmospheric pressure and room temperature conditions, the Full-Width-Half-Maximum (FWHM) width for these absorption curves lie in the range 4 ~ 7 GHz (e.g. 4.17 GHz for CH_4 absorption at 1650.96 nm, 3.78 GHz for CO absorption at 1563.09 nm, 6.98 GHz for CO_2 absorption at 1577.36 nm [55]). As this narrow range can be scanned by diode laser frequency chirp, spectroscopic detection of such gases is possible without any current or temperature tuning of wavelength applied to the laser like TDLS systems. This makes the new *frequency chirped diode laser spectroscopy* (FC-DLS) orders of magnitude faster than existing approach. Moreover, if diode lasers in the near Infrared (IR) region are used for frequency chirping and the injection current pulse duration is small enough, it is possible to realize a spatially distributed gas detection system along a single mode optical fiber.

Figure 5.2 shows the contrast between conventional wavelength scanning principles used for diode laser spectroscopy and the new frequency chirp based scanning. Here λ_0 is the wavelength at which gas absorption response peak appears. Although wavelength scanning is not linear during the chirp, the detection process can be ultrafast. Typical speed for conventional continuous wave (CW) wavelength scanning is few seconds to tens of millisecond. On the other hand, pulsed diode laser baser wavelength chirp scanning can be several millisecond (thermal chirp) to several nanosecond (carrier density variation).

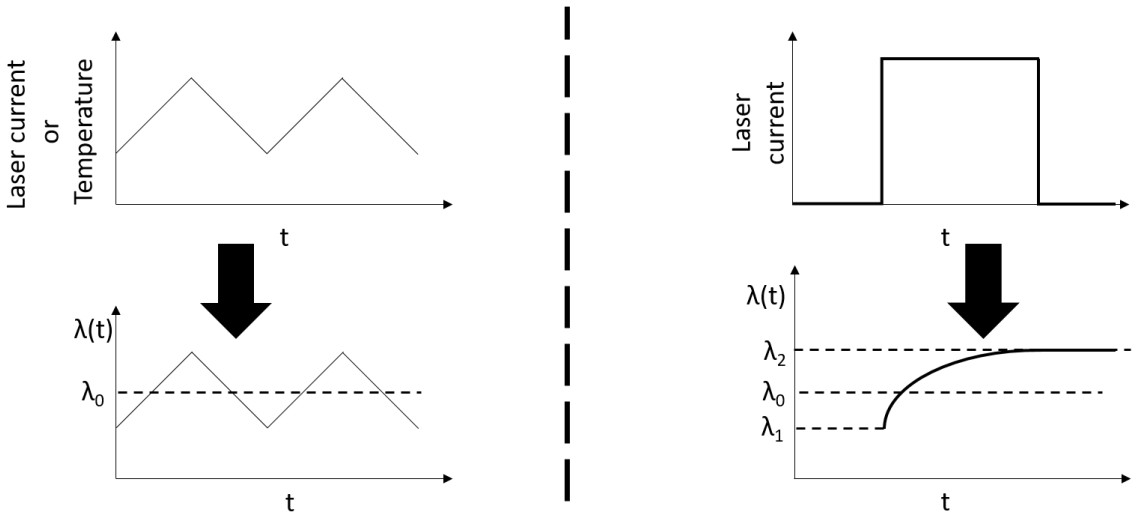

Figure 5.2. Conventional wavelength scanning for TDLS system using continuous wave (left) vs. injection current pulse generated wavelength chirp based scanning for FC-DLS system (right).

Now, a few important conditions should be satisfied for making laser frequency chirp spectroscopy work. Firstly, the maximum value of short current pulses fed to the laser diode should be sufficiently above the threshold (typically 80 mA or more for commercial DFB lasers used in telecommunication). This ensures that frequency chirp interval is wide enough to capture full absorption response spectrum $\alpha(\nu)$. Secondly, the temperature and DC bias current (if not zero) conditions of the laser should be reasonably stable so that its mean emission frequency does not drift with time and frequency chirp interval covers the target gas absorption line. Thirdly, measured absorption response at the photodetector will be distorted in time as frequency chirp is a nonlinear scanning process. So, if absolute laser line shape function is desired for additional information such as gas pressure or temperature along with its concentration value, this temporal distortion needs to be corrected. Therefore, laser emission frequency of wavelength must be recorded in real time during the measurement. The following section discusses how to obtain frequency chirp from telecomm lasers and track their emission wavelength chirp in time.

5.3 Laser Emission Wavelength Tracking

For recovering correct absorption line shape function $\alpha(\nu)$ from FC-DLS, it is important that to track laser wavelength or frequency variation in real time so that distortions dues to nonlinear $\nu(t)$ can be removed in data processing. This wavelength tracking can be accomplished by an interferometer with small Free Spectral Range (FSR). A single mode fiber Michelson interferometer with Faraday mirrors was used for this purpose as it can easily be connected to fiber pigtailed diode lasers and does not suffer from polarization fading exhibited by fiber interferometers. The interferometer used in the experiment is depicted in Figure 5.3.

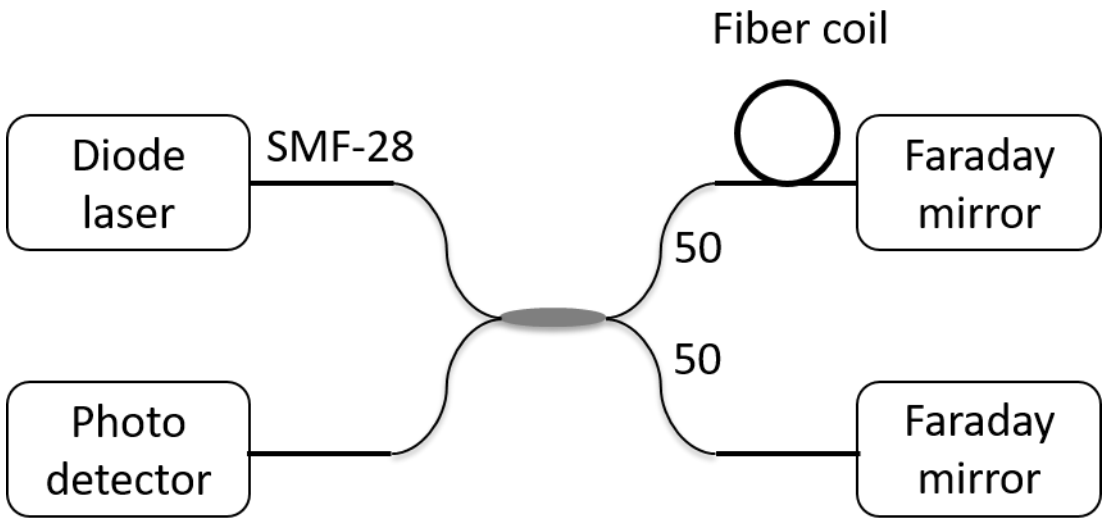

Figure 5.3. Michelson interferometer with Faraday Rotator Mirrors (FRM).

In this research, only positive injection current pulse of duration between millisecond to nanosecond is used. For a 1 ms pulse, diode laser exhibits frequency down chirp because of the thermal effect described in Section 5.2. In order to measure the frequency chirp generated from thermal effect for spectroscopy, a DFB laser diode from NEC Corporation (Model No. NX8570SD654Q-55) was used. The emission wavelength is near 1563 nm and suitable to capture carbon monoxide (CO) line transitions in the near Infrared. Figure 5.4 shows experiment setup for measuring wavelength chirp exhibited by DFB laser diode. The interferometer used in this setup has a free spectra range of 222 MHz or 1.81 pm near the wavelength of laser operation.

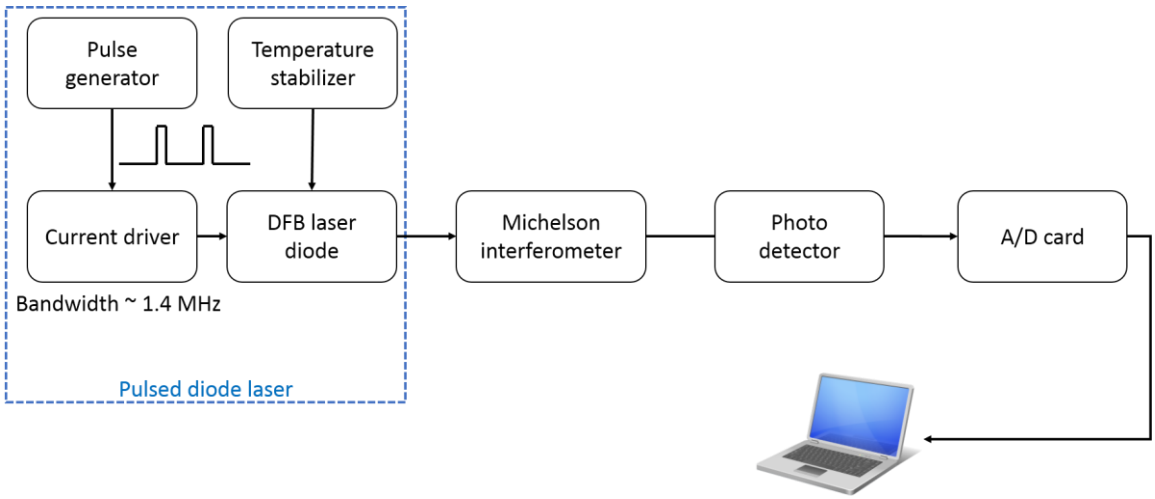

Figure 5.4. Measurement setup for diode laser chirp with 1 ms injection current pulse.

Figure 5.5 shows the frequency or wavelength chirp exhibited by the diode laser for a millisecond injection current pulse. Tektronix function generator (Model no. AFG3252) is used to generate square pulses and laser diode controller from Newport (Model no. 6100) is used to drive the DFB laser diode in pulse mode. The TEC controller circuit keeps the laser temperature stable at 29.68 degree C. The current is switched from 0 mA to 140 mA for 1 millisecond duration at a duty cycle of 90% for the pulse train. Figure 5.5 (a) shows the interferometer fringes as a function of time. It is evident from the rapidly changing fringe density that the wavelength chirp is nonlinear in time domain. Assuming that Optical Path Difference (OPD) between the two arms of the interferometer is constant for the short interval in which laser in ON, it is easy to calculate the laser emission wavelength with time[3]. The result from this calculation is shown in Figure 5.5 (b) and (c). It is clear that the wavenumber $\nu(t)$ change is mostly nonlinear for duration of the pulse and hence measured absorption response $\alpha(\nu(t))$ is expected to be distorted in time.

[3] A discussion on using fringe density to estimate laser wavelength can be found in Appendix C.

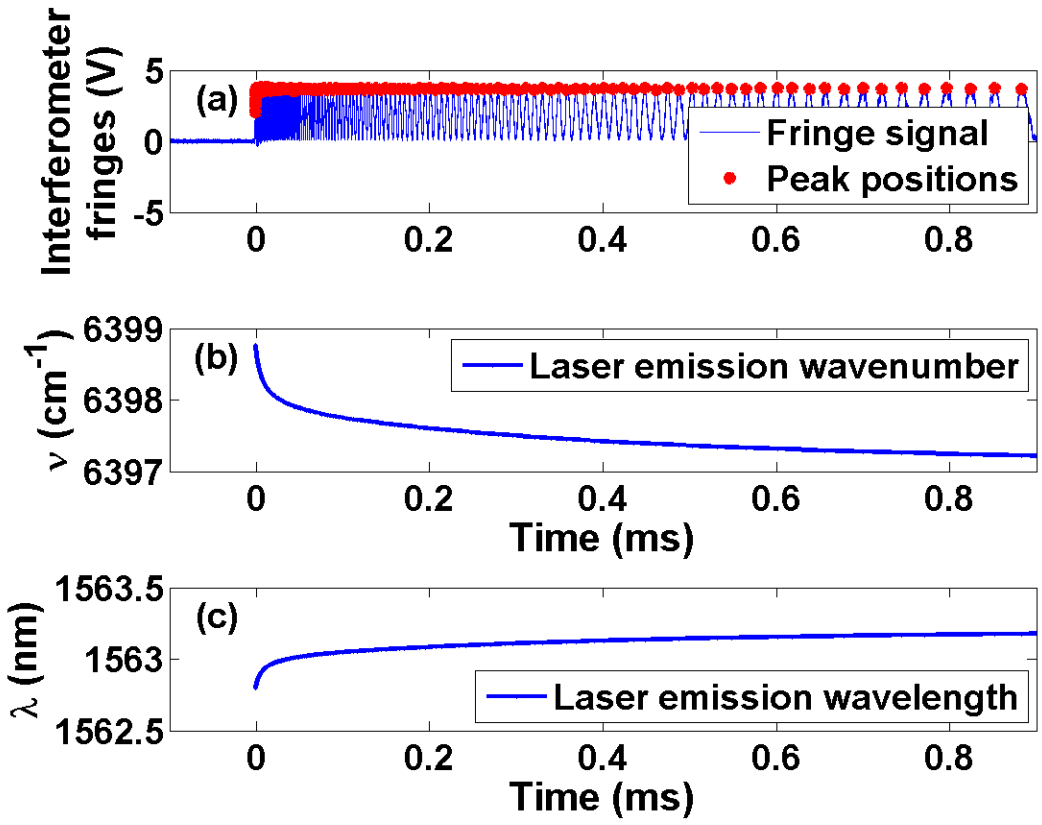

Figure 5.5. (a) Michelson interferometer fringes with peak locations marked, (b) Estimated laser peak emission wavenumber vs. time, (c) Estimated laser emission wavelength vs. time (Total wavelength chirp during the pulse is 379.6 pm or 46.6 GHz).

In order to measure the frequency chirp generated from carrier density change for spectroscopy, a DFB laser diode from JDSU Corporation (Model No. CQF935/808-19550) was used. The emission wavelength is near 1533 nm and suitable to capture acetylene (C_2H_2) line transitions in the near Infrared. Figure 5.6 shows experiment setup for measuring wavelength chirp exhibited by this diode laser. The interferometer used in this setup has a Free Spectra Range (FSR) of 2.55 GHz or 20.4 pm near the wavelength of laser operation. Although smaller FSR yields a more accurate wavelength measurement, it had to be kept large for this system. Because for large Optical Path Difference (OPD) between two arms of the interferometer, nanosecond pulses fail to interfere due to different time of arrival at detector. A voltage pulse generator from AVTECH Electrosystems (Model No. AVI-V-2L-P-VTA) is used to drive the diode laser that has an effective input impedance of 50 Ω. The generator has a maximum pulse

repetition frequency of 100 kHz and a rise/ fall time less than 500 ps. The repetition rate is controlled by a TTL signal generated by a function generator. A laser diode mount (Model No. LM14S2) with bias Tee adapter from Thorlabs is used to feed RF pulse signal to the internal bias Tee of the diode laser module. The internal temperature of the laser is kept fixed at 21.45 degree C by a thermoelectric temperature controller (Model No. TED200C) from Thorlabs. The pulse generator generates a voltage pulse of amplitude 14 V which switches injection current from 0 mA to 280 mA for 5 nanosecond at a repetition frequency of 100 kHz.

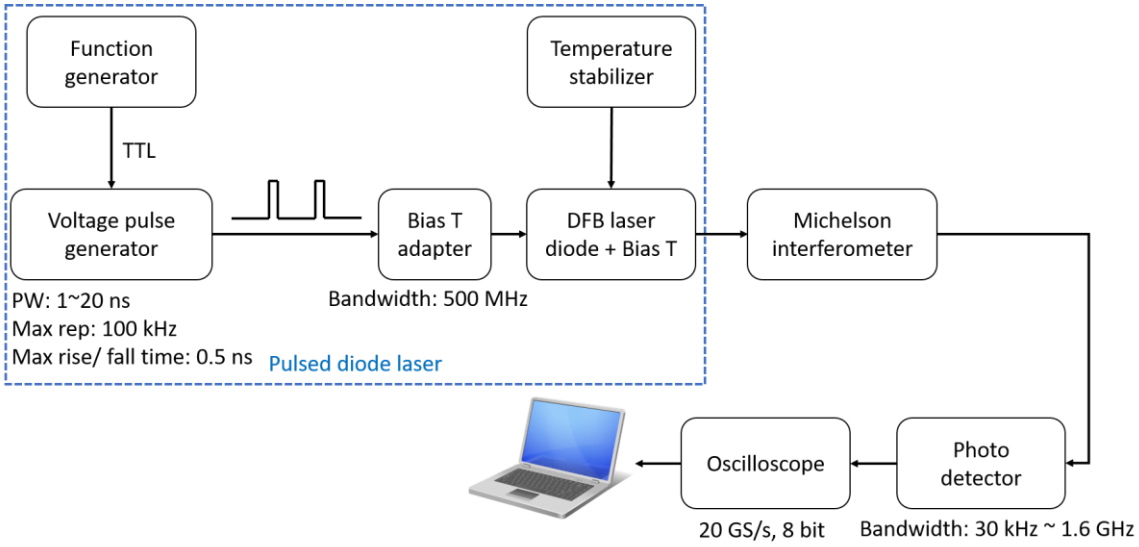

Figure 5.6. Measurement setup for diode laser chirp with 1~20 ns injection current pulse.

Figure 5.7(a) shows the interferometer fringes as a function of time. Assuming that Optical Path Difference (OPD) between the two arms of the interferometer is constant for the short interval in which laser in ON, it is easy to calculate the laser emission wavelength with time[4]. The result from this calculation is shown in Figure 5.7 (b) and (c). Unlike thermal chirp, wavenumber $\nu(t)$ change due to carrier density change appears mostly linear for duration of the pulse. This may be due to the large FSR of the interferometer which fails to capture rapidly changing wavenumber at the beginning of pulse.

[4] A discussion on using fringe density to estimate laser wavelength can be found in Appendix C.

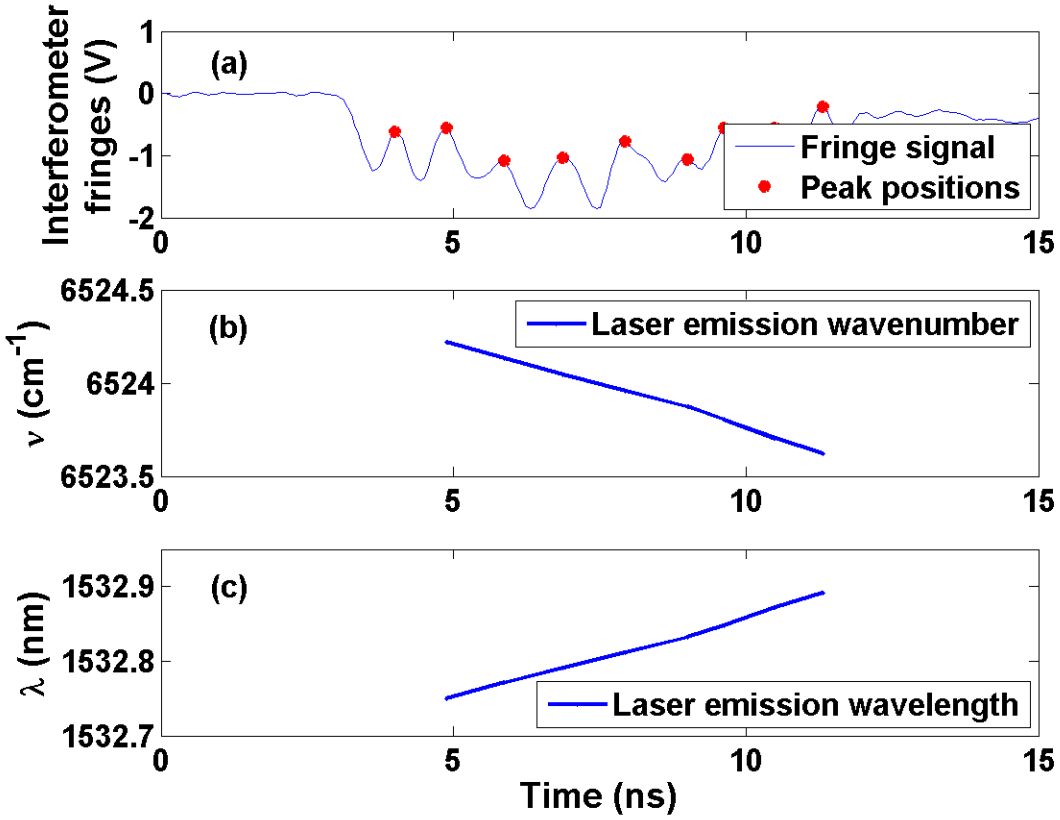

Figure 5.7. (a) Michelson interferometer fringes with peak locations marked, (b) Estimated laser peak emission wavenumber vs. time, (c) Estimated laser emission wavelength vs. time (Total wavelength chirp during the pulse is 141.2 pm or 18.04 GHz).

5.4 System Design for Spectroscopic Measurement by Frequency Chirped Diode Laser

5.4.1 Spectroscopic measurement using millisecond laser pulse

To demonstrate spectroscopic measurement using laser frequency chirp technique, absorption response from 47.6% carbon monoxide (CO)-air mixture with peak at 1563.09 nm was measured by the experimental arrangement shown in Figure 5.8. The laser signal is split into two paths using an optical coupler. A fiber Michelson interferometer with FSR of 222 MHz is placed in one of the arms to track laser wavelength variation in real time while the other arm is used for spectroscopy application. A high power laser diode from NEC Corporation (Model No. NX8570SD654Q-55) is used for this application. The

current is switched from 0 mA to 140 mA for 1 millisecond duration at a duty cycle of 90% for the pulse train. Note that threshold current for this laser diode is 30 mA.

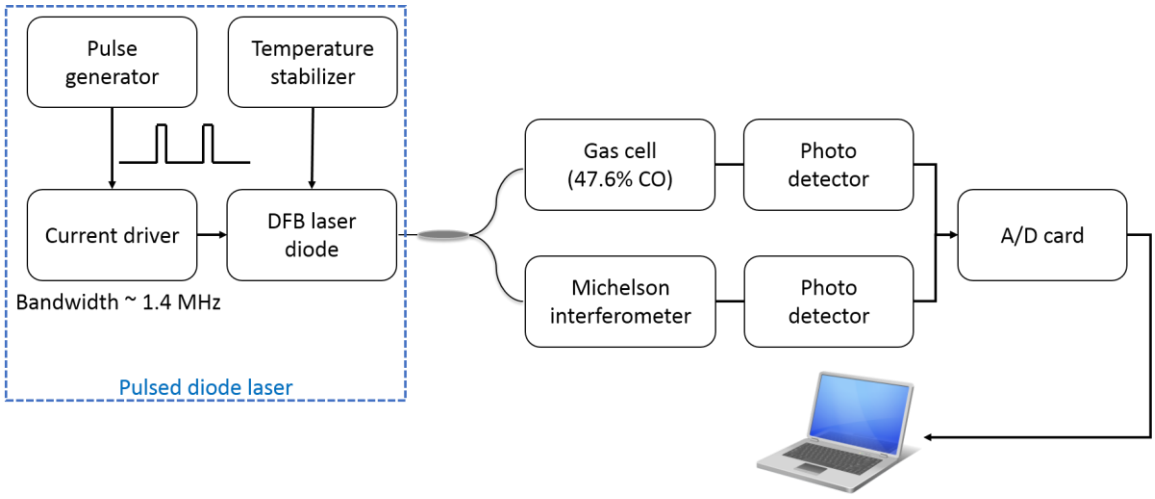

Figure 5.8. Experiment setup for measuring carbon monoxide (CO) absorption signal by laser frequency chirp with millisecond pulse.

Figure 5.9 (a) shows the CO absorption signal observed when laser diode temperature is stabilized at 29.68 degree C. Square wave modulation signals are generated from a function generator (Tektronix, Model AFG3252) and fed to driver from Newport (Model 6100) for driving the laser. The pulse duration is kept at 1 ms for this experiment. At this low modulation frequency, generated frequency chirp is from Joule heating or thermal effect. The temporal behavior of this chirp is recorded by the Michelson interferometer and Figure 5.9 (b) shows the fringe pattern over time. The nonlinear response of $\nu(t)$ slightly distorts the measured absorption response $\alpha(\nu(t))$ in time domain. After laser emission wavenumber has been calculated from the interferometer data, this distortion in absorption response is corrected by spline interpolation in MATLAB. Figure 5.10 (a) shows the estimated wavenumber as a function of time. The absorption signal before and after distortion removal are depicted in Figure 5.10 (b) and (c) respectively. Next the absorbance (αCl) is calculated by normalizing the absorption signal, $I_0\left[1-\alpha(\nu)Cl\right]$, with its baseline intensity (or optical intensity in the absence of gas absorption), I_0, similar to background RAM estimation method in WMS [24–26,74]. Figure 5.11 shows the measured optical depth and its Lorentz profile fit. It is evident that the distortion in

measurement signal has been corrected. The estimated absorbance can be used to make gas parameter measurements.

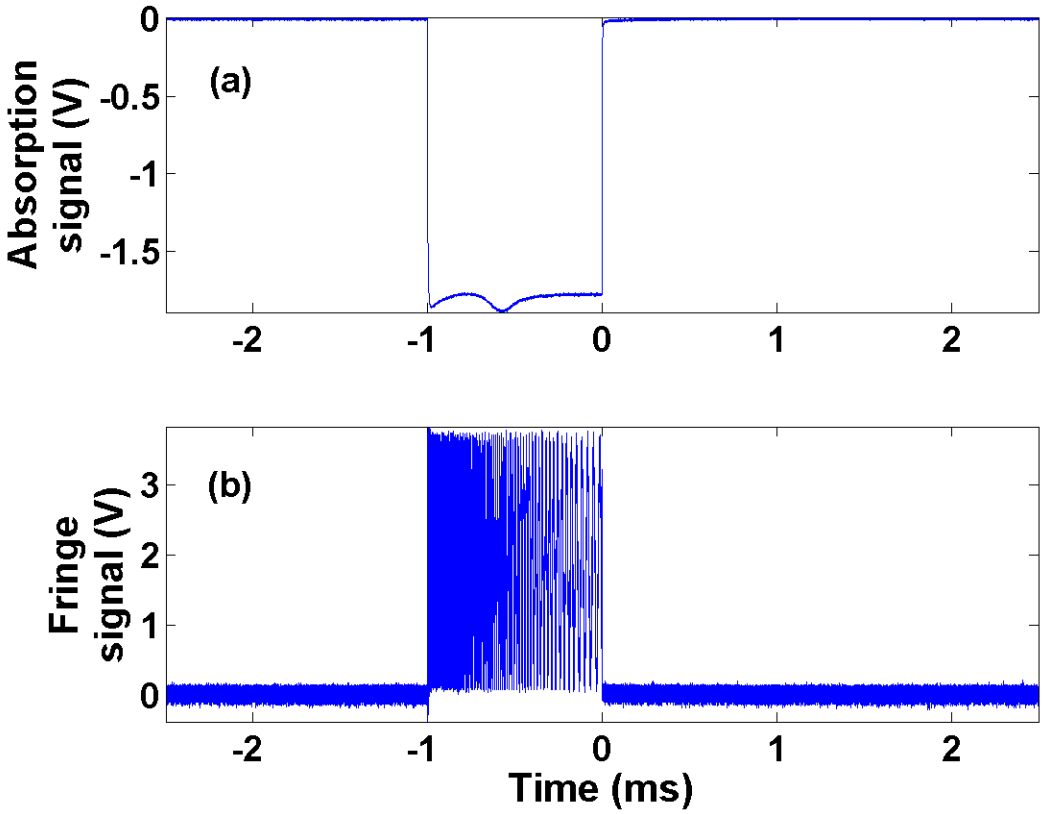

Figure 5.9. (a) Detected optical pulse with CO absorption (pulse signal has been inverted at the balanced detector) response, (b) Fringes from Michelson interferometer to measure the laser wavelength variation in time domain.

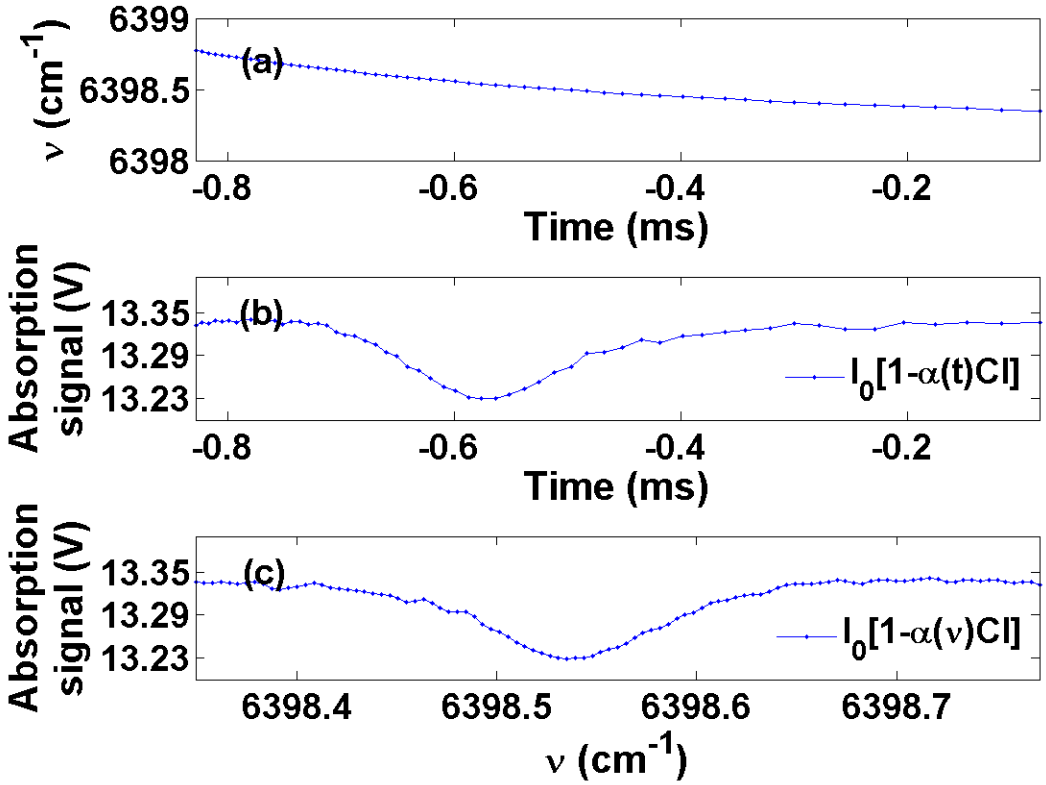

Figure 5.10. (a) Wavenumber chirp estimated from interferometer fringes, (b) Measured spectroscopy signal for carbon monoxide (CO) with distortion in time domain, (c) Distortion corrected spectroscopy signal for carbon monoxide (CO) in wavenumber domain.

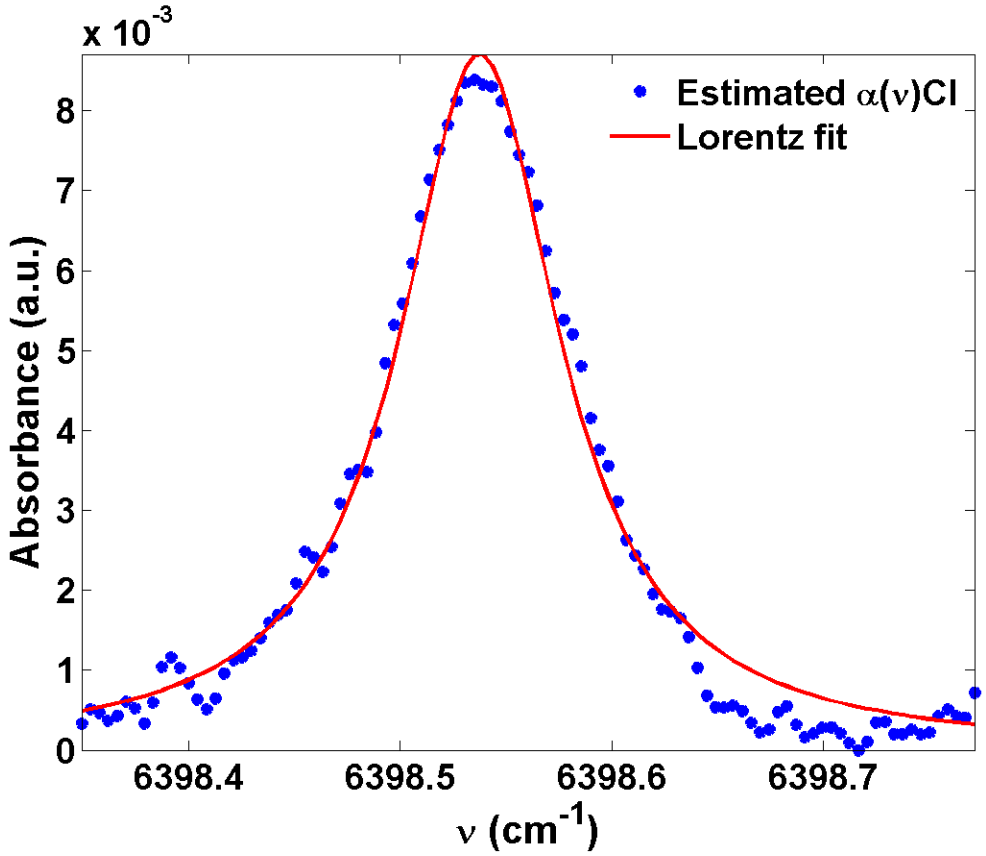

Figure 5.11. Measured absorbance from thermal frequency chirp spectroscopy of carbon monoxide (CO).

5.4.2 Spectroscopic measurement using nanosecond laser pulse

To demonstrate spectroscopic measurement using laser frequency chirp technique with nanosecond pulse, absorption response from different gas mixtures were measured with the experimental arrangement shown in Figure 5.12. A wavelength tracking interferometer is not used in this setup as laser frequency chirp is approximately linear as shown in Figure 5.7 (b).

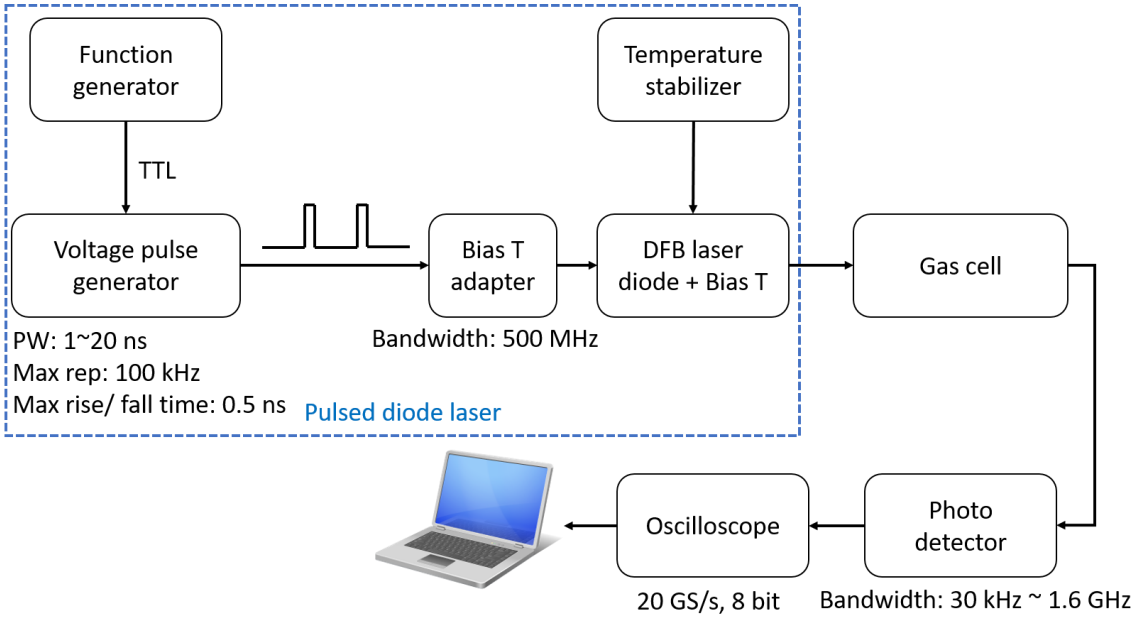

Figure 5.12. Experiment setup for measuring gas absorption signal by laser frequency chirp with nanosecond pulse.

Mixtures of methane (CH_4)-air at three different concentration levels were used to check the performance FC-DLS gas sensor. A diode laser from Inphenix Corporation (Model No. IPDFD1602-1110) was used to record methane absorption response with peak at 1650.96 nm. The laser temperature was set to 22.18 deg C by thermoelectric temperature controller from Thorlabs (Model No. TED200C). The injection current was switched from 0 mA to 70 mA for several nanoseconds at a repetition frequency of 100 kHz. Note that the threshold current for this diode laser is 5 mA. Figure 5.13 shows the voltage pulse measured at the photodetector for approximately 5%, 10%, and 20% methane-air mixtures with a 6.35 cm long cavity gas cell. It is evident that with increased concentration of methane, the absorption signature becomes stronger in the detected pulse. The optical pulse in the absence of any gas is used as a baseline intensity signal to make self-calibrated estimation of the absorbance, αCl. Note that, due to large optical depth values in this experiment, optical intensity is given by exponential relation (Eq. (5.3)) instead of the linear approximation in Eq. (2.10).

$$\begin{aligned} I_{out,no\ gas}(t) &= I_{in}(t) \\ I_{out,with\ gas}(t) &= I_{in}(t)e^{[-\alpha(t)Cl]} \end{aligned} \tag{5.3}$$

In this case, gas absorbance was calculated by Eq. (5.4). Figure 5.14 shows the calculated absorbance along with theoretically expected Lorentz profile.

$$\alpha(t)Cl = \log_e\left(I_{out,no\ gas}(t) / I_{out,with\ gas}(t)\right) \tag{5.4}$$

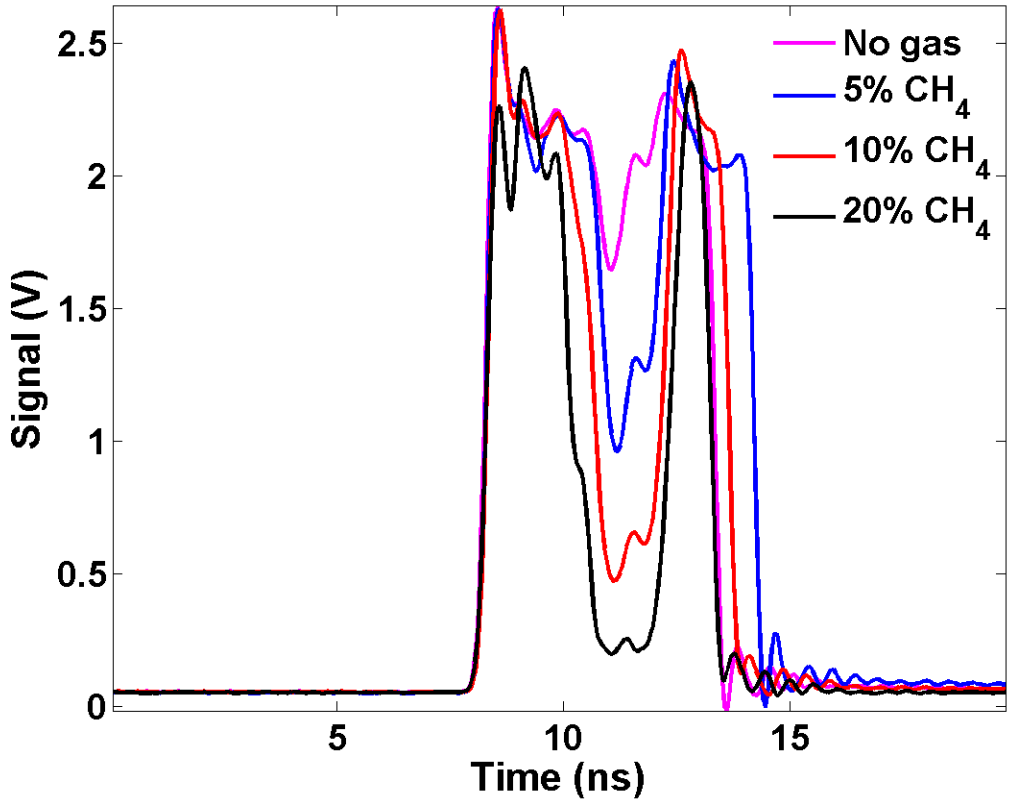

Figure 5.13. Nanosecond laser frequency chirp spectroscopy of methane (CH_4) at different concentration levels.

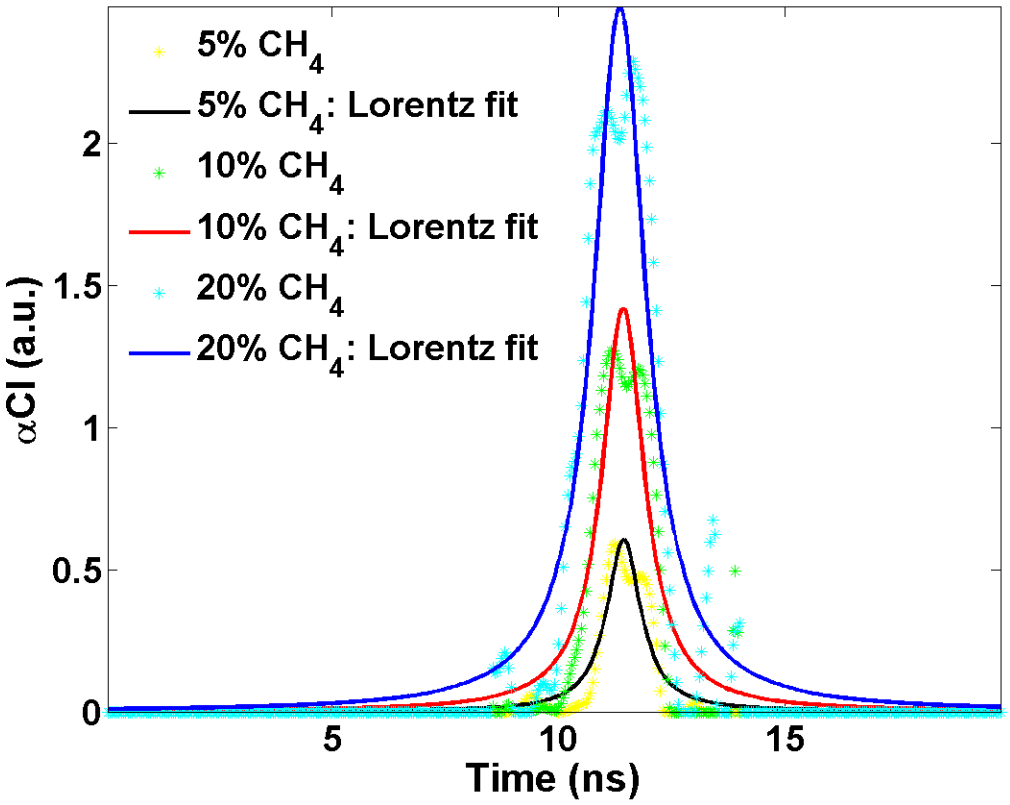

Figure 5.14. Extracted methane (CH_4) absorbance from laser frequency chirp spectroscopy at different concentration levels.

To find the baseline intensity (i.e. optical pulse without any gas interaction), one can use two separate optical channels and photodetectors for measuring with and without gas conditions. But a simpler solution is to operate the system in reflection mode and measure the baseline intensity pulse and pulse with gas absorption information by the same detector. This design is shown in Figure 5.15. Henceforth, the reflected optical pulse used for estimating baseline intensity is referred to as *reference* pulse.

This reference reflection pulse is generated by a mirror while the reflection pulse with gas absorption is generated by the gas sensor or cell. As the reference pulse travels a shorter distance compared to sensor pulse, they can be separated in time domain. Figure 5.16 shows the two pulses detected on such a system. There is an 83 ns delay between the sensor pulse and reference pulse which corresponds a path difference of approximately 8.5 meters along a single mode. For this experiment, the target gas was acetylene (C_2H_2). Its absorption peak, located at 1532.83 nm, was measured by a diode laser from JDSU

Corporation (Model No. CQF935/808-19550). The laser temperature was set to 17.41 deg C by a thermoelectric temperature controller from Thorlabs (Model No. TED200C). The injection current was switched from 0 mA to 290 mA for several nanoseconds at a repetition frequency of 100 kHz.

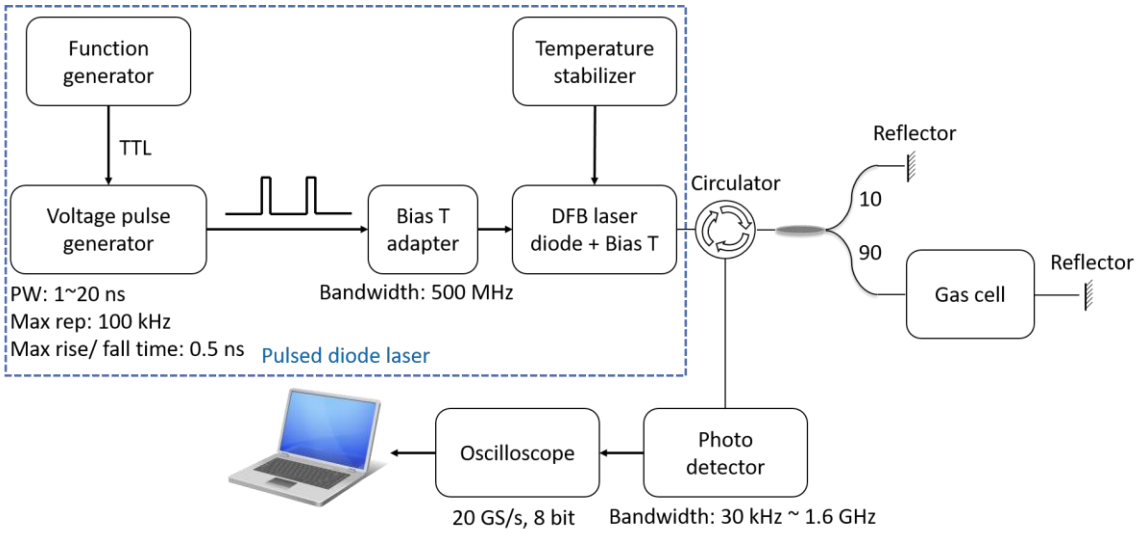

Figure 5.15. Experiment setup for measuring acetylene (C_2H_2) absorption signal by laser frequency chirp with reference reflection pulse.

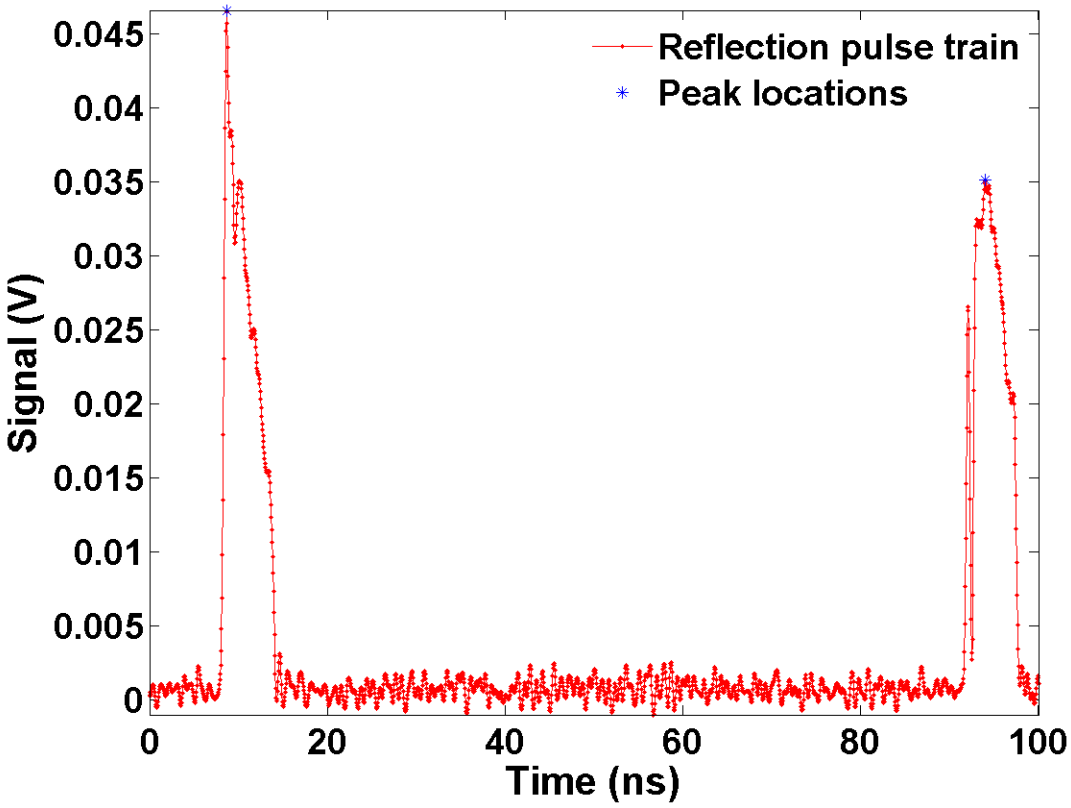

Figure 5.16. Measured reflection pulse train from laser frequency chirp spectroscopy of acetylene (C_2H_2). Reference reflection pulse arrives first at the detector followed by reflection pulse from gas sensor.

Next the absorbance, αCl, is calculated by normalizing the sensor pulse with absorption by a scaled copy of the reference pulse. In Figure 5.17 (a) the isolated reference pulse is shown. Figure 5.17 (b) depicts the situation when reference pulse has been properly scaled and aligned with the sensor pulse. Signal cross-correlation approach is used to align these two pulses in time domain and the non-absorbing sections of both pules are used to estimate required scaling factor. Due to large optical depth values in this experiment, Eq. (5.4) was used to for calculation by replacing $I_{out,no\ gas}(t)$ with aligned and scaled reference pulse.

Figure 5.18 depicts the calculated absorbance with theoretically expected Lorentz fit. It is clear that measured gas concentration from optical depth (αCl_{max}) is independent of optical intensity. In other words, new high speed FC-DLS system is capable of making

calibration-free gas absorbance measurements like conventional WMS systems. Hence, it can be used for long-term applications in harsh environments.

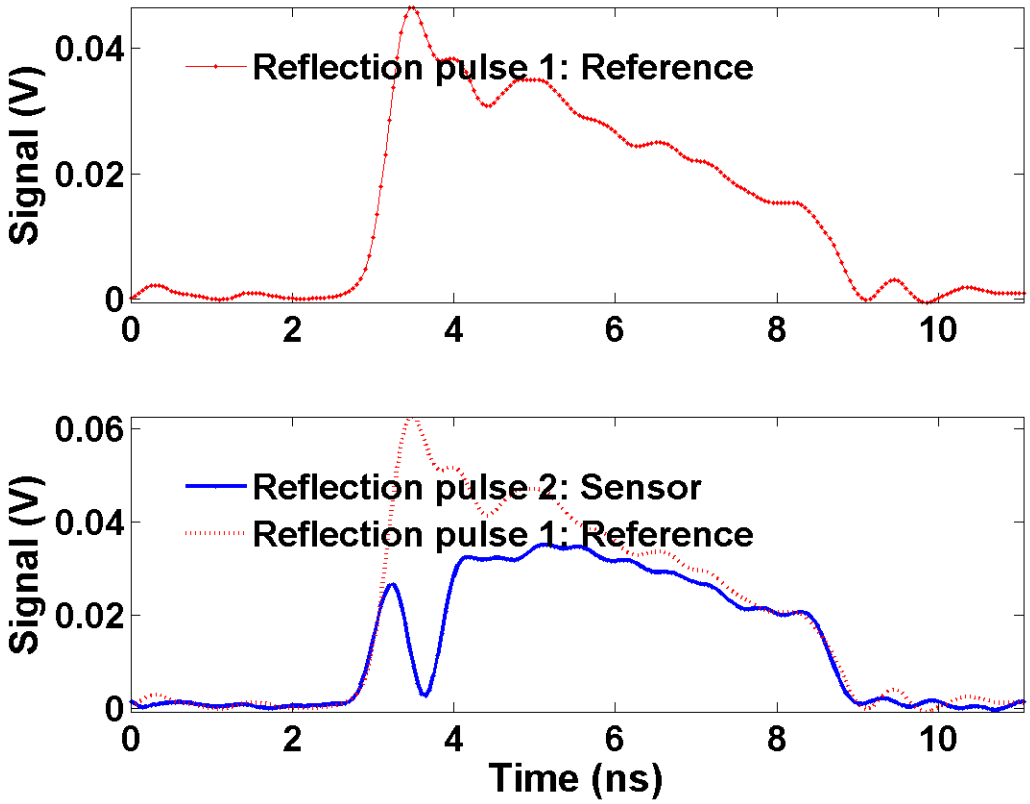

Figure 5.17. (a) Isolated reference reflection pulse, (b) Reflection pulse from gas sensor and a scaled copy of reference reflection to act as baseline intensity.

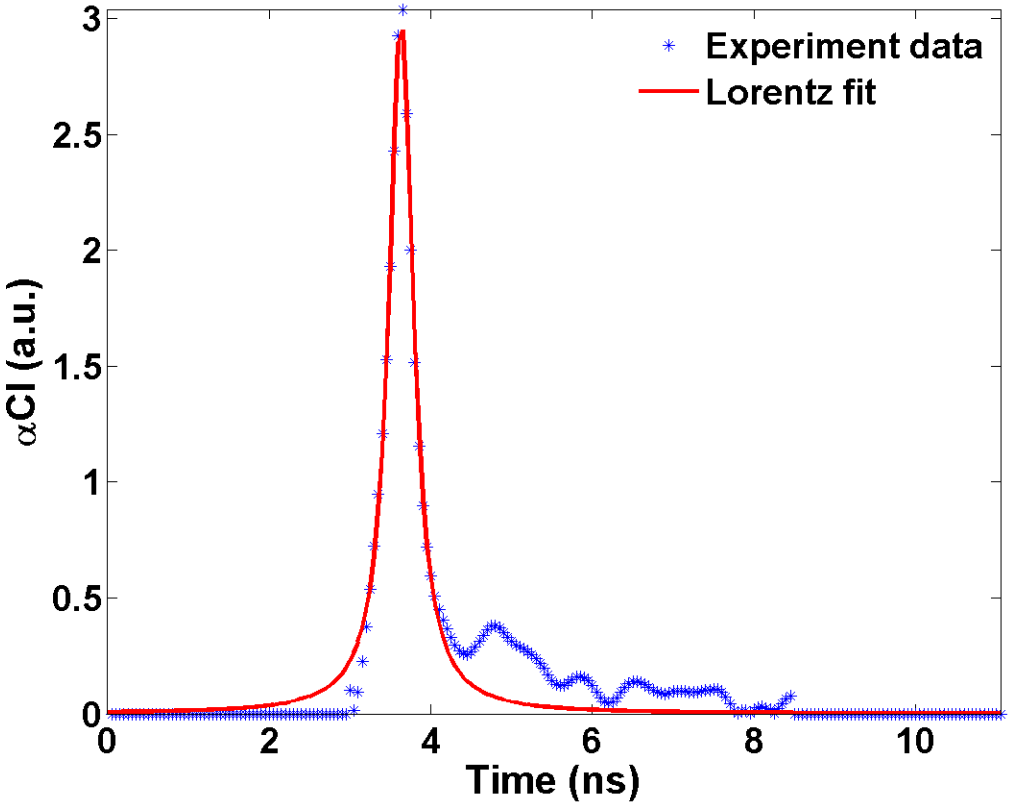

Figure 5.18. Measured absorbance from nanosecond frequency chirp spectroscopy of acetylene.

To test the sensitivity and accuracy of nanosecond frequency chirp spectroscopy system, absorption optical depth was measured by changing acetylene concentration near the gas cell. This gas cell has 6.35 cm long open cavity for light-gas interaction. The system setup is same as that shown in Figure 5.15. But the gas cell is kept inside a quartz vacuum chamber so that it can be exposed to different acetylene concentration levels. *Partial pressure based mixing* and *dilution* technique is used to change acetylene-air mixture ratio inside the chamber[5]. Optical pulse train measured at each gas concentration level corresponds to an average of 100 consecutive scans. The absorption response αCl is estimated by using Eq. (5.4) and replacing $I_{out,no\ gas}(t)$ with aligned and scaled reference reflection pulse. Figure 5.19 (a) shows the recovered absorption signal from three such measurements at 5.93%, 4.24% and 2.91% acetylene concentrations. Then Lorentz curve

[5] A discussion on preparing different gas concentration mixtures using their partial pressure and dilution technique can be found in Appendix B.

fit is used over the experimental data to reduce the noise and estimate maximum absorbance or optical depth (αCl_{max}) in a robust manner. Finally, experimentally measured optical depth is plotted against the gas concentration inside the chamber for 0.41% to 20.6% acetylene mixture. This response curve is shown in Figure 5.19 (b) with error bars from ten sensor readings. From the linear relation between measured optical depth and gas concentration, it is evident that spectroscopic measurement by FC-DLS method is quite accurate. The accuracy of this system is about ±300 ppm or 1.4% of sensor reading (whichever is greater). The sensitivity is about 4000 ppm, but it can be improved with a more stable laser pulse and by increasing the number of laser scans used for averaging at each concentration level.

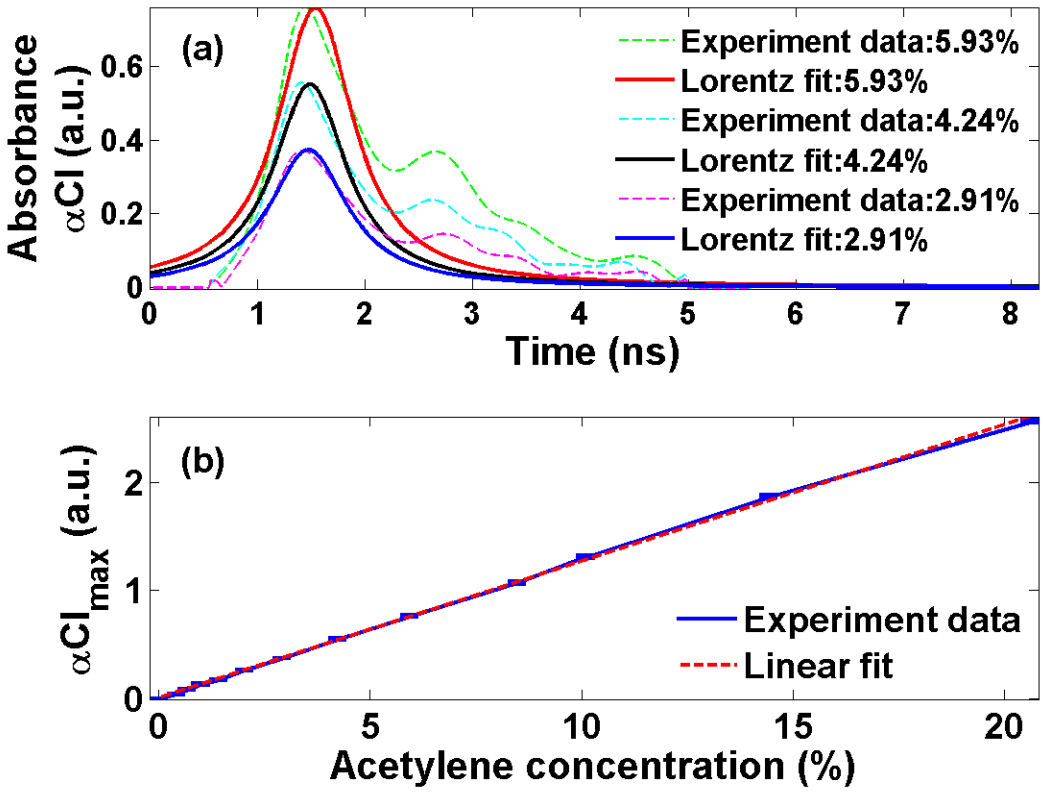

Figure 5.19. (a) Absorption response curves at different concentration levels of acetylene, (b) Optical depth vs. acetylene concentration levels.

Gas pressure measurement using FC-DLS technique is demonstrated by placing the gas cell from Figure 5.15 in a sealed vacuum chamber and controlling the chamber pressure.

Acetylene absorbance is measured for a pressure range of 73 to 100 kPa. Figure 5.20 (a) shows the recovered absorption signal from three such measurements at 76 kPa, 82 kPa, and 97 kPa. Lorentz curve fit is used over the experimental data to reduce the noise and estimate FWHM of absorbance (αCl) in a robust manner. Experimentally measured FWHM is plotted against the chamber pressure for approximately 4% acetylene-air mixture. This response curve is shown in Figure 5.20. (b) with error bars from ten sensor readings. It should be noted that FWHM values of absorbance have been indicated in nanoseconds as they are calculated from harmonic signals measured in time domain. From the linear relation between experimentally measured FWHM and pressure, it is evident that recovered absorbance from FC-DLS is quite accurate. The accuracy of gas pressure estimation by this approach estimated to be ±1.03 kPa in the range 73 to 100 kPa. But it can be improved with a more stable laser pulse and by increasing the sampling rate for digitization. Because the change in FWHM of absorbance due to pressure variation is small and hence larger number of samples near the absorption peak make tracking these changes easier.

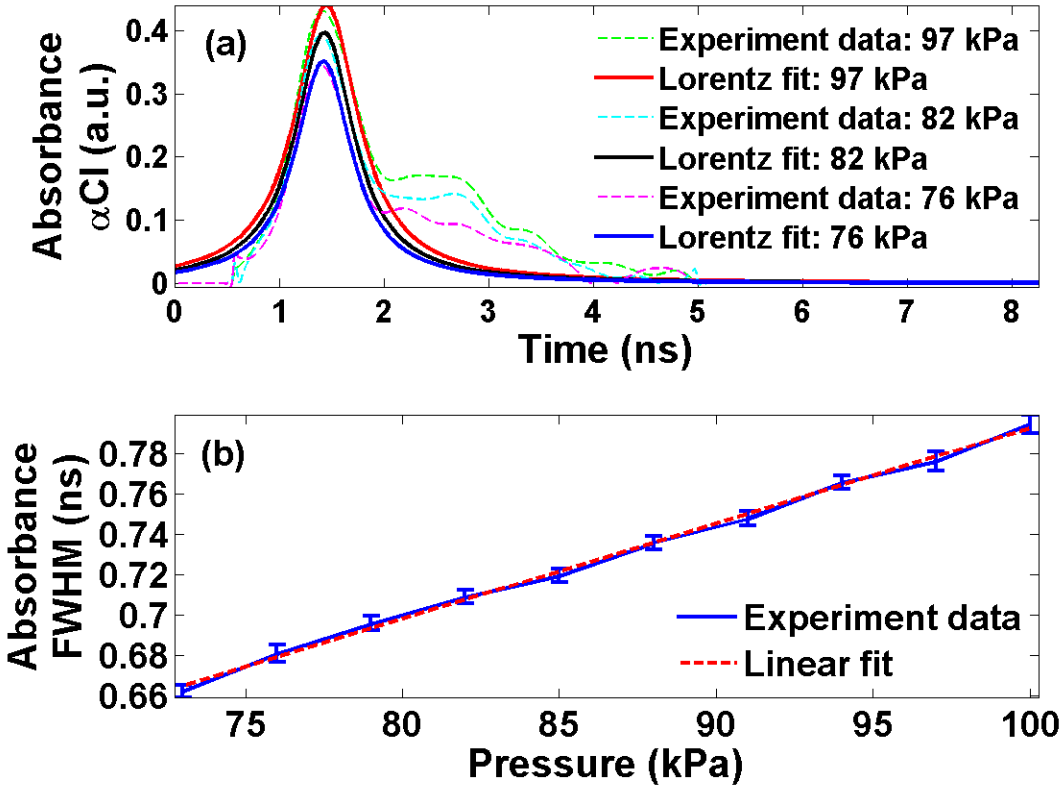

Figure 5.20. (a) Absorption response curves at different gas pressure levels for acetylene, (b) FWHM of absorbance vs. gas chamber pressure.

5.5 Demonstration of Spatially Distributed Gas Sensing

As frequency chirp spectroscopy is carried out by nanosecond optical pulses, this technique can be used to interrogate multiple sensing elements connected in succession along one optical fiber. Furthermore, the diode lasers used for demonstrating frequency chirp spectroscopy operate in the telecomm optical wavelength band (near 1550 nm), and thereby suffer less than 0.2 dB/km attenuation along a single mode silica fiber. Hence, by using traditional OTDR technique, spatial location of each gas sensing element can be estimated with a single detector.

In Figure 5.21, the basic design of quasi-distributed gas sensing by FC-DLS is explained. A diode laser with suitable emission wavelength for the target gas is driven by injection current pulses to generate a frequency chirp. This laser pulse is delivered to a single mode fiber via an optical circulator. Several miniature gas sensing elements are serially

connected along this single mode fiber and the minimum physical separation between them is decided by the spatial resolution achievable by the laser interrogator. Each sensing element reflects a small portion of the laser pulse and transmits the rest along the fiber. All reflected pulses are collected by a photodetector and converted to voltage waveforms. A high speed oscilloscope records these voltage waveforms and their times of arrival. One reference reflection pulse is used to perform calibration-free measurement of gas concentrations for all the sensing elements.

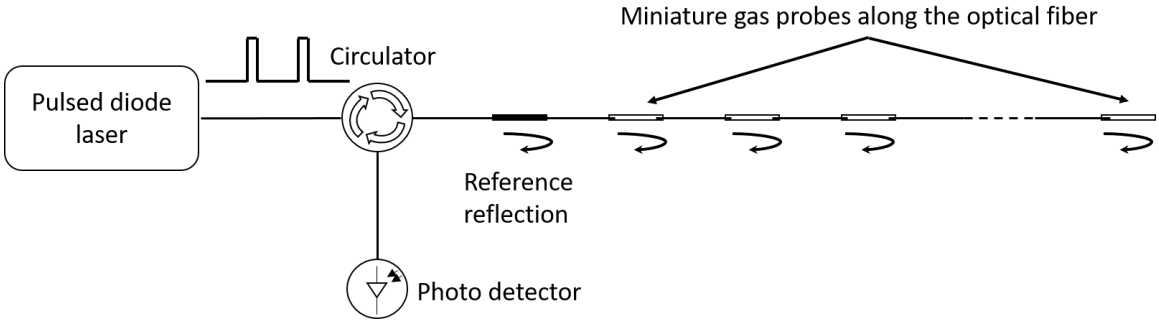

Figure 5.21. Principle of quasi-distributed gas sensing with frequency chirped diode laser spectroscopy.

Time of flight (TOF) calculation for determining spatial location of different sensing elements is explained in Figure 5.22. Let sensor 1 and 2 be located L_1 and L_2 distance away from the reference reflector respectively. The reflection pulses from these two sensor will arrive at different time. If Δt_1 and Δt_2 are the relative time of arrivals for sensor 1 and 2 respectively, their spatial locations relative to the reference reflector can be calculated by

$$L_{1,2} = \frac{c}{2n_{eff}} \Delta t_{1,2} \tag{5.5}$$

where $n_{eff} = 1.4682$ is the effective group index of refraction for SMF-28 fiber from Corning.

Similarly, spatial resolution for the sensor system is given by Eq. (5.6) where *PW* represents the width of the voltage pulse measured at photodetector. If laser injection current has 10 ns pulse width, the spatial resolution is approximately 1 meter.

$$d = \frac{c}{2n_{eff}}(PW) \tag{5.6}$$

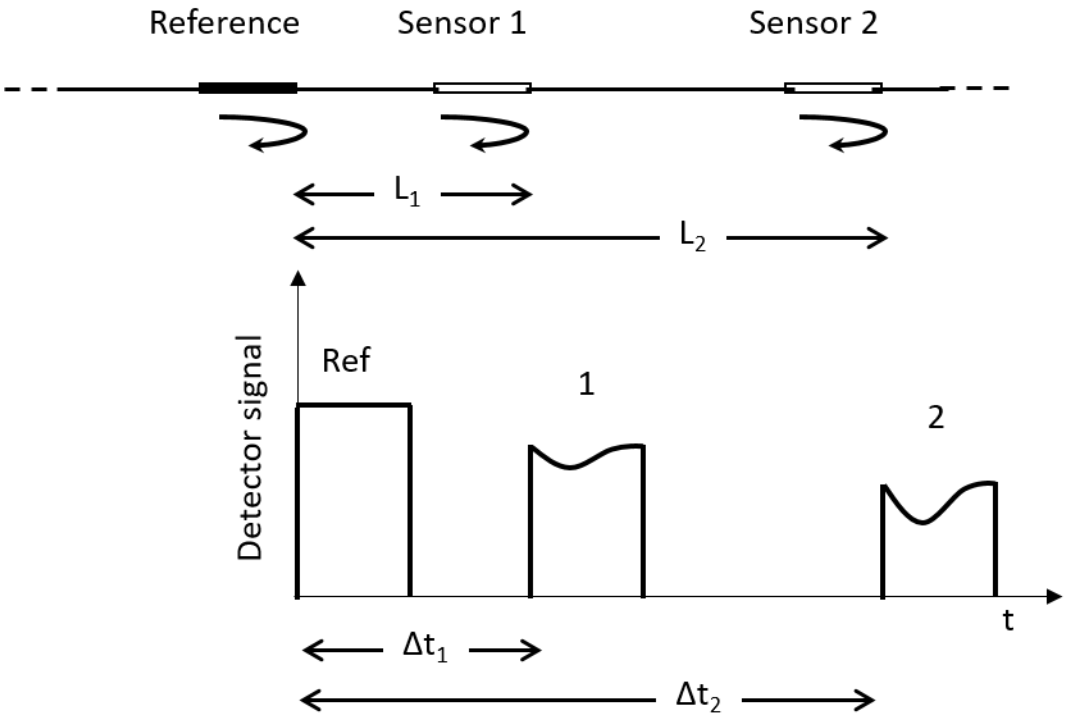

Figure 5.22. Spatial location estimation for the sensing elements from their times of arrival.

In order to demonstrate spatially distributed gas measurement by FC-DLS, the experimental arrangement in Figure 5.23 is used. Fiber optic couplers with 90/10 power splitting ratio and fiber pigtailed mirrors are used to generate partial reflection from each gas sensing element. The sensing elements are 6.35 cm long gas flow cells with optical collimators at both ends and are filled with target gas acetylene. The optical fibers connecting these elements in series are represented as 'fiber coil' in the diagram. DFB diode laser from JDSU Corporation (Model No. CQF935/808-19550) is used as the light source. The laser operating condition is same as that used for single point acetylene detection in Section 5.4.2.

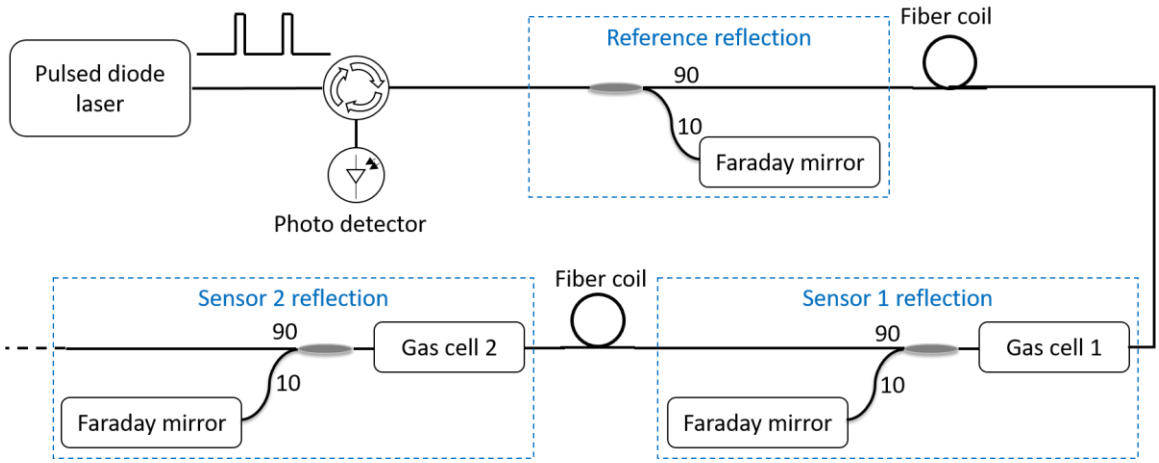

Figure 5.23. Experiment setup for quasi-distributed gas sensing with frequency chirped diode laser spectroscopy.

The voltage pulse train measured at the detector are shown in Figure 5.24. After each pulse is isolated and properly aligned in time domain by signal cross-correlation, appropriate scaling factor is applied on the reference pulse to obtain a baseline intensity for all sensor signals. Figure 5.25 shows all three isolated pulses and their baseline intensities obtained from the reference pulse. Then the absorbance value is calculated by using Eq. (5.4). It should be noted that the pulse from sensor 2 records absorbance from both sensor 1 and 2 as they are connected in succession and light reflected from sensor 2 passes through both sensors. Therefore, absorbance calculated sensor 1 pulse needs to be subtracted from the absorbance calculated from sensor 2 pulse to measure the correct gas concentration at sensor 2. Figure 5.26 shows the absorbance values recorded at sensor 1 and 2 after this subtraction has been carried out. A Lorentz curve fit is also provided on the experiment data that can be used for more robust estimation of concentration.

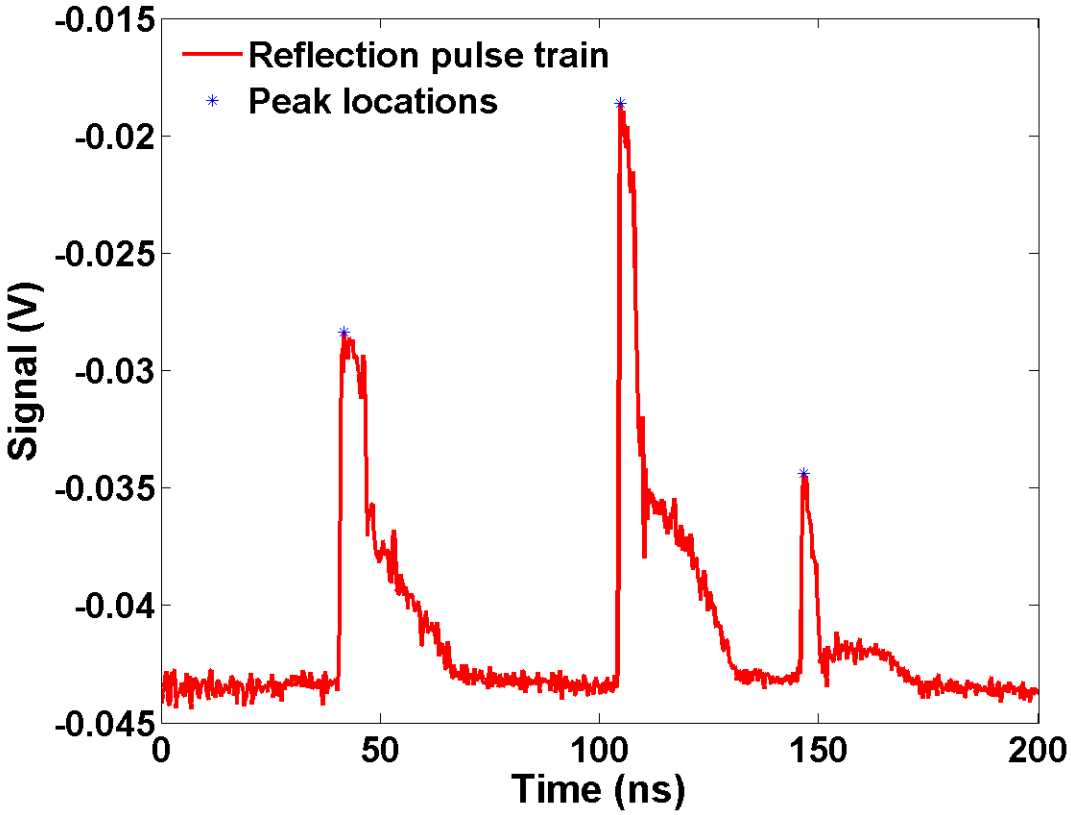

Figure 5.24. Measured reflection pulse train for spatially distributed measurement of acetylene. Reference reflection pulse arrives first followed by the two reflection pulses from two serially connected gas sensors.

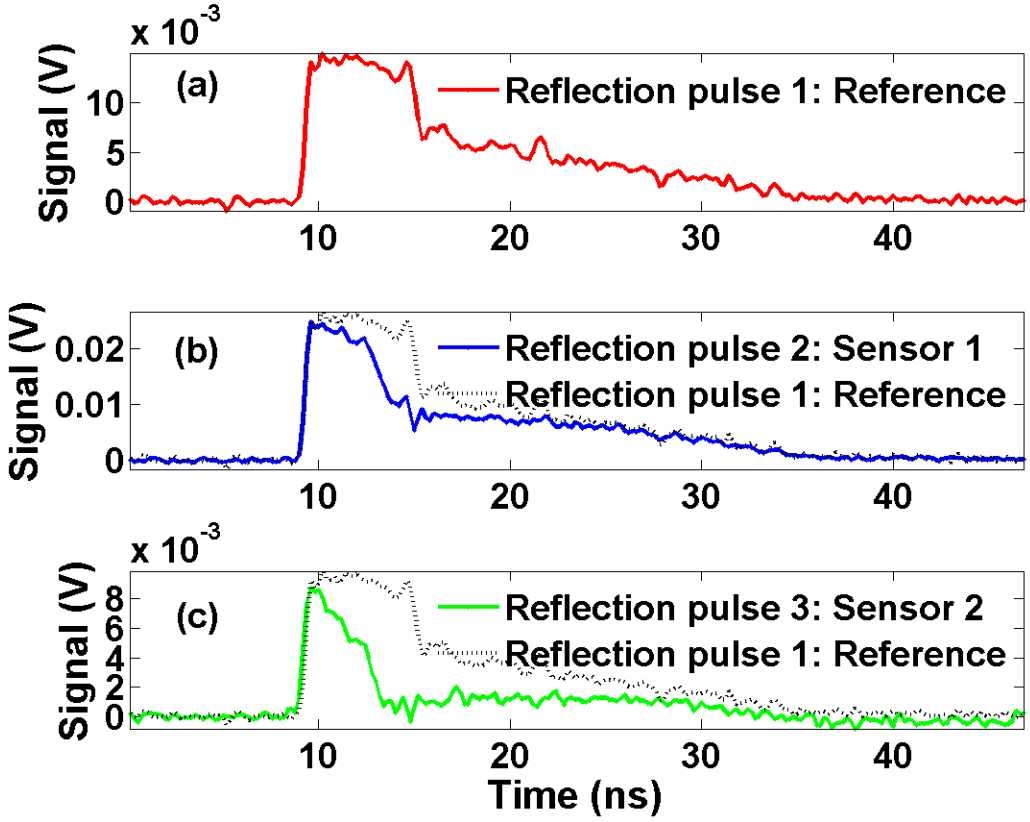

Figure 5.25. (a) Isolated reference reflection pulse, (b) Reflection pulse from gas sensor 1 and scaled reference reflection to matching the background, (c) Reflection pulse from gas sensor 2 and scaled reference reflection to matching the background.

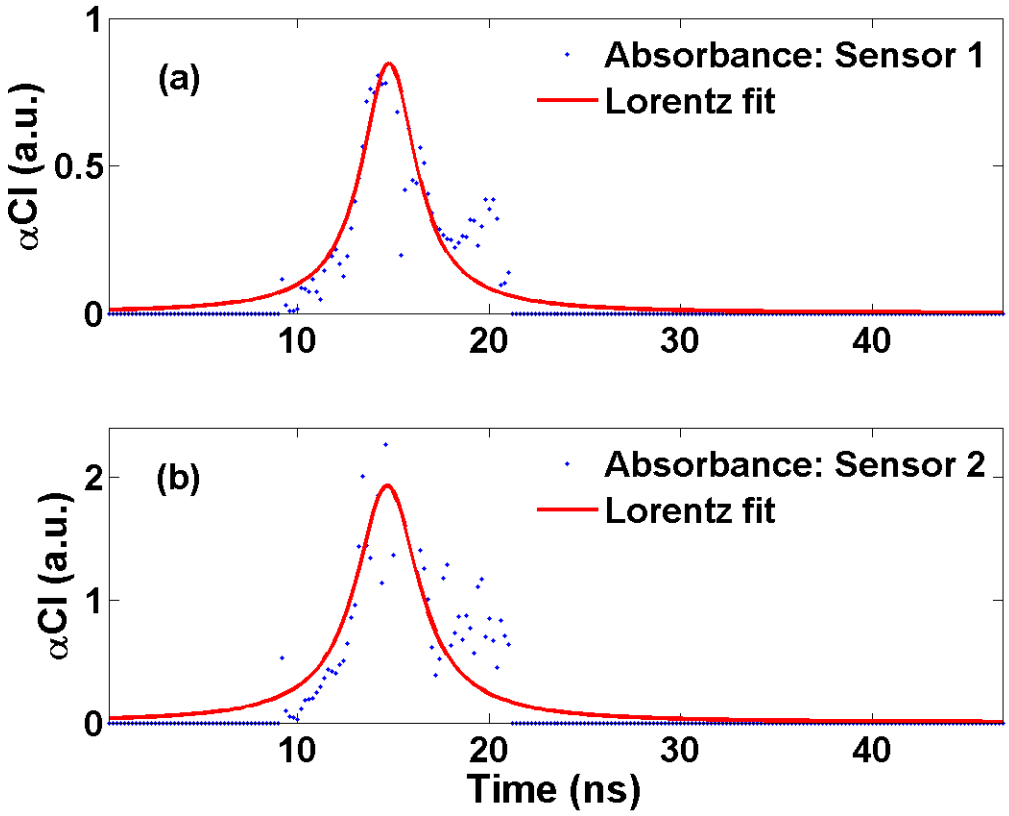

Figure 5.26. (a) Absorption response from gas sensor 1 with Lorentz fit, (b) Absorption response from gas sensor 2 with Lorentz fit.

5.6 Advantages and Limitations

5.6.1 Advantages

One of the key advantages of distributed gas sensing by FC-DLS approach is that it uses low cost and robust optical components from the telecomm market. Moreover, using single mode telecomm fiber and diode lasers operating near 1550 nm wavelength, a sensing span of several kilometers can be easily realized. Another advantage is that FC-DLS system is not specific to particular gas, but can be applied to any gas that has decent absorption strength in the near infrared region. Gases like acetylene, methane, carbon monoxide, carbon dioxide, hydrogen sulfide, and nitric oxide can be monitored in a distributed manner using the proposed system by simply changing diode laser source. In other words, the same chain of sensor probes can be used to simultaneously monitor multiple gases by using wavelength-division-multiplexing (WDM) and launching the

combined light from all diode lasers in the sensing fiber. FC-DLS also allows one to capture the full absorption response spectrum ($\alpha(\nu)Cl$) without any on-site calibration. Hence, besides gas concentration, information like its temperature and pressure can be estimated by applying the curve fitting methodology described in Chapter 3. Finally, a spatial resolution of 1 meter or lower can be realized due to the narrow pulse width used in this system.

5.6.2 Limitations

Unlike TDLS with wavelength modulation, frequency chirp spectroscopy is not a single frequency detection. Without lock-in amplifier noise rejection in the system, a wide bandwidth of noise is captured at the detector. One of the primary source of noise in this system is laser injection current jitter which can translate to intensity as well as wavelength fluctuations. Laser intensity noise generated from this pulse jitter is simply added to the absorption response. If this noise is not in the same frequency band as the desired absorption signal, it can be removed by a digital filter. However, wavelength fluctuations due to pulse jitter can distort the shape of absorption response ($\alpha(\nu)Cl$) as it is a nonlinear function of ν. These distortions are often impossible to correct and can only be slightly reduced by curve fitting (Lorentz profile or Voigt profile) the experimental data. An ideal flat top current pulse can avoid these wavelength and intensity jitters. But in practical applications, voltage or current pulse generators always present some oscillations in their output.

Chapter 6 Conclusions and Future Work

6.1 Conclusions

In this work, commercial telecomm laser diodes have been used to achieve single point and spatially distributed gas sensing. Single point monitoring is accomplished by wavelength modulation spectroscopy (WMS) as it provides better signal-to-noise ratio, and hence better sensitivity to trace gases compared to TDLS with direct detection. Being *calibration-free* is the key for applying any gas sensing technology in practical industrial environments. However, existing techniques for calibration-free WMS impose multiple limitation on system operating conditions and lead to erroneous measurements if those conditions are not met. In some cases, extensive pre-characterization of diode laser parameters is needed to simulate the expected harmonic signals in real time and iteratively match with those obtained from measurement. But this is not suitable in applications that are intended for long-term applications, because future measurements may show errors due to drift from pre-characterization test conditions, temperature variations, or aging of laser diode. All these limitations are mitigated by a new signal processing algorithm for measured harmonics. By exploiting the symmetric nature of absorption response and its time derivatives, RAM contributions are successfully extracted from the WMS harmonics. Then second harmonic RAM term is normalized by the RAM term in first harmonic to recover gas absorbance. This new RAM normalization process is more robust and stays unaffected by changes in $\Delta I / I$ value or other laser operating conditions, it adds great flexibility to field installation of WMS gas monitoring system such as replacing a laser diode or switching modulation frequency for accommodating additional target gases. Furthermore, the normalization process yields the absolute absorption line shape function which can be used to predict several gas parameters like concentration, pressure, and temperature by applying Lorentz/ Voigt fitting.

Based on the above mentioned algorithm, RAM contributions in the measured first and second harmonic signals from 1% and 8% methane-nitrogen mixture have been recovered. The same method is used to compute the optical depth (maximum value of

absorbance, αCl) and FWHM of absorbance in time domain while pressure varies from 60 to 100 kPa. These experimental results demonstrate the simultaneous estimation of gas concentration and pressure from its absorption response. RAM normalization technique is also experimentally validated by changing the optical transmission loss by 12 dB in the system. Even though amplitude of first and second harmonic signals change by 12 dB due to optical intensity change, the normalized amplitude of second harmonic RAM remained constant. This experimentally validates that proposed signal processing algorithm has achieved a calibration-free gas sensor.

Additionally, spatially distributed gas monitoring is accomplished by new frequency chirped diode laser spectroscopy (FC-DLS) with direct detection. Diode lasers are operated in pulse mode by applying an injection current pulse of nanosecond duration. As a result of this current modulation, laser emission frequency is chirped. After keeping the laser mean emission frequency fixed (by keeping laser temperature constant), chirp interval is used to automatically scan the absorption spectrum of target gas and measure its absorbance. Since the laser pulse has a very narrow temporal width, traditional OTDR technique is then used to estimate the spatial location of sensor using time-of-flight calculation.

The feasibility of FC-DLS method is experimentally demonstrated by measuring absorbance (αCl) for approximately 5%, 10%, and 20% methane-air mixture using a 6 nanosecond injection current pulse. Since gas mixture is kept at room temperature and atmospheric pressure, absorption response is expected to follow a Lorentz profile. This theoretical prediction is verified by a curve fit on experimental data. It is also shown that FC-DLS technique can realize calibration-free measurement of gas properties by operating the sensor system in reflection mode and using a reference optical pulse (pulse not interacting with target gas) for sensor signal normalization. Absorbance measured by this approach is self-calibrated and can easily be applied in industrial environment. Furthermore, the ability to measure full absorption response, $\alpha(\nu)Cl$, can be used to estimate multiple gas parameters like concentration, pressure, and temperature by applying Lorentz/ Voigt fitting. An acetylene-air mixture for 5000 ppm to 200,000 ppm concentration levels has been used to prove the accuracy and sensitivity of FC-DLS gas

sensor. The experimental demonstration of spatially distributed gas monitoring is also carried out by measuring acetylene absorbance from two sensor probes connected in series along a single mode fiber. With a 10 nanosecond laser pulse, a spatial resolution of 1 meter has been shown.

Diode laser spectroscopy based gas monitoring methods described in this dissertation are quite flexible and can be easily implemented to detect single or multiple gas species by choosing diode lasers of suitable wavelength. At the same time, the sensor system can be kept low cost as it operates in the standard telecomm wavelength band and optical components are readily available. For example, FC-DLS is quite attractive approach for distributed hydrocarbon leakage monitoring along natural gas pipelines. The optical power attenuation coefficient for standard single mode fiber is very low and a sensing span of several kilometers is easy to realize. In addition to these benefits, both WMS and FC-DLS schemes are calibration-free systems and hence excellent choice for long-term applications in harsh industrial environments where gas concentrations needs to be measured under varying pressure or temperature and frequent maintenance is not an option.

6.2 Recommendations for Future Work

The experiment results have demonstrated that the proposed FC-DLS technique shows great promise in achieving quasi-distributed gas measurement. But there are number of challenges which need to be addressed for this technology to become more practical.

6.2.1 Injection current pulse

In the experiments, a voltage pulse generator has been used to indirectly modulate laser injection current. Ideally, a flat-top pulse is preferred to keep the laser frequency chirp monotonic in time. But voltage output of the nanosecond pulse generator has a lot of fluctuations in its value as can be noticed in Figure 6.1. Consequently, laser injection current is not ideal and measured gas absorption response is affected by both intensity and frequency (or wavelength) fluctuations which are extremely difficult to correct. Therefore, improving the injection pulse quality should be major task in the future.

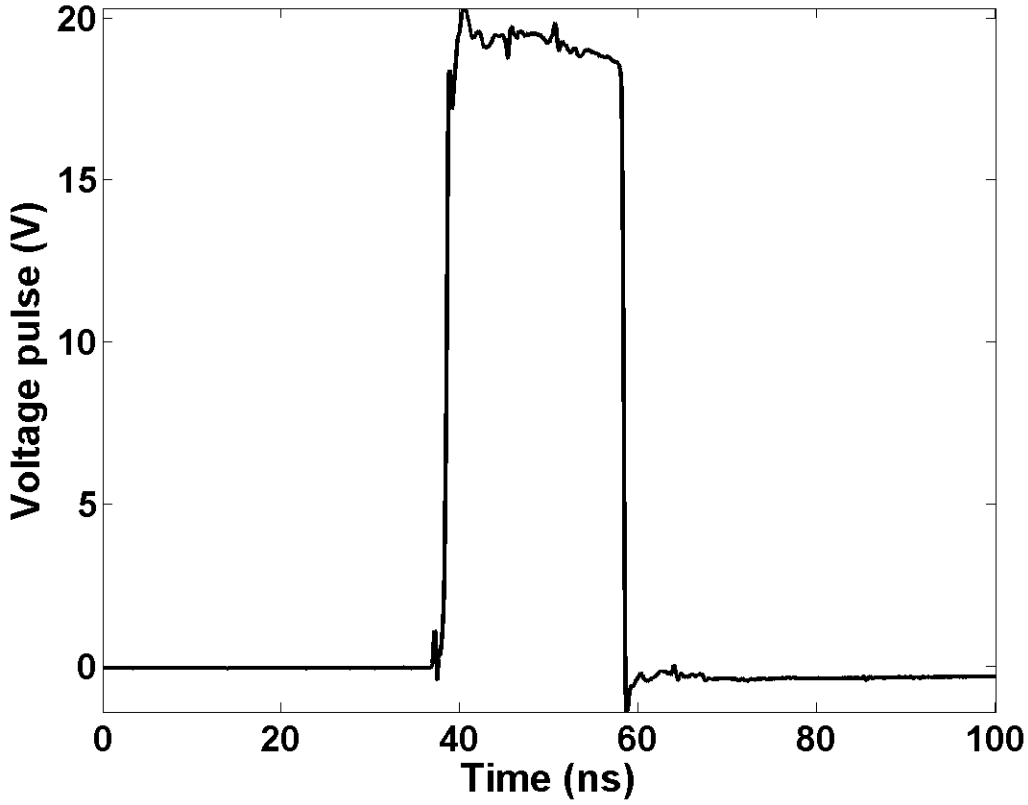

Figure 6.1. Voltage pulse used for modulating laser injection current.

6.2.2 Wavelength tracking for nanosecond laser pulse

The absorption response, $\alpha(\nu)$, measured from FC-DLS is always distorted as laser emission wavenumber, ν, is a nonlinear function of time. As described in Section 5.4.1, this distortion can be corrected by tracking the time dependence of laser frequency. The fringe density of a Michelson interferometer has been used to track this frequency chirp during the laser pulse interval. However, accurate measurement needs a very low free spectral range (FSR) for the interferometer and this FSR cannot be reduced without increasing the optical path difference between its two arms. On the other hand, large path difference increases the time delay between the pulses in two arms of the interferometer and makes it difficult for them to effectively interfere. Thus wavelength tracking method needs to be improved or optimized for laser pulse width and optical path difference in the interferometer.

6.2.3 Tapered single mode fiber as gas sensing element

Although distributed gas sensing has been demonstrated using two collimator based open-cavity gas cells as sensing elements, it is much more convenient if these mini sensor probes can be part of the single mode fiber that delivers the optical pulse. Tapered optical fibers are good candidate to realize this. The procedure for making such structure by 'heating and stretching' has been outlined by Knight et al [75]. In Figure 6.2, a tapered structure fabricated from standard telecomm fiber (SMF-28, Corning) is shown. It has maximum transmission loss of 2 dB in 1520 ~ 1570 nm wavelength range and the narrowest section of the tapered structure has a diameter of about 1 μm. Because of such narrow waist, the fiber core is no longer significant in the taper region, and the light travels in the fundamental mode along the waveguide formed by the silica waist surrounded by air. On reaching the other end of the waist, the light remaining in the waist is returned to the guided mode in the fiber core. As a result, when taper waist is small, the fundamental mode will have an evanescent tail extending significantly out into the free space surrounding the taper. This evanescent field can also be observed in the structure shown in Figure 6.2 when taper fiber has been coupled to a red laser ($\lambda = 635\,nm$) diode.

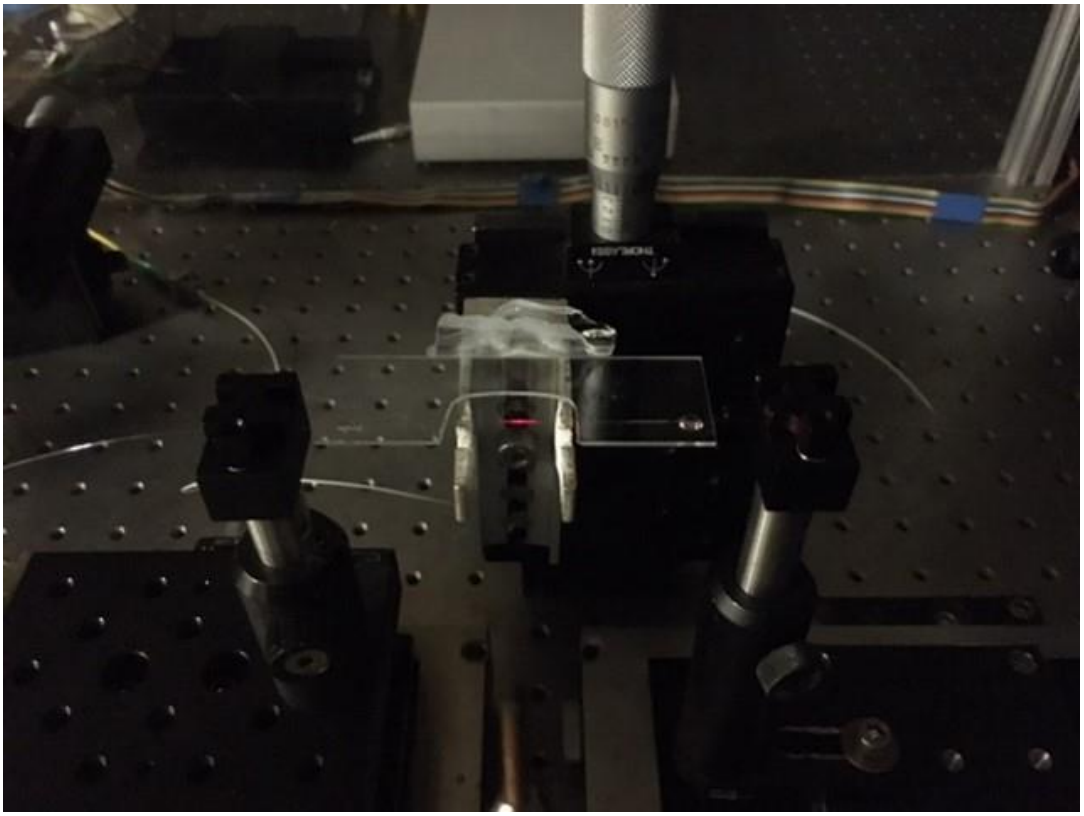

Figure 6.2. Fabricated taper fiber structure from single mode fiber (SMF-28). Notice that evanescent field is observable near the tapered region as the fiber has been coupled to a red laser diode.

The evanescent field surrounding the taper structure can be used to interact with gas molecules and hence the taper fiber can be used as a miniature gas sensing element for spatially distributed gas sensing by FC-DLS. This is experimentally validated by placing the tapered fiber structure inside a quartz vacuum chamber and exposing it to approximately 15% acetylene-air mixture. Figure 6.3 depicts this arrangement. The experimental setup described in Figure 5.15 is used for measuring acetylene absorbance. Figure 6.4 (a) plots the measured optical pulses with and without the presence of acetylene near the taper fiber. The absorbance value estimated from this experiment is shown in Figure 6.4 (b). It is clear that absorbance follows a Lorentzian profile. But, because of very small light-gas interaction length (about 1 cm), the amplitude of absorbance or sensor sensitivity is quite low. So further investigation is needed to make tapered fiber based distributed gas monitoring system practical.

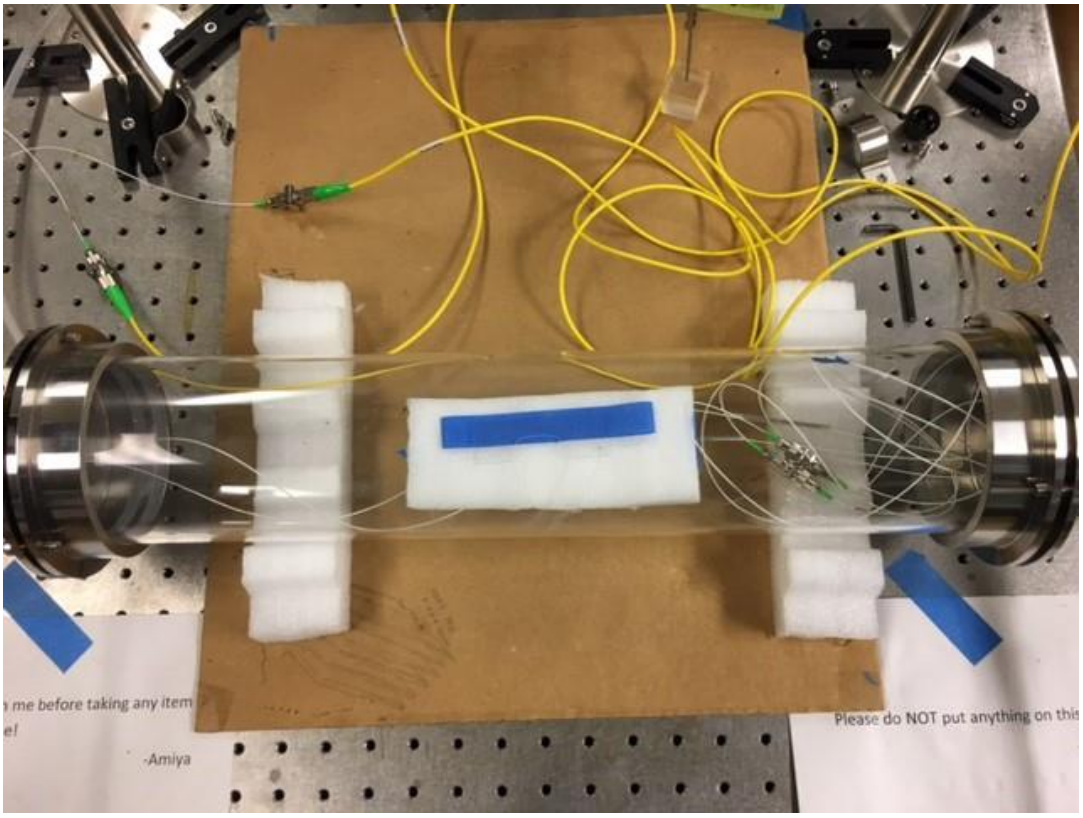

Figure 6.3. Fabricated tapered structure placed inside the quartz vacuum chamber for gas detection.

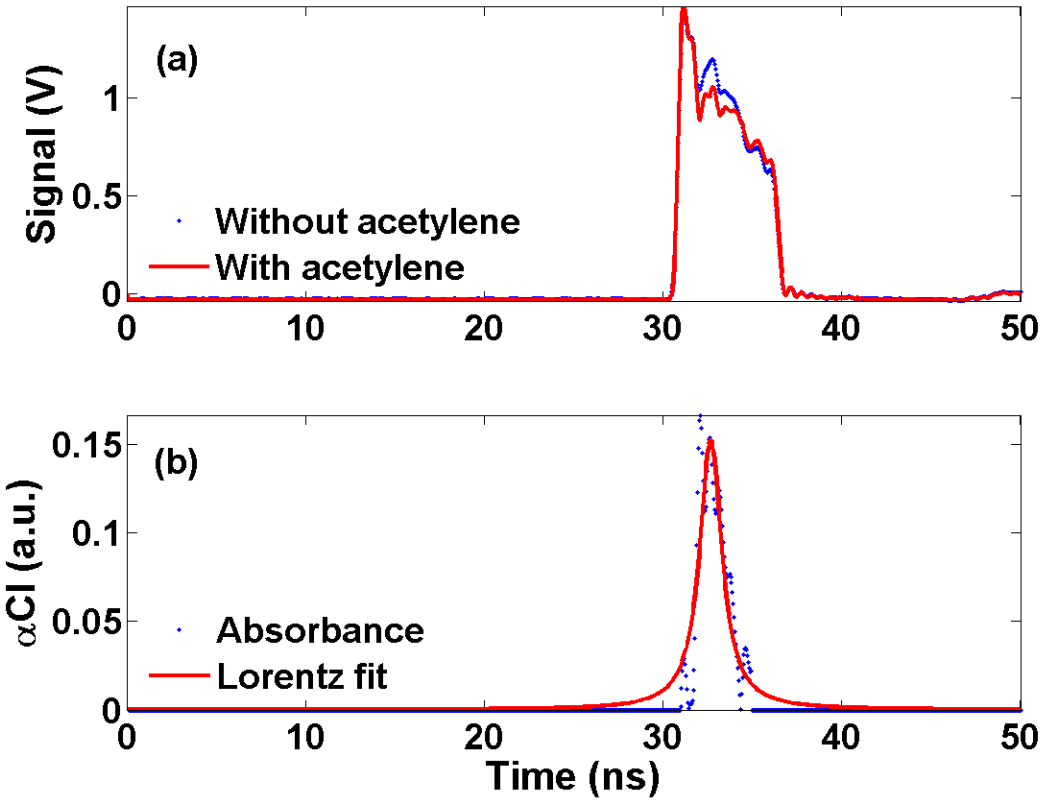

Figure 6.4. (a) Measured pulse from FC-DLS using tapered single mode fiber with and without acetylene, (b) Calculated absorption response with Lorentz fit.

Appendix A – Signal Processing for TDLS systems

For TDLS systems, *Laser* signal and *RGC* signals are used for more accurate absorption signal recovery. Since the laser intensity also changes when its emission frequency is scanned by TEC control, optical signal without any absorption is useful for absorbance calculation. This baseline signal is referred to as *Laser* signal in Figure 2.6. Because of the sinusoidal nature of optical intensity change by TEC tuning, laser output is simply described by $I(t) = I_0 + \Delta I_0 \sin(\omega t)$. The *RGC* signal is used for self-calibration of the sensor system from a known concentration mixture. It also helps improving the concentration accuracy by linear regression.

Figure A.1 shows a simplified block diagram to describe signal processing scheme for a single probe. Voltage signals at receiver board from *Laser* signal, *RGC* signal, and *Sensor* signal are denoted as V_1, V_2, and V_3 respectively. For reference, typical waveforms measured as V_1, V_2, and V_3 are depicted in Figure A.2.

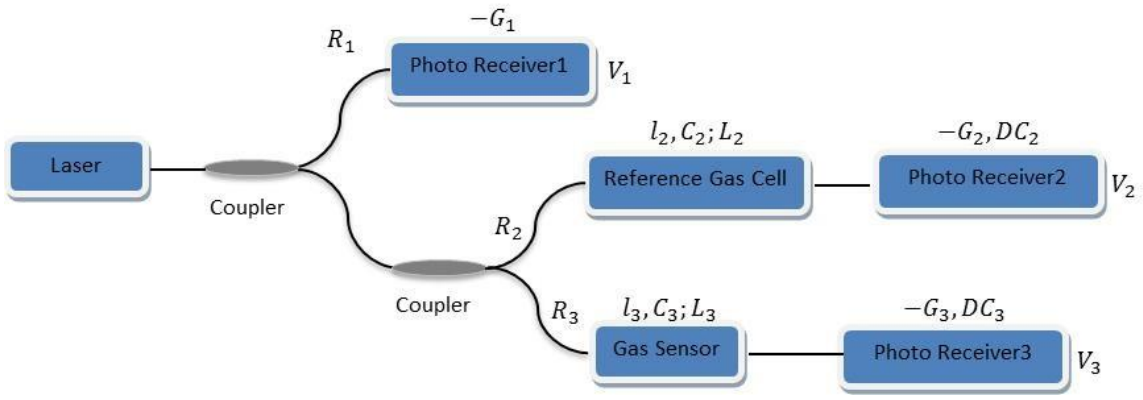

Figure A.1. Signals collected at different channels for a single sensor-probe.

In Figure A.1, R_1, R_2, R_3 are the optical coupling ratios for three channels. l_2, C_2 are optical path length and target gas concentration in reference gas cell respectively. Similarly, l_3, C_3 are optical path length and target gas concentration at sensor probe. L_2, L_3 are optical path losses in reference gas cell and sensor probe respectively. G_1, G_2, G_3 are the gains of trans-impedance amplifiers used for laser, RGC, and sensor

channel respectively. DC_2, DC_3 are the biasing offsets added to RGC and sensor channel. Laser channel has zero bias applied to it.

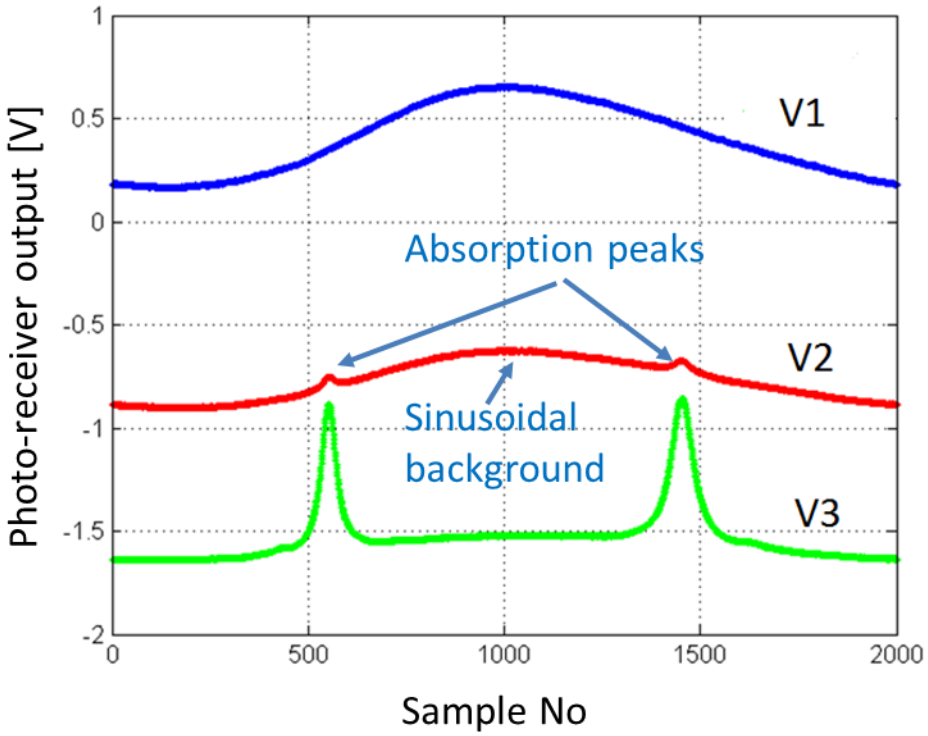

Figure A.2. Typical waveforms on three channels.

The signal processing algorithm works in the following way.

Step-1: Scaling

$$V_1 = -R_1 G_1 I_0 - R_1 G_1 \Delta I_0 \sin(\omega t)$$

Optical loss ratio, $L_{21} = \dfrac{R_2 L_2 G_2}{R_1 G_1}$

Optical loss ratio, $L_{31} = \dfrac{R_3 L_3 G_3}{R_1 G_1}$

$$V_2^{'} = \frac{V_2}{L_{21}} = \frac{R_1 G_1}{R_2 L_2 G_2} DC_2 - R_1 G_1 I_0 e^{-\alpha(t) C_2 l_2} - R_1 G_1 \Delta I_0 \sin(\omega t) e^{-\alpha(t) C_2 l_2}$$

$$V_3^{'} = \frac{V_3}{L_{31}} = \frac{R_1 G_1}{R_3 L_3 G_3} DC_3 - R_1 G_1 I_0 e^{-\alpha(t) C_3 l_3} - R_1 G_1 \Delta I_0 \sin(\omega t) e^{-\alpha(t) C_3 l_3}$$

Step-2: Shifting

$$offset_{21} = \frac{R_1 G_1}{R_2 L_2 G_2} DC_2$$

$$offset_{31} = \frac{R_1 G_1}{R_3 L_3 G_3} DC_3$$

$$V_2^{''} = V_2^{'} - offset_{21} = -R_1 G_1 I_0 e^{-\alpha(t) C_2 l_2} - R_1 G_1 \Delta I_0 \sin(\omega t) e^{-\alpha(t) C_2 l_2}$$

$$V_3^{''} = V_3^{'} - offset_{31} = -R_1 G_1 I_0 e^{-\alpha(t) C_3 l_3} - R_1 G_1 \Delta I_0 \sin(\omega t) e^{-\alpha(t) C_3 l_3}$$

Step-3: Normalization

$$peak_{RGC} = \frac{V_2^{''}}{V_1} = e^{-\alpha(t) C_2 l_2}$$

$$peak_{sensor} = \frac{V_3^{''}}{V_1} = e^{-\alpha(t) C_3 l_3}$$

Step-4: Absorbance calculation

$$\text{Absorbance, } A_{RGC} = -\log_e(peak_{RGC})$$

$$\text{Absorbance, } A_{sensor} = -\log_e(peak_{sensor})$$

After the absorbance is determined for reference gas cell and sensor probe, unknown concentration can be calculated using

$$C_3 = \frac{C_2 l_2}{l_3} \left(\frac{A_{sensor}}{A_{RGC}} \right)$$

The optical loss ratios L_{21}, L_{31} are calculated using the sinusoidal background (non-absorbing sections) that all the three waveforms V_1, V_2, V_3 have.

Appendix B – Gas Mixture Preparation

In order to get an accurate calibration curve for the gas sensor system and check its sensitivity, it was necessary to subject the sensor probe to several known concentration mixtures of methane. Nitrogen (N_2) and methane (CH_4) were mixed in different proportions to create various methane concentration mixtures in the vicinity of sensor probe. The designed sensor probe was kept in an air tight quartz chamber (see Figure B.1) to avoid any leakage. Also, polyethylene vacuum tubing was used to safely dump the methane mixture in the laboratory fume hood when the chamber was emptied. A *partial pressure based mixing* and *dilution* technique was utilized to achieve different concentration mixtures.

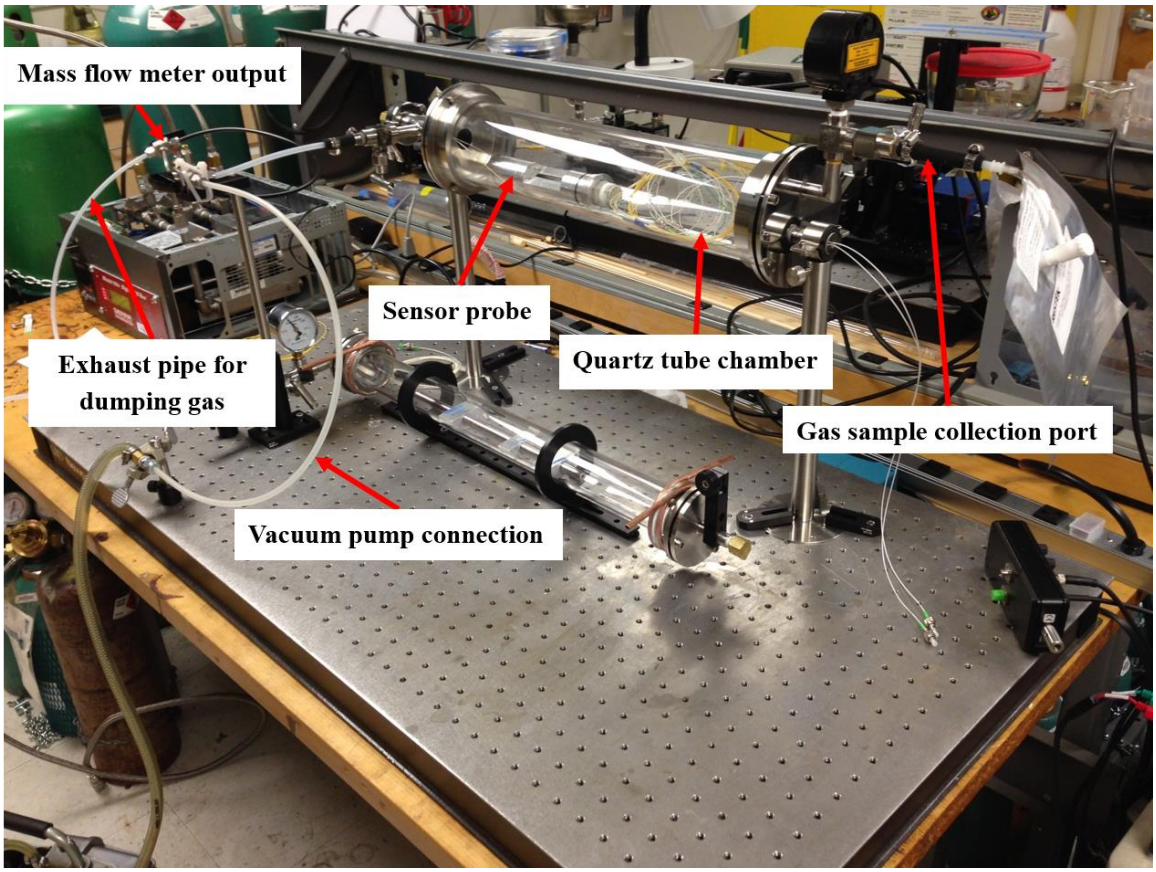

Figure B.1. Gas chamber for sensor testing and calibration (Note: Sensor probe is inside the quartz vacuum chamber).

Partial pressure of a gas in a gas mixture is defined as the hypothetical pressure of that gas if it alone occupied the volume of the mixture at the same temperature. Moreover, Dalton's law states that in a mixture of non-reacting gases, the total pressure exerted is equal to the sum of the partial pressures of the individual gases. Mathematically, the pressure of a mixture of non-reactive gases can be defined as a summation of partial pressures, $P_{total} = \sum_{i=1}^{N} P_i$, where P_i is partial pressure of i^{th} gas.

From ideal gas law, partial pressure can be expressed by $P_i = P_{total} \bullet \chi_i = \frac{P_{total} C_i}{10^6}$ where χ_i is the mole fraction and C_i is the concentration of i^{th} gas in parts per million (ppm). By using the digital vacuum gauge, it is possible to accurately measure the pressure inside the gas chamber. From these pressure readings, the partial pressure and hence the concentration for methane can be determined.

Once a fixed concentration is mixed, further lower concentrations mixtures can be prepared by careful dilution of the chamber with Nitrogen (N_2) or ambient air. It should be noted that the methane concentration in ambient air is less than 5 ppm and thus can be ignored while diluting the gas chamber mixture.

The basic setup for this scheme is shown in Figure B.2. The steps involved in this scheme are as follows.

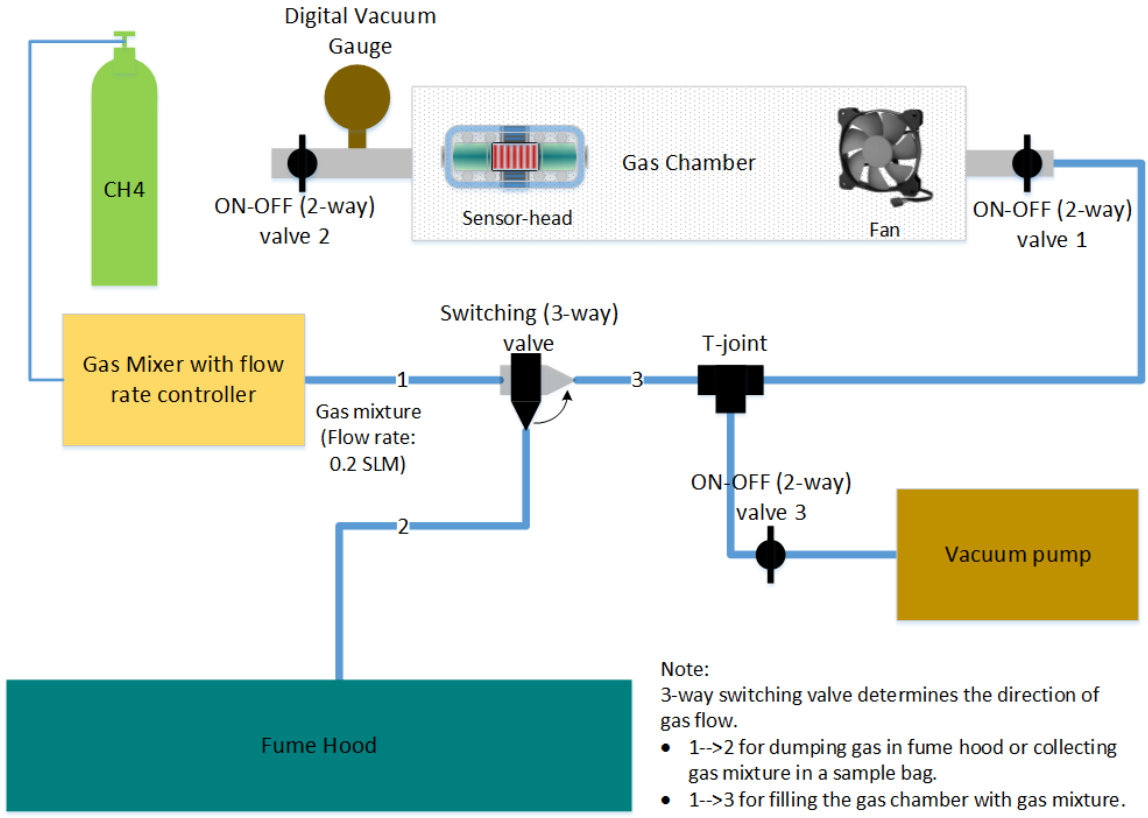

Figure B.2. Setup for sensor probe calibration (Note: Sensor probe is inside the quartz tube gas chamber).

Mixing gases by their partial pressure:

1) Keep the 3-way switching valve in 1→2 state, so that the gas mixer output is directly dumped in the fume hood.

2) Vacuum the connection tubes and the gas chamber by keeping valve-2 in OFF and valves 1 &3 in ON position.

3) After the digital vacuum gauge reads around -95 kPa, turn OFF valve-3 and shut down the vacuum pump. Note that, before vacuuming, the chamber was filled with ambient air (N2, O2, and barely any methane).

4) Flow pure methane through the gas mixer mass flow controllers into the fume hood. Allow the mixer to flow for 4 to 5 minutes so that there is not any other gas present in the gas mixer connection pipes.

5) Change the 3- way switching valve from 1→2 to 1→3 state.

6) Flow methane into the chamber till the vacuum gauge reads -90 kPa. Immediately turn OFF valve-1.

7) Open valve-2 (one to two turns) to let the ambient air get inside the chamber. Close the valve as soon as the vacuum gauge reads 0 kPa.

8) Now, partial pressure for methane is 5 kPa and 95 kPa for other gases. So the concentration of methane in the chamber is $\frac{5kPa}{(5kPa+95kPa)} = 5\%\ or\ 50,000\ ppm$.

Dilute the mixture to achieve lower concentration:

1) Turn on the vacuum pump and turn ON valve-3.

2) Open valve-1 by a small amount (Do not exceed one turn) and allow the chamber pressure drop gradually.

3) Turn OFF valve-1 as soon as the digital vacuum gauge reads -30 kPa.

4) Shut down the vacuum pump.

After vacuuming, the partial pressures inside the chamber the following: methane = 70 kPa x 5 %= 3.5 kPa, Other gases = 70 kPa x 95 % = 66.5 kPa

5) Open valve-2 (one to two turns) to let the ambient air get inside the chamber. Close the valve as soon as the vacuum gauge reads 0 kPa.

The new partial pressures are the following: methane = 3.5 kPa, Other gases = 100-3.5 kPa=96.5 kPa. So the concentration of methane in the chamber is $\frac{3.5kPa}{(3.5kPa+96.5kPa)} = 3.5\%$.

By repeating the *Dilution* step, lower concentrations can be reached. However, for this scheme to work, several precautions must be taken.

Precautions:

1) A fan must be present inside the chamber for mixing the air while running the vacuum pump for ‘Dilution’ step. Experimental evidence suggest that all the gas molecules (including methane) do not exit the chamber at the same rate.

2) Valve-1 should be not be opened by a small amount while performing ‘Dilution’ step. Here, the idea is that the fan must mix the gases very well before the vacuum pump sucks them out of the chamber. Slower vacuuming rate is better.

The digital vacuum gauge has an accuracy of ±1 kPa. Hence it is better to start with a higher partial pressure of methane. This will reduce the chances of calculated concentration being too far from actual concentration. For example, starting with a methane concentration of 500,000 ppm is more accurate than starting with 50,000 ppm. Because 500,000 ppm mixture will require a starting partial pressure of 50 kPa for methane while 50,000 ppm mixture will require a starting partial pressure of 5 kPa.

Appendix C – Wavelength Estimation from Interferometer Fringes

It is well known that wavelength chirp due to injection current pulse is a monotonically increasing function because of electron density reduction by stimulated emission process. In other words, wavenumber ν monotonically decreases in time.

The fringe pattern observed in the optical intensity at the photodetector of a Michelson interferometer can be expressed by $I(t) = I_0\left[1+\cos(2\pi\nu(t)\bullet OPD+\phi_0)\right]$, where I_0 is the average intensity, $\nu(t)=\frac{1}{\lambda(t)}$ is the wavenumber, *OPD* is the optical path difference between the two arms of the interferometer, and ϕ_0 is the initial phase.

The wavenumber change between consecutive fringes is $\Delta\nu = \nu_{n+1}-\nu_n = -\frac{1}{OPD}$ (negative sign as ν is decreasing with time). For a free spectral range of 222 MHz, OPD is approximately 46 cm. As these peak positions have been located in time domain (see Figure 5.5 (a)), $\Delta t = t_{n+1}-t_n$ is also known. Thus $\frac{d\nu}{dt}=\lim_{\Delta t\to 0}\frac{\Delta\nu}{\Delta t}$ can be evaluated as time step size Δt is very small. Once $\frac{d\nu}{dt}$ has been evaluated in MATLAB, it can be numerically integrated to calculate $\nu(t)$. The constant of integration is the mean laser emission wavenumber ν_c for the specific operating conditions (temperature and injection current) of the diode laser. ν_c can be accurately obtained if the laser wavelength chirp scans across a known gas absorption line. For example, absorption peak for carbon monoxide (CO) at 1563.09 nm can be used for the fringe pattern in Figure 5.5 (a) to calculate the wavelength chirp with time. Similarly, absorption peak for acetylene (C_2H_2) at 1532.83 nm can be used for the fringe pattern in Figure 5.7 (a).

References

1. Y. Sivathanu, *Natural Gas Leak Detection in Pipelines* (En'Urga Inc., 2003).

2. E. D. Hinkley, "High-Resolution Infrared Spectroscopy with a Tunable Diode Laser," Appl. Phys. Lett. **16**, 351–354 (1970).

3. J. Reid, J. Shewchun, B. K. Garside, and E. A. Ballik, "High sensitivity pollution detection employing tunable diode lasers," Appl. Opt. **17**, 300 (1978).

4. J. Reid, B. K. Garside, J. Shewchun, M. El-Sherbiny, and E. A. Ballik, "High sensitivity point monitoring of atmospheric gases employing tunable diode lasers," Appl. Opt. **17**, 1806 (1978).

5. D. T. Cassidy and J. Reid, "Atmospheric pressure monitoring of trace gases using tunable diode lasers.," Appl. Opt. **21**, 1185–1190 (1982).

6. D. S. Bomse, a C. Stanton, and J. a Silver, "Frequency-Modulation and Wavelength Modulation Spectroscopies - Comparison of Experimental Methods Using a Lead-Salt Diode-Laser," Appl. Opt. **31**, 718–731 (1992).

7. B. Culshaw, G. Stewart, F. Dong, C. Tandy, and D. Moodie, "Fibre optic techniques for remote spectroscopic methane detection—from concept to system realisation," Sens. Actuators B Chem. **51**, 25–37 (1998).

8. P. Werle, "A review of recent advances in semiconductor laser based gas monitors," Spectrochim. Acta. A. Mol. Biomol. Spectrosc. **54**, 197–236 (1998).

9. D. Richter, D. G. Lancaster, and F. K. Tittel, "Development of an automated diode-laser-based multicomponent gas sensor," Appl. Opt. **39**, 4444 (2000).

10. H. Teichert, T. Fernholz, and V. Ebert, "Simultaneous in situ measurement of CO, H2O, and gas temperatures in a full-sized coal-fired power plant by near-infrared diode lasers.," Appl. Opt. **42**, 2043–2051 (2003).

11. X. Zhou, X. Liu, J. B. Jeffries, and R. K. Hanson, "Development of a sensor for temperature and water concentration in combustion gases using a single tunable diode laser," Meas. Sci. Technol. **14**, 1459 (2003).

12. D. T. Cassidy and L. J. Bonnell, "Trace gas detection with short-external-cavity InGaAsP diode laser transmitter modules operating at 158 μm," Appl. Opt. **27**, 2688 (1988).

13. X. Zhu and D. T. Cassidy, "Modulation spectroscopy with a semiconductor diode laser by injection-current modulation," J. Opt. Soc. Am. B **14**, 1945 (1997).

14. J. Reid and D. Labrie, "Second-Harmonic Detection with Tunable Diode Lasers - Comparison of Experiment and Theory," Appl. Phys. B **26**, 203–210 (1981).

15. J. M. Supplee, E. a Whittaker, and W. Lenth, "Theoretical description of frequency modulation and wavelength modulation spectroscopy.," Appl. Opt. **33**, 6294–6302 (1994).

16. L. C. Philippe and R. K. Hanson, "Laser diode wavelength-modulation spectroscopy for simultaneous measurement of temperature, pressure, and velocity in shock-heated oxygen flows.," Appl. Opt. **32**, 6090–6103 (1993).

17. I. Linnerud, P. Kaspersen, T. Jæ ger, and T. Jaeger, "Gas monitoring in the process industry using diode laser spectroscopy," Appl. Phys. B Lasers Opt. **67**, 297–305 (1998).

18. S. Schilt, L. Thevenaz, and P. Robert, "Wavelength Modulation Spectroscopy: Combined Frequency and Intensity Laser Modulation," Appl. Opt. **42**, 6728–6738 (2003).

19. R. Sur, K. Sun, J. B. Jeffries, R. K. Hanson, R. J. Pummill, T. Waind, D. R. Wagner, and K. J. Whitty, "TDLAS-based sensors for in situ measurement of syngas composition in a pressurized, oxygen-blown, entrained flow coal gasifier," Appl. Phys. B Lasers Opt. **116**, 33–42 (2014).

20. K. Sun, R. Sur, J. B. Jeffries, R. K. Hanson, T. Clark, J. Anthony, S. Machovec, and J. Northington, "Application of wavelength-scanned wavelength-modulation spectroscopy H2O absorption measurements in an engineering-scale high-pressure coal gasifier," Appl. Phys. B **117**, 411–421 (2014).

21. J. T. C. Liu, G. B. Rieker, J. B. Jeffries, M. R. Gruber, C. D. Carter, T. Mathur, and R. K. Hanson, "Near-infrared diode laser absorption diagnostic for temperature and water vapor in a scramjet combustor," Appl. Opt. **44**, 6701 (2005).

22. G. B. Rieker, H. Li, X. Liu, J. T. C. Liu, J. B. Jeffries, R. K. Hanson, M. G. Allen, S. D. Wehe, P. A. Mulhall, H. S. Kindle, A. Kakuho, K. R. Sholes, T. Matsuura, and S. Takatani, "Rapid measurements of temperature and H2O concentration in IC engines with a spark plug-mounted diode laser sensor," Proc. Combust. Inst. **31**, 3041–3049 (2007).

23. J. Henningsen and H. Simonsen, "Quantitative wavelength-modulation spectroscopy without certified gas mixtures," Appl. Phys. B **70**, 627–633 (2000).

24. K. Duffin, A. J. McGettrick, W. Johnstone, G. Stewart, and D. G. Moodie, "Tunable diode-laser spectroscopy with wavelength modulation: A calibration-free approach to the recovery of absolute gas absorption line shapes," J. Light. Technol. **25**, 3114–3125 (2007).

25. A. J. McGettrick, K. Duffin, W. Johnstone, G. Stewart, and D. G. Moodie, "Tunable diode laser spectroscopy with wavelength modulation: A phasor decomposition method for calibration-free measurements of gas concentration and pressure," J. Light. Technol. **26**, 432–440 (2008).

26. W. Johnstone, A. J. McGettrick, K. Duffin, A. Cheung, and G. Stewart, "Tunable diode laser spectroscopy for industrial process applications: system characterization in conventional and new approaches," IEEE Sens. J. **8**, 1079–1088 (2008).

27. A. L. Chakraborty, K. C. Ruxton, W. Johnstone, M. Lengden, and K. Duffin, "Elimination of residual amplitude modulation in tunable diode laser wavelength

modulation spectroscopy using an optical fiber delay line," Opt. Express **17**, 9602–9607 (2009).

28. G. Stewart, W. Johnstone, J. R. P. Bain, K. Ruxton, and K. Duffin, "Recovery of Absolute Gas Absorption Line Shapes Using Tunable Diode Laser Spectroscopy With Wavelength Modulation-Part I: Theoretical Analysis," J. Light. Technol. **29**, 811–821 (2011).

29. H. Li, G. B. Rieker, X. Liu, J. B. Jeffries, and R. K. Hanson, "Extension of wavelength-modulation spectroscopy to large modulation depth for diode laser absorption measurements in high-pressure gases.," Appl. Opt. **45**, 1052–1061 (2006).

30. G. B. Rieker, H. Li, X. Liu, J. B. Jeffries, R. K. Hanson, M. G. Allen, S. D. Wehe, P. a Mulhall, and H. S. Kindle, "A diode laser sensor for rapid, sensitive measurements of gas temperature and water vapour concentration at high temperatures and pressures," Meas. Sci. Technol. **18**, 1195–1204 (2007).

31. G. B. Rieker, J. B. Jeffries, and R. K. Hanson, "Calibration-free wavelength-modulation spectroscopy for measurements of gas temperature and concentration in harsh environments.," Appl. Opt. **48**, 5546–5560 (2009).

32. L. S. Rothman, I. E. Gordon, a. Barbe, D. C. Benner, P. F. Bernath, M. Birk, V. Boudon, L. R. Brown, a. Campargue, J. P. Champion, K. Chance, L. H. Coudert, V. Dana, V. M. Devi, S. Fally, J. M. Flaud, R. R. Gamache, a. Goldman, D. Jacquemart, I. Kleiner, N. Lacome, W. J. Lafferty, J. Y. Mandin, S. T. Massie, S. N. Mikhailenko, C. E. Miller, N. Moazzen-Ahmadi, O. V. Naumenko, a. V. Nikitin, J. Orphal, V. I. Perevalov, a. Perrin, a. Predoi-Cross, C. P. Rinsland, M. Rotger, M. Šimečková, M. a H. Smith, K. Sung, S. a. Tashkun, J. Tennyson, R. a. Toth, a. C. Vandaele, and J. Vander Auwera, "The HITRAN 2008 molecular spectroscopic database," J. Quant. Spectrosc. Radiat. Transf. **110**, 533–572 (2009).

33. K. Sun, X. Chao, R. Sur, C. S. Goldenstein, J. B. Jeffries, and R. K. Hanson, "Analysis of calibration-free wavelength-scanned wavelength modulation spectroscopy

for practical gas sensing using tunable diode lasers," Meas. Sci. Technol. **24**, 125203 (2013).

34. C. S. Goldenstein, C. L. Strand, I. a Schultz, K. Sun, J. B. Jeffries, and R. K. Hanson, "Fitting of calibration-free scanned-wavelength-modulation spectroscopy spectra for determination of gas properties and absorption lineshapes.," Appl. Opt. **53**, 356–67 (2014).

35. M. Zavrsnik and G. Stewart, "Coherence addressing of quasi-distributed absorption sensors by the FMCW method," J. Light. Technol. **18**, 57–65 (2000).

36. M. Zavrsnik and G. Stewart, "Analysis of quasi-distributed optical sensors combining rf modulation with the FMCW method," Opt. Eng. **39**, 3053–3059 (2000).

37. M. Zavrsnik and G. Stewart, "Theoretical analysis of a quasi-distributed optical sensor system using FMCW for application to trace gas measurement," Sens. Actuators B Chem. **71**, 31–35 (2000).

38. Z. G. Guan, B. Zhou, G. Liu, and S. He, "Quasi-Distributed Absorption Sensing System Based on a Coherent Multiplexing Technique," IEEE Photonics Technol. Lett. **19**, 792–794 (2007).

39. M. Lu, K. Nonaka, H. Kobayashi, J. Yang, and L. Yuan, "Quasi-distributed region selectable gas sensing for long distance pipeline maintenance," Meas. Sci. Technol. **24**, 095104 (2013).

40. Juntao Wu, *Distributed Fiber Optic Gas Sensing for Harsh Environment* (U.S. Department of Energy, 2008).

41. D. Wang, Y. Wang, J. Gong, and A. Wang, "Fully-Distributed Fiber-Optic Hydrogen Sensing Using Acoustically-Induced Long-Period Grating," Photonics Technol. Lett. IEEE **23**, 1–1 (2011).

42. K. N. Liou, *An Introduction to Atmospheric Radiation* (Academic Press, 2002).

43. G. E. Thomas and K. Stamnes, *Radiative Transfer in the Atmosphere and Ocean* (Cambridge University Press, 2002).

44. P. L. Varghese and R. K. Hanson, "Collisional Narrowing Effects on Spectral-Line Shapes Measured At High-Resolution," Appl. Opt. **23**, 2376–2385 (1984).

45. A. B. McLean, C. E. J. Mitchell, and D. M. Swanston, "Implementation of an efficient analytical approximation to the Voigt function for photoemission lineshape analysis," J. Electron Spectrosc. Relat. Phenom. **69**, 125–132 (1994).

46. G. Rieker, J. Jeffries, and R. K. Hanson, "Measurements of high-pressure CO2 absorption near 2.0 μm and implications on tunable diode laser sensor design," Appl. Phys. B Lasers Opt. **94**, 51–63 (2009).

47. L. Li, N. Arsad, G. Stewart, G. Thursby, D. Uttamchandani, B. Culshaw, and W. Yi-ding, "Absorption Line Profile Recovery Based on TDLS and MEMS Micro-Mirror for Photoacoustic Gas Sensing," Spectrosc. Spectr. Anal. **31**, 1814–1818 (2011).

48. C. S. Goldenstein, J. B. Jeffries, and R. K. Hanson, "Diode laser measurements of linestrength and temperature-dependent lineshape parameters of H2O-, CO2-, and N2-perturbed H2O transitions near 2474 and 2482nm," J. Quant. Spectrosc. Radiat. Transf. **130**, 100–111 (2013).

49. R. M. Spearrin, C. S. Goldenstein, J. B. Jeffries, and R. K. Hanson, "Quantum cascade laser absorption sensor for carbon monoxide in high-pressure gases using wavelength modulation spectroscopy.," Appl. Opt. **53**, 1938–46 (2014).

50. C. S. Goldenstein and R. K. Hanson, "Diode-laser measurements of linestrength and temperature-dependent lineshape parameters for H2O transitions near 1.4 μm using Voigt, Rautian, Galatry, and speed-dependent Voigt profiles," J. Quant. Spectrosc. Radiat. Transf. **152**, 127–139 (2015).

51. A. Upadhyay and A. L. Chakraborty, "Residual Amplitude Modulation Method Implemented at the Phase Quadrature Frequency of a 1650-nm Laser Diode for Line Shape Recovery of Methane," IEEE Sens. J. **15**, 1153–1160 (2015).

52. A. R. Behera, B. Dong, and A. Wang, "Fiber Optic Gas Monitoring System for Coal Mine Safety," in (OSA, 2015), p. FTh1E.2.

53. S. Sumida, S. Okazaki, S. Asakura, H. Nakagawa, H. Murayama, and T. Hasegawa, "Distributed hydrogen determination with fiber-optic sensor," Sens. Actuators B Chem. **108**, 508–514 (2005).

54. C. S. Goldenstein, I. a Schultz, J. B. Jeffries, and R. K. Hanson, "Two-color absorption spectroscopy strategy for measuring the column density and path average temperature of the absorbing species in nonuniform gases," Appl. Opt. **52**, 7950–7962 (2013).

55. L. S. Rothman, D. Jacquemart, A. Barbe, D. C. Benner, M. Birk, L. R. Brown, M. R. Carleer, J. C. Chackerian, and K. C. Et Al., "The HITRAN 2008 molecular spectroscopic database," J Quant Spectrosc Radiat Transf. **110**, 533–572 (2008).

56. S. Kobayashi, Y. Yamamoto, M. Ito, and T. Kimura, "Direct frequency modulation in AlGaAs semiconductor lasers," IEEE J. Quantum Electron. **18**, 582–595 (1982).

57. B. Dong, A. Behera, B. Liu, S. Zhang, A. Wang, and J. Gong, "Fiber optic gas monitoring system," U.S. patent WO2015038217 A1 (March 19, 2015).

58. P. Rako, "Photodiode Amplifiers–Changing light to electricity," Natl. Semicond. (2004).

59. T. Wang and B. Erhman, "Compensate transimpedance amplifiers intuitively," Tex. Instrum. Appl. Rep. (1993).

60. P. C. D. Hobbs, "Ultrasensitive laser measurements without tears," Appl. Opt. **36**, 903–920 (1997).

61. P. C. D. Hobbs, "Photodiode Front Ends: The Real Story," Opt. Photonics News **12**, 44–47 (2001).

62. M. Pachchigar, "Design considerations for a transimpedance amplifier," (2008).

63. R. Arndt, "Analytical line shapes for Lorentzian signals broadened by modulation," J. Appl. Phys. **36**, 2522–2524 (1965).

64. C. E. Wieman and L. Hollberg, "Using diode lasers for atomic physics," Rev. Sci. Instrum. **62**, 1–20 (1991).

65. C. Lin, T. P. Lee, and C. A. Burrus, "Picosecond frequency chirping and dynamic line broadening in InGaAsP injection lasers under fast excitation," Appl. Phys. Lett. **42**, 141–143 (1983).

66. T. L. Koch and J. E. Bowers, "Nature of wavelength chirping in directly modulated semiconductor lasers," Electron. Lett. **20**, 1038–1040 (1984).

67. N. A. Olsson, N. K. Dutta, and K.-Y. Liou, "Dynamic linewidth of amplitude-modulated single-longitudinal-mode semiconductor lasers operating at 1.5 μm wavelength," Electron. Lett. **20**, 121 (1984).

68. A. Sudbo, "The frequency chirp of current modulated semiconductor diode lasers," IEEE J. Quantum Electron. **22**, 1006–1008 (1986).

69. M. Osinski and J. Buus, "Linewidth broadening factor in semiconductor lasers–An overview," IEEE J. Quantum Electron. **23**, 9–29 (1987).

70. Y.-Q. Li and M. Xiao, "Transient spectroscopy with a current-switched semiconductor diode laser," J. Opt. B Quantum Semiclassical Opt. **1**, 541 (1999).

71. M. Ito and T. Kimura, "Carrier density dependence of refractive index in AlGaAs semiconductor lasers," IEEE J. Quantum Electron. **16**, 910–911 (1980).

72. K. Stubkjaer, M. Asada, S. Arai, and Y. Suematsu, "Spontaneous Recombination, Gain and Refractive Index Variation for 1.6 μm Wavelength InGaAsP/InP Lasers," Jpn. J. Appl. Phys. **20**, 1499 (1981).

73. K. Kishino, S. Aoki, and Y. Suematsu, "Wavelength variation of 1.6 um wavelength buried heterostructure GaInAsP/InP lasers due to direct modulation," IEEE J. Quantum Electron. **18**, 343–351 (1982).

74. A. Behera and A. Wang, "Calibration-free wavelength modulation spectroscopy: symmetry approach and residual amplitude modulation normalization," Appl. Opt. **55**, 4446 (2016).

75. J. C. Knight, G. Cheung, F. Jacques, and T. A. Birks, "Phase-matched excitation of whispering-gallery-mode resonances by a fiber taper," Opt. Lett. **22**, 1129–1131 (1997).